

Washington University in St. Louis
Washington University Open Scholarship

Engineering and Applied Science Theses &
Dissertations

McKelvey School of Engineering


Spring 5-15-2016

Cyclotron Production and Biomedical Imaging Applications of the PET Isotope Manganese-52

Andrew Lake Wooten

Washington University in St. Louis

Follow this and additional works at: https://openscholarship.wustl.edu/eng_etds

 Part of the [Nuclear Engineering Commons](#), [Other Chemistry Commons](#), and the [Radiochemistry Commons](#)

Recommended Citation

Wooten, Andrew Lake, "Cyclotron Production and Biomedical Imaging Applications of the PET Isotope Manganese-52" (2016).
Engineering and Applied Science Theses & Dissertations. 174.
https://openscholarship.wustl.edu/eng_etds/174

This Dissertation is brought to you for free and open access by the McKelvey School of Engineering at Washington University Open Scholarship. It has been accepted for inclusion in Engineering and Applied Science Theses & Dissertations by an authorized administrator of Washington University Open Scholarship. For more information, please contact digital@wumail.wustl.edu.

WASHINGTON UNIVERSITY IN ST. LOUIS

School of Engineering & Applied Sciences
Department of Biomedical Engineering

Dissertation Examination Committee:

Suzanne E. Lapi, Chair
Mark A. Anastasio, Co-Chair
Parag Banerjee
Joseph P. Culver
Jason S. Lewis
Samuel A. Wickline

Cyclotron Production and Biomedical Imaging Applications of the PET Isotope Manganese-52
by
Andrew Lake Wooten

A dissertation presented to the
Graduate School of Arts & Sciences
of Washington University in
partial fulfillment of the
requirements for the degree
of Doctor of Philosophy

May 2016
Saint Louis, Missouri

© 2016, Andrew Lake Wooten

Table of Contents

List of Figures.....	iv
List of Tables.....	vii
Research Acknowledgments.....	viii
Funding Acknowledgments.....	x
Personal Acknowledgments.....	xi
Disclaimers.....	xiii
Abstract of the Dissertation.....	xv
Chapter 1. Introduction.....	1
1.1. The Paradigm of Molecular Imaging.....	1
1.2. Motivations for Studying Manganese.....	3
1.3. Radioactive Decay, Detection, and In Vivo Imaging.....	8
1.4. Selection of ^{52}Mn as a Radiotracer.....	20
1.5. Thesis and Scope of this Dissertation.....	27
1.6. References.....	27
Chapter 2. Nuclear Cross-Sections and Chemical Separation of $^{52}\text{Mn}^{3+}$	35
2.1. Background.....	35
2.2. Experimental.....	37
2.3. Results.....	56
2.4. Discussion.....	62
2.5. Conclusions and Recommendations.....	63
2.6. References.....	64
Chapter 3. Biodistribution and PET Imaging of $^{52}\text{Mn}^{3+}$	68
3.1. Background.....	68
3.2. Experimental.....	70
3.3. Results.....	74
3.4. Discussion.....	79
3.5. Conclusions and Recommendations.....	86
3.6. References.....	87
Chapter 4. Applications for ^{52}Mn in PET/MR Imaging.....	91
4.1. Background.....	91
4.2. Experimental.....	92

Table of Contents (continued)

4.3. Results	94
4.4. Discussion.....	97
4.5. Conclusions and Recommendations.....	98
4.6. References	98
Chapter 5. Remotely-Controlled Modules for the Isolation of PET Radiometals”	100
5.1. Background.....	101
5.2. Experimental.....	111
5.3. Results	130
5.4. Discussion.....	134
5.5. Conclusions and Recommendations.....	139
5.6. References	140
Chapter 6. Compiled Conclusions and Recommendations	144
Appendix A. Calibration Setting Numbers for Selected PET Radioisotopes in Ionization Dose Calibrators	

List of Figures

Figure 1.1. Illustration of the mechanism behind ionization chambers.	11
Figure 1.2. Illustration of the mechanism underlying scintillation radiation detectors.....	12
Figure 1.3. Illustration of the mechanism underlying semiconductor radiation detectors.....	12
Figure 1.4. Illustration of the physics of positron emission tomography.....	17
Figure 1.5. Photograph of a General Electric (GE) Optima PET/CT 560 human scanner.....	18
Figure 1.6. Lesion from multiple myeloma viewed with FDG-PET, CT, and MR.....	19
Figure 1.7. Simplified level decay scheme for $^{52,52m}\text{Mn}$	25
Figure 2.1. Photographs illustrating the process for the fabrication of thin Cr foil discs.	39
Figure 2.2. Photograph of one style of target holder used in this dissertation.	40
Figure 2.3. Plot showing the activity ratios calculated using $t_b=120$ sec and recommended cross-section data from the IAEA for the $^{nat}\text{Cu}(p,x)^{63,65}\text{Zn}$ monitor reactions.	48
Figure 2.4: Cumulative cross-section results for the $^{nat}\text{Cr}(p,x)^{52}\text{Mn}$ reaction.	57
Figure 2.5. Cross-section results for the $^{nat}\text{Cr}(p,x)^{52m}\text{Mn}$ reaction.	59
Figure 2.6. Cross-section results for the $^{nat}\text{Cr}(p,x)^{54}\text{Mn}$ reaction.	60
Figure 2.7. Elution profiles showing the elution of Cr(III) in 0.1 M H_2SO_4 and $^{52}\text{Mn(II)}$ in various eluents.	62
Figure 3.1. Plastic chamber for inhalation studies in mice.....	73
Figure 3.2. Plot showing results from ex vivo biodistribution of saline solutions containing ^{52}Mn administered via intravenous injection or inhalation.	75
Figure 3.3. PET/CT images of mice at 1 h and 3 days following intravenous administration of ^{52}Mn in aqueous solution, windowed for visualizing activity in the abdomen.....	76

List of Figures (continued)

Figure 3.4. Results from ex vivo biodistribution performed shortly after imaging at 3 day timepoint.	76
Figure 3.5. Biodistribution results of ^{52}Mn isolated by anion-exchange chromatography and administered in a saline solution by intravenous injection into male CD-1 rats.	77
Figure 3.6. Excretion profile for male rats from the 7-day cohort that received intravenous administration of ^{52}Mn	77
Figure 3.7. Approximately ventral view of a maximum intensity projection (MIP) image of PET signal co-registered with CT image of a male CD-1 rat at 7 days following intravenous administration of ^{52}Mn in saline.	78
Figure 3.8. Post-imaging biodistribution results of ^{52}Mn in male CD-1 rats.	79
Figure 3.9. T_1 -weighted MRI images of a normoglycemic (non-diabetic) human and a human with type 2 diabetes.	85
Figure 4.1. Phantom design and images from inversion-recovery MRI experiment with different concentrations of Mn(II) in water imaged at many different inversion times (TI).	94
Figure 4.2. Results from inversion recovery experiment for several concentrations of Mn(II) solutions in water.	95
Figure 4.3. Plot of longitudinal relaxation rate (R_1) versus concentration of Mn(II) based on inversion recovery experiment.	95
Figure 4.4. PET/MR images of phantom consisting of conical tubes containing aqueous solutions of different amounts of non-radioactive $\text{MnCl}_2 \cdot 4(\text{H}_2\text{O})$ and radioactive $^{52}\text{Mn(II)}$	96
Figure 5.1. Examples of commercially available hot cell capable of housing and integrating with automated modules.	102
Figure 5.2. Simplified decay scheme for ^{89}Zr	104
Figure 5.3. Screen shot of published cross-section data for reactions relevant to bombardment of ^{nat}Y with low-energy protons.	106
Figure 5.4. Cross-sections for the production of $^{86,86m}\text{Y}$ via bombardment of ^{86}Sr with low-energy protons.	110
Figure 5.5. Photograph of the disassembled (left) and assembled (right) Y foil target and Niobium target holder.	113

List of Figures (continued)

Figure 5.6. A flowchart describing the process for production and isolation of ^{89}Zr from an irradiated Y foil.....	115
Figure 5.7. A flowchart that describes the process for the production and chemical separation of ^{86}Y from an irradiated SrO target.	117
Figure 5.8. Process flow diagram for the automated module used for chemical separation of ^{89}Zr from irradiated $^{\text{nat}}\text{Y}$ foils.....	119
Figure 5.9. Photograph of the module for isolating ^{89}Zr from $^{\text{nat}}\text{Y}$ metal target material.	120
Figure 5.10. Screenshot of the window containing the graphical user interface (GUI) that was used to control the automated module.....	122
Figure 5.11. Process flow diagram for the automated module used for chemical separation of ^{86}Y from irradiated SrO powder targets.....	124
Figure 5.12. A photograph of the automated module for ^{86}Y	125
Figure 5.13. Screenshot of the window containing the graphical user interface (GUI) that controlled the automated module.....	126
Figure 5.14. Process flow diagram for a module for the isolation of ^{52}Mn from Cr metal.	129
Figure 5.15. Distribution of ^{89}Zr in various components after each production.	131
Figure 5.16. Gamma spectra of diluted aliquots from the product vial from two different productions. DFO- ^{89}Zr titration curve that resulted in an effective specific activity of $63 \text{ mCi}\cdot\mu\text{mol}^{-1}$ for a selected ^{89}Zr production.....	132
Figure 5.17. Distribution of ^{86}Y in various components after each production.	133

List of Tables

Table 1.1. Summary of radiation emitted directly or indirectly by radioactive decay.....	9
Table 1.2. Summary of non-imaging technologies for detecting radioactivity.....	14
Table 1.3. Selection considerations for radionuclides in biomedical experiments.	21
Table 1.4. Comparison of decay properties of radioisotopes of manganese.....	24
Table 1.5. Data for radioactive decay of ^{52}Mn	25
Table 1.6. Comparison of decay characteristics of ^{52}Mn to other PET radionuclides.....	26
Table 1.7. Comparison of ^{52}Mn to other PET radionuclides.....	26
Table 2.1. Summary of the radioisotope products in irradiated Cu and Cr foils.....	43
Table 2.2 Cross-section results for the $^{\text{nat}}\text{Cr}(p,x)^{52}\text{Mn}$ reaction.	57
Table 2.3. Cross-section results for the $^{\text{nat}}\text{Cr}(p,x)^{52\text{m}}\text{Mn}$ reaction.	59
Table 2.4. Cross-section results for the $^{\text{nat}}\text{Cr}(p,x)^{54}\text{Mn}$ reaction.	61
Table 2.5. Predicted yields for $^{\text{nat}}\text{Cr}(p,x)$ reactions at saturation.....	61
Table 5.1. Published automated modules for production of $^{60,64}\text{Cu}$, ^{86}Y , and ^{89}Zr	103
Table 5.2. Summary of characteristics for production of ^{89}Zr using a low-energy cyclotron.....	106
Table 5.3. Summary of chemical and nuclear decay properties of ^{86}Y with a simplified decay scheme.....	109

Research Acknowledgments

My sincere gratitude goes to my primary Ph.D. advisor, Suzanne Lapi, Ph.D. I appreciate how quickly after joining her research group she trusted me with important responsibilities and believed in my abilities to handle new scientific concepts, tasks, and situations. Prof. Lapi took care of many details behind the scenes and was generous to me with her time, funding my stipend and research expenses, and sending me to scientific meetings, fantastic summer schools in nuclear science, and even a month of research at Brookhaven National Laboratory. I also thank Mark Anastasio, Ph.D., who was my advisor of record for my Ph.D. program, and Jason Lewis, Ph.D., who provided expert advice and travelled to St. Louis for meetings, as well as the other members of my thesis committee for their time over the past few years: Parag Banerjee, Ph.D., Joseph Culver, Ph.D., and Samuel Wickline, M.D.

My work in the Lapi group was performed with the advice and assistance of many very helpful group members, individuals inside and outside of WUSTL, and several core facilities and external companies. Specific contributions to the work are mentioned throughout this dissertation, but several people deserve special mention. First among these is Ben Lewis, a former undergraduate at WUSTL, who made significant contributions to several projects presented in this dissertation. Also, Luke Lawrence contributed immensely to the work in automated modules for remotely controlled isolations of ^{89}Zr and ^{86}Y (Chapter 5). I also received assistance and/or advice from many other current and former members of the Lapi research group (esp. Kathryn Andel, Tolu Aweda, Ph.D., Rebecca Gross, Tara Mastren, Ph.D., Vernal Richards, Ph.D., Alex Zheleznyak). I worked closely with the Isotope Production Team (esp.

Evelyn Madrid) and the Cyclotron Facility (esp. Greg Gaehle, Luke Lawrence, Bill Margenau, Pat Margenau).

I benefitted from numerous core facilities and departments at WUSTL, including the WUSM Instrument Machine Shop (esp. Dave Trame), the WUSM/MIR Preclinical PET/CT Imaging Facility (esp. Nikki Fettig, Amanda Roth), the WUSM/MIR Center for Clinical Imaging Research (esp. Glenn Foster), and the WUSTL machine shop in the Department of Chemistry (esp. Jim Linders). Outside of WUSTL, I am indebted to Four Star Finishing in Saint Louis (esp. Gene Sprung) for advice and for electroplating of chromium. Finally, I am grateful to the current and former principal investigators and leaders who established MIR as such a wonderful place to study isotope production and PET imaging (esp. in recent years Gil Jost, M.D., Michael Welch, Ph.D.).

Funding Acknowledgments

The research in this dissertation would not have been possible without funding from numerous sources for personnel, materials, procedures, etc. Project-specific sources of funding are identified on the first page of chapters in this dissertation. I am also grateful for sources of funding for my training that were not project-specific, which included: the Nuclear Science and Security Consortium (NSSC), a program funded by the United States Department of Energy (U.S. DOE)/National Nuclear Security Administration (NNSA) (DE-NA0000979; See disclaimer in frontmatter of this dissertation.) and a fellowship from the Imaging Sciences Pathway at WUSM/DBBS, funded by NIH/NIBIB (T32EB014855-01). Project specific funding is also greatly appreciated from the Nuclear Physics Isotope Program within the U.S. DOE Office of Science and an internal grant from WUSM/MIR. Neither I nor any of the co-authors have any competing financial interests or any other conflicts of interest to disclose.

Disclaimer for work that was funded by NSSC: “This report was prepared as an account of work sponsored by an agency of the United States Government. Neither the United States Government nor any agency thereof, nor any of their employees, makes any warranty, express or limited, or assumes any legal liability or responsibility for the accuracy, completeness, or usefulness of any information, apparatus, product, or process disclosed, or represents that its use would not infringe privately owned rights. Reference herein to any specific commercial product, process, or service by trade name, trademark, manufacturer, or otherwise does not necessarily constitute or imply its endorsement, recommendation, or favoring by the United States Government or any agency thereof. The views and opinions of authors expressed herein do not necessarily state or reflect those of the United States Government or any agency thereof.”

Personal Acknowledgments

Many people have supported me during graduate school and earlier education. My parents Kent and Nanette have shown me love and encouragement throughout my life, which has included many phone calls and visits during graduate school. When I was a child, they sacrificed money and time for me to attend a private school and to get extra help in math, and this academic foundation, combined with their love, gave me strength and confidence for challenging myself academically. I am grateful to my wife Alicia Wooten, Au.D., who has loved and encouraged me and even been a role model during my final years of graduate school. To live with me in Saint Louis, Alicia accepted a job in Farmington, Missouri, while working half of her weekends in a local hospital and helping me with chores and errands. Needless to say, my complaining about how hard I worked as a graduate student plummeted thanks to her example of diligence.

Academically, I have had several role models who have contributed significantly to my development pre-high school (esp. David Longhofer, The Pembroke Hill School; Charlie McCalla) and during undergraduate research (esp. Chris Fischer, Ph.D., University of Kansas; Tim Lohman, Ph.D., WUSM). In my Ph.D. program, I am grateful to Frank Yin, M.D., Ph.D. for building a top-tier department from the ground up and, along with Shelly Sakiyama-Elbert, Ph.D., for guidance during my time in the Ph.D. program. Josh Swamidass, M.D., Ph.D. has also given me excellent advice for my academic and personal lives.

I am grateful to the Guariglia family for their friendship and for sharing their time, home, and food with me. Special appreciation goes to for the healthcare professionals at WUSTL Student Health Services and elsewhere in St. Louis for keeping me healthy, I could focus on my graduate work, especially during the past two years. For anyone not mentioned by name, many

people at church and elsewhere have been valuable sources of friendship and support during my time in St. Louis. Graduate school has been a challenging, humbling, and wonderful experience and a stimulating opportunity to dive deep into fascinating areas of science, engineering, and medicine. As a person of faith, I consider every person, resource, and opportunity mentioned in these acknowledgments as a blessing from God, who has been exceedingly generous to me.

Disclaimers

Portions of this dissertation come from manuscripts and articles to which other authors contributed writing (esp. B.C. Lewis) and revisions (esp. S.E. Lapi). S.E. Lapi and Alicia E. Wooten also assisted with revising this dissertation.

Unless otherwise indicated, values in this dissertation that were related to nuclear decay and emissions, as well as natural abundances of isotopes, were likely found via the National Nuclear Data Center (NNDC) at Brookhaven National Laboratory (BNL)^a. This center maintains several online services that access data from databases of original data from articles containing original measurements, articles that compile results from other articles, reports from government laboratories, and possibly other sources. The online services that we may have used from BNL/NNDC for decay data and natural abundances of isotopes included:

- The interactive Chart of Nuclides^b and NuDat 2.6^c, which gave credit to data from BNL/NNDC, which was based on Nuclear Wallet Cards^d and data from the International Network of Nuclear Structure and Decay Data (NSDD)^e Evaluators via the Evaluated Nuclear Structure Data File (ENSDF)^f.

^a National Nuclear Data Center (NNDC) at Brookhaven National Laboratory (BNL). Herman, M. (center head). Online: <<http://www.nndc.bnl.gov>>.

^b Chart of Nuclides. Sonzogni, A. (database manager and web programming). Online: <<http://www.nndc.bnl.gov/chart/>>.

^c NuDat, (current version: 2.6). Sonzogni, A. (database manager and web programming). Online: <<http://www.nndc.bnl.gov/nudat2/>>.

^d Tuli, J.K., 2011. Nuclear Wallet Cards. Johnson, T. (web manager); Pritychenko (original). Online: <<http://www.nndc.bnl.gov/wallet/>>.

^e International Network of Nuclear Structure and Decay Data Evaluators (NSDD), Nuclear Data Services, Nuclear Data Section (NDS), International Atomic Energy Agency (IAEA). Demetriou, P. (scientific secretary). Online: <<https://www-nds.iaea.org/nsdd/>>.

^f Evaluated Nuclear Structure Data File (ENSDF). Tuli, J. (database manager); Johnson, T. (web and programming). Online: <<http://www.nndc.bnl.gov/ensdf/>>.

- Medical Internal Radiation Dose (MIRD) format database^g, which accessed data from NSDD via ENSDF and possibly from a report written by T.W. Burrows in 1988^h.

Other data were also obtained via BNL/NNDC, such as cross-sections and thresholds for nuclear transmutation reactions and possibly other quantities as well, but these instances are cited within this dissertation.

^g Molecular Internal Radiation Dose (MIRD) format. Tuli, J.K. (database manager); Burrows, T.W. (web and programming).

^h Burrows, T.W., 1988. The Program RADLST. Report from BNL no.: BNL-NCS-52142.

Abstract of the Dissertation

Cyclotron Production and Biomedical Applications of the PET Isotope Manganese-52

by

Andrew Lake Wooten

Doctor of Philosophy in Biomedical Engineering

Washington University in St. Louis, 2016

Suzanne E. Lapi, Chair

Mark A. Anastasio, Co-Chair

Manganese is an important element for biomedical research because of its roles as an essential micronutrient and as a neurotoxin from chronic elevated exposure, as well as the role of manganese(II) as a paramagnetic core for contrast agents in T_1 -weighted magnetic resonance imaging (MRI). Using a radiotracer of manganese provides excellent sensitivity for studying these phenomena, but only ^{52}Mn met the criteria for our experiments: (1) a half-life ($t_{1/2}=5.6$ days) that was long enough to examine timepoints over several days, (2) a half-life that was short enough to emit sufficient counts for a realistic scan time, and (3) emitted radiation of a variety and energy that were appropriate for existing pre-clinical imaging modalities. Manganese-52 is well-suited for imaging with positron emission tomography (PET) because it emits positrons with a low energy ($E_{\beta^+}=242$ keV), which improves spatial resolution, and with an acceptable total abundance for positron emission ($I_{\beta^+}=29.6\%$) for adequate signal. Manganese-52 was produced on site by the $^{52}\text{Cr}(p,n)^{52}\text{Mn}$ reaction by bombarding non-enriched chromium (^{52}Cr : 83.8%) with ~ 13 MeV protons that were accelerated in the CS-15 cyclotron at Washington University School of Medicine in St. Louis. Bombardments of stacks of thin chromium metal foils were used to measure nuclear cross-sections for the $^{\text{nat}}\text{Cr}(p,x)^{52,52\text{m},54}\text{Mn}$ reactions, with results that agreed closely to simulations and published results. Manganese-52 was separated

chemically from bombarded chromium metal by cation- or anion-exchange chromatography. The separated product was used in experiments that included biodistribution by injection or inhalation, PET/CT or PET/MR in phantoms and rodents, and radiolabelling of a Mn(II)-based contrast agent for T_1 -weighted MRI. To reduce radiation dose to production personnel, we designed a remotely controlled, semi-automated module for the remote separation of ^{52}Mn inside a lead hot cell. This module was similar to other modules that we designed, built, and tested for the routine, scaled-up production of larger quantities of the PET isotopes ^{89}Zr and ^{86}Y . We anticipate that the module for ^{52}Mn will be completed, routine production of greater quantities of ^{52}Mn will be achieved, and this radioisotope will continue to be used to study and image the interesting aspects and behaviors of manganese chemistry.

Chapter 1. Introduction

1.1. The Paradigm of Molecular Imaging

The work in this dissertation includes non-imaging experiments related to the production and validation of a radiotracer for manganese, but, ultimately, the goal is to develop a radiotracer for manganese for *in vivo* nuclear imaging as an approach to molecular imaging. Radiotracers in biological and medical experiments has roots extending back to the earliest days of radionuclide production (Wagner, 2010) from cyclotrons (Ruben, et al., 1939) and nuclear reactors (Werner, et al., 1949), but molecular imaging as a whole extends beyond radiotracers and nuclear imaging. Only in recent decades, has the term molecular imaging been used and defined in 2007 as “[..]the visualization, characterization, and measurement of biological processes at the molecular and cellular levels in humans and other living systems.” (Mankoff, 2007). This definition goes on to explain that molecular imaging frequently generates quantitative images in two- or three-dimensions with time resolution and that this field is not limited to nuclear imaging, but also includes approaches based on nuclear magnetic resonance spectroscopy and imaging, ultrasound, optical luminescence imaging, and other imaging modalities (Mankoff, 2007).

One major advantage of molecular imaging for studying biological questions is that, unlike *in vitro* and *ex vivo* assays, biological processes can be examined *in vivo*—intact in a living organism. This is more realistic because cells are in their original microenvironment, including biological feedback loops (Gambhir, 2010). The ideal molecular imaging modality would have the ability to detect very low concentrations of molecular targets and to track cells, image with excellent spatial and temporal resolution, provide completely quantitative results, be

useful for imaging targets anywhere within cells and tissues at any realistic depth, as well as practical criteria of high throughput and low cost (Gambhir, 2010). Practically, the perfect modality does not exist, so the advantages and disadvantages of various modalities are considered when selecting an approach to a molecular imaging study.

Molecular imaging typically depends on endogenous or exogenous molecular imaging agents that can generate imageable signal(s) that reflect the location and other biological information inside an organism (Mankoff, 2007). Molecular imaging agents typically satisfy the tracer principle (Vanbrocklin, 2010) that was originally described by de Hevesy (Hevesy, 1923), which asserts that a probe in a small enough concentration will not disturb the (bio)chemistry of the system to which it is being applied for study. Probes that satisfy the tracer criteria can be trusted to provide information about a practically unperturbed system. Additionally, the chemical toxicity of such probes is not significant for non-chronic use, which dramatically increases the flexibility of selecting an imaging probe, such as radioisotopes of elements that would be toxic in greater concentrations. The tracer principle applies most readily to nuclear imaging because most biomedical radiotracers produce sufficient signal for detection and imaging from trace concentrations, but the tracer principle can apply to probes for other modalities of molecular imaging as well.

Frequently, the goal of developing a molecular imaging agent or other imaging technique is to translate the agent into clinical practice, but such translation requires navigating significant regulations associated with clinical studies (Gambhir, 2010). Some molecular imaging agents are not suitable for clinical use for various reasons (Gambhir, 2010), such as chemical toxicity, radiation dosimetry, attenuation of signal by human tissue, cost, or availability. Nevertheless, some agents that are only used in animal models can make valuable contributions to basic

research by expanding knowledge of biological questions (Gambhir, 2010). The development of ^{52}Mn as a radiotracer for PET imaging of manganese likely fits into this category.

1.2. Motivations for Studying Manganese

There are at least three biomedical roles and applications of manganese that make this element interesting for study, and they motivate the pursuit of quantitative detection and imaging of manganese. These roles include manganese (1) as an essential micronutrient that serves as a cofactor for important metalloenzymes, (2) as a neurotoxin that causes motor disorders following chronic inhalation of manganese, and (3) as a contrast agent for manganese-enhance magnetic resonance imaging (MEMRI). Although imaging of accumulated Mn(II) is possible by MRI, quantitative measurement and quantitative imaging of manganese is difficult, and MRI and CT contrast agents can require local concentrations as high as millimolar (10^{-3} M), compared to concentrations as low as picomolar (10^{-12} M) for the nuclear emission imaging techniques SPECT and PET (Lobatto, et al., 2011). The concentrations of contrast agents for MRI and CT are high enough that toxicity needs to be considered; however, this is not the case at the concentrations used for radiotracers for SPECT and PET.

The results presented from biological experiments in this dissertation (Chapter 3) could be useful as supporting information for environmental and occupational regulations, for designing PET studies utilizing ^{52}Mn , and for predicting biodistribution of manganese-based MR agents.

1.2.1. Natural Abundance of ^{52}Mn

Manganese is a micronutrient that is essential for human life in only trace amounts (Avila, et al., 2013; Averill and Eldredge, 2011). Ingestion of manganese is part of a healthy human diet, and deficiency is rare (OSU/LPI, 2010). Existing primarily in the Mn(IV) oxidation state in the earth's crust (Greenwood and Earnshaw, 1997), manganese is the third most abundant transition metal in the crust (TJNAF; Greenwood and Earnshaw, 1997), and is taken up by plants, where it is stored in produce and nuts (USDA/ARS) and utilized in green leaves as an oxidizer in photosynthesis (Greenwood and Earnshaw, 1997). Although manganese can form complexes in more oxidation states than any other first-row transition metal (Brown, et al., 2000; Greenwood and Earnshaw, 1997), Mn(II) is by far the most electrochemically stable oxidation state for manganese (Greenwood and Earnshaw, 1997) and the state that is predominantly used as an enzymatic cofactor. Nevertheless, free Mn(II) is efficiently cleared from the blood by the liver for excretion (Gibbons, et al., 1976), so Mn in the blood is found as Mn(III) bound to binding sites for Fe(III) on transferrin (Scheuhammer and Cherian, 1985; Gibbons, et al., 1976) or as Mn(II) bound to other serum proteins (Lau and Sarkar, 1984).

In humans, manganese is principally utilized as a co-factor for metalloenzymes in important biological processes, such as conversion of reactive oxygen species, gluconeogenesis, and the urea cycle (OSU/LPI, 2010). The body distributes manganese to tissues throughout the body (Yokel, 2009), where it can be taken into cells by transferrin-mediated endocytosis, the divalent metal transporter (DMT-1), and/or voltage-gated calcium channels (Roth, 2009). Manganese can also cross the blood-brain barrier by carrier-mediated transport (Yokel, 2009, 2006; Crossgrove, et al., 2003) and calcium-release activated channels (Yokel, 2009, 2006; Crossgrove and Yokel, 2005), where at least one of its roles is to moderate cellular uptake of the

neurotransmitter glutamate (Yin, et al., 2010; OSU/LPI, 2010). In this dissertation, we examine the biodistribution of manganese using ^{52}Mn as a radiotracer (Chapter 3).

1.2.2. Toxicology of Manganese

The necessity of manganese as a nutrient is sometimes overshadowed by its neurotoxic effects, resulting in *manganism* (Avila, et al., 2013), a condition that was first described in 1837 (Couper, 1837). In manganism, early-stage patients often present with psychiatric symptoms (Racette, et al., 2012a; Laohaudomchok, et al., 2011; Guilarte, 2010; Burton and Guilarte, 2009; Roth, 2006; Mergler, et al., 1994; Sjogren, et al., 1990; Rodier, 1955) that are sometimes referred to as “manganese madness” (Calne, et al., 1994). Later-stage patients develop symptoms of parkinsonism, including intellectual impairment, tremors, and rigidity similar to parkinsonism (Cersosimo and Koller, 2006; Josephs, et al., 2005; Hudnell, 1999; Sjogren, et al., 1996; Calne, et al., 1994; Mergler, et al., 1994; Rodier, 1955; Couper, 1837), with a few key differences from idiopathic Parkinson’s disease. It is believed that manganism typically results from chronic exposure to small doses of manganese, because manganese(II) chloride has relatively low acute toxicity in rodent models: $LD_{50}=0.22-3.59$ mmol/kg for intravenous injection (Gimi, et al., 2006; Elizondo, et al., 1991; Wolf, et al., 1985), $LD_{50}=1$ mmol/kg for intraperitoneal injection (Pan, et al., 2010), and $LD_{50}=7.50$ mmol/kg (tetrahydrate) for oral administration (MSDS, Sigma-Aldrich, 2015).

Nevertheless, neurotoxicity can result in animals or humans from chronic exposure to manganese in the water supply (Elsner and Spangler, 2005; Kondakis, et al., 1989), in ephedrine (methcathinone) produced using potassium permanganate (Sikk, et al., 2013; Sikk, et al., 2011; Sikk, et al., 2010; de Bie, et al., 2007; Sanotsky, et al., 2007), in the farming fungicides maneb or

mancozeb (J. Zhang, et al., 2003; Thiruchelvam, et al., 2000a; Thiruchelvam, et al., 2000b; Meco, et al., 1994; Morato, et al., 1989; Ferraz, et al., 1988; Israeli, et al., 1983; Israeli, et al.), or in gasoline containing the additive methylcyclopentadienyl manganese tricarbonyl (MMT) (Zheng, et al., 2000; Komura and Sakamoto, 1994, 1992; Clay and Morris, 1989). These sources have led government bodies to place limits on acceptable levels of non-occupational manganese at 0.05-0.5 mg/L in drinking water (Australia Department of the Environment, 2015; Williams, et al., 2012; U.S. E.P.A., 2009; Williams-Johnson, 1999) and 0.15-1,000 $\mu\text{g}/\text{m}^3$ in air (Williams, et al., 2012; Williams-Johnson, 1999).

However, certain types of metalworking can cause elevated risk of exposure to airborne manganese, so regulations have been placed on workplace exposure to airborne manganese (including from compounds, particles, and fumes) at 0.3-5 mg/m^3 (Australia Department of the Environment, 2015; Williams, et al., 2012; U.S. E.P.A., 2009; Williams-Johnson, 1999). Despite a few epidemiology studies—including some sponsored by industry—that dispute the existence of a link between metalworking and neurological disease (Fored, et al., 2006; Marsh and Gula, 2006; Fryzek, et al., 2005), there are still many reports of manganism in exposed workers (Searles Nielsen, et al., 2015; Gonzalez-Cuyar, et al., 2014; Racette, et al., 2012b; Racette, et al., 2012a; Harris, et al., 2011; Laohaudomchok, et al., 2011; Sriram, et al., 2010; Flynn and Susi, 2009; Marsh and Gula, 2006; Kenangil, et al., 2006; Fored, et al., 2006; Josephs, et al., 2005). Studies in these workers have demonstrated hallmark symptoms of manganism, and the accumulation of manganese in the brain can be so great that the current method for diagnosis of manganism is quantification of signal in the *globus pallidus* from T1-weighted MR imaging of the manganese that has accumulated in that region of the brain (Criswell, et al., 2012; Kenangil,

et al., 2006; Josephs, et al., 2005). In our biodistribution results (Chapter 3), we observe uptake of radiomanganese in the brain following intravenous administration of ^{52}Mn .

1.2.3. Manganese-Based Contrast Agents for Magnetic Resonance Imaging

An additional motivation for understanding the biodistribution of free manganese is that manganese(II) has been utilized in contrast agents for MR imaging. Manganese(II) is “high-spin” from its five unpaired valence electrons (Wolf, et al., 1985; Weinmann, et al., 1984), which shorten the spin-lattice time constant (T_1) for nearby ^1H nuclei, resulting in brighter signal when using a T_1 -weighted MR pulse sequence (Pan, et al., 2010; Rodriguez-Vargas, 2010; Silva and Bock, 2008), especially in anatomical regions with high water density. Gadolinium(III), by far the most commonly used cation in clinically approved T_1 contrast agents (Kahakachchi and Moore, 2010; Rodriguez-Vargas, 2010; Caravan, et al., 1999; Lauffer, 1987) requires higher coordination than Mn(II), giving Mn(II) better exchange kinetics with water molecules. However, Gd(III) has seven unpaired valence electrons, imparting Gd(III) with greater T_1 relaxivity ($R_1=1/T_1$) than Mn(II) in several different metal chelators.

The intravenous acute toxicity of Mn(II) chloride is similar to that of Gd(III) chloride ($LD_{50}=0.3-0.5$ mmol/kg in rodent models (Sigma-Aldrich, 2014; Bousquet, et al., 1988; Weinmann, et al., 1984)), but manganese ions are nevertheless interesting for certain MR applications, including utilizing the redox chemistry of chelated Mn(II/III) as an activatable probe of the redox environment in tissue (Boros, et al., 2015; Gale, et al., 2014; Loving, et al., 2013). Additionally, Mn complexes could serve as a safe alternative to Gd(III) (Brismar, et al., 2012; Thomsen, 2009; Mendonca-Dias, et al., 1983), which might pose a health risk to patients with renal insufficiency if Gd(III) dissociates from its chelator in the body (Pierre, et al., 2014;

Brismar, et al., 2012; Janus, et al., 2010; Ledneva, et al., 2009; Thomsen, 2009), since free Gd(III) is excreted through the kidneys, but free Mn(II) is excreted through the liver (Mendonca-Dias, et al., 1983).

For these reasons, various complexes of Mn(II) (Zhu, et al., 2014) and Mn(III) (Cheng, et al., 2014; Pierre, et al., 2014; Qazi, et al., 2014) are being developed, numerous kinds of Mn-doped inorganic and organic nanoparticles are in the *in vitro* and pre-clinical stages (Pan, et al., 2010, 2009, 2008), and oral administration of liquids containing Mn(II) has been tested in humans (Brismar, et al., 2012; Hiraishi, et al., 1995). So far, the only manganese-based MR contrast agent to reach the market in the United States was Teslascan® (*mangafodipir*; manganese(II)-dipyridoxyl diphosphate (Mn-DPDP); Amersham plc, Amersham, United Kingdom), which was used for detecting colorectal metastases in the liver (Elizondo, et al., 1991; Rocklage, et al., 1989), and was withdrawn in the United States in 2003 because of low demand (not safety concerns). Since MRI is not inherently as quantitative as PET, and since MEMRI is not as widely studied as Gd-based imaging, it would be useful to “authentically” radiolabel manganese-based MR contrast agents with radiomanganese (Coenen, et al., 2014; Klein, et al., 2005) for quantitative confirmation of their biodistribution—by dissection, autoradiography, and/or *in vivo* imaging.

1.3. Radioactive Decay, Detection, and In Vivo Imaging

Quantifying radiotracers is very sensitive and precise, and offers opportunities for *in vivo* imaging. At least twenty-seven isotopes of manganese have been discovered, one of which is stable. The twenty-six remaining isotopes decay by numerous different modes of radioactive

decay, resulting in many different types of particle and energy emissions. Based on techniques for detection and imaging and on half-lives that are useful for biomedical experiments, there are only a few radioisotopes that are potentially valuable for biomedical applications, and, for the majority of this dissertation, we will focus on cyclotron production and biomedical applications of ^{52}Mn in particular.

1.3.1. Nuclear Decay and Radiation

There are many different modes of nuclear decay, all of which basically involve a radioactive isotope seeking a more stable, less energetic state. Nuclear decay typically results in the radioactive parent isotope releasing energy as particles (including positrons), gamma-rays, or in other forms, as the nucleus transforms into a daughter isotope or isomer (which itself may be stable or radioactive). Numerous types of radiation can be emitted—directly or indirectly—by nuclear decay, and some of the most common kinds are summarized in Table 1.1.

Table 1.1. Summary of radiation emitted directly or indirectly by radioactive decay.

Type of Radiation	Charge	Mass	Primary Interaction(s) with Matter Following Scattering off Orbital Electrons
α	+2	4.00 u	Ionization (sometimes producing Cherenkov light)
β^+ or e^-	-1	5.5e-4 u	Ionization (sometimes producing Cherenkov light) Bremsstrahlung radiation
Photon: from γ decay	None	0	Pair production (>1.02 MeV) Compton effect Photoelectric (<500 keV)
Photon: from β^+ annihilation			Photoelectric effect
Photon: X-ray from e^- capture			Photoelectric effect

(Sources: ICSU/CODATA; Royal Society of Chemistry/Radiochemical Methods Group.)

1.3.2. Non-Imaging and Ex Vivo Options for Detecting Radiation in Biomedical Research

Although this dissertation focuses the application of a radioisotope of manganese for *in vivo* imaging, it is important to consider alternative techniques that could also study the behavior of manganese by detecting radiomanganese. This section discusses a few common non-imaging techniques that are used for detecting radiation in medical radiochemistry.

Ionization is a mechanism of interaction between radiation and matter that is commonly used for detecting and measuring radiation. Ionization of an atom occurs when the energy of the radiation—particles, X-rays, or gamma-rays—is greater than the energy required to remove an electron from an atom (different for 1st, 2nd, 3rd, etc. electrons of an atom). Following ionization, in a detector, the resulting free electrons are attracted to an anode, and the cations to a cathode, and the resulting current is measured by an electrometer circuit and is correlated to the ionizing radiation that was originally detected. Gases are commonly used as the ionization medium because of faster movement to the electrodes. The incident radiation that is best measured by ionization is usually gamma-rays, beta particles, and annihilation photons.

Detectors that operate on this principle are classified as gaseous ionization detectors. Typically gaseous ionization detectors (dose calibrators) cannot measure the energy of radiation, so accurately converting radiation into units of radioactivity requires the sample to only emit radiation from one radioisotope that is known, as well as calibrating the device itself (Appendix A) or by calculations.

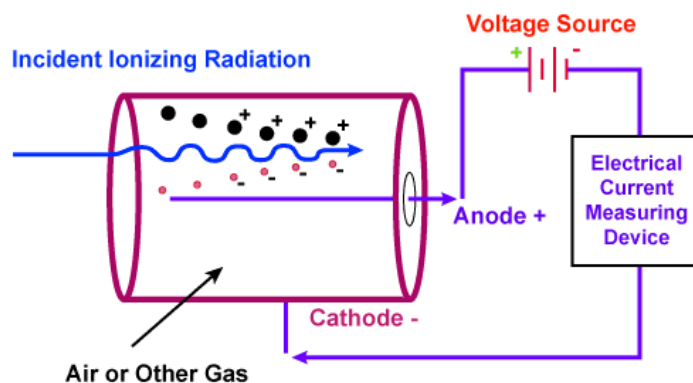


Figure 1.1. Illustration of the mechanism behind ionization chambers.
 (Image courtesy of EQUIPCO. Used with permission.)

Gamma-ray energy can be measured by scintillation detectors and semiconductor detectors. The most common type of scintillation detector uses a NaI crystal that has been doped with Tl, and this crystal produces a small amount of visible light when it encounters a photon with sufficient energy. The crystal is attached to the window of a photomultiplier tube (PMT), which detects the light in the crystal, converts it to an electrical pulse, and amplifies this pulse until it is large enough to be counted by the electronics connected to this system (Figure 1.2). The brightness of the light in the crystal and the pulse height in the PMT are correlated to the energy of the incident photon, so this energy can be estimated. A NaI(Tl) detector is used in many gamma counters, including the ones that we used for quantifying radioactivity in our *ex vivo* biodistribution experiments (Chapter 3), and this kind of detector was also used in the radiation detector used in the radiation detector attached to our high-pressure liquid chromatography (radio-HPLC) system.

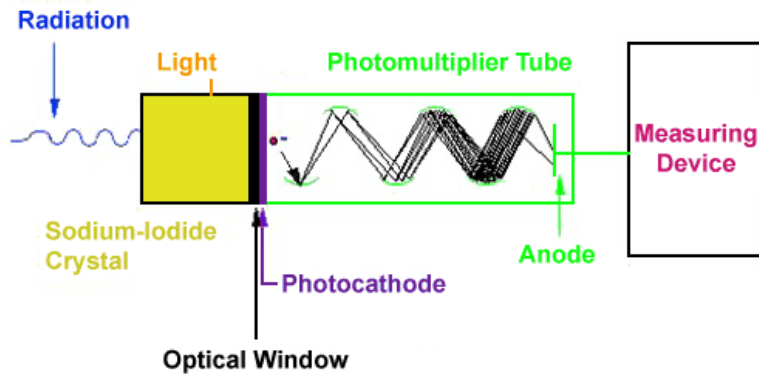


Figure 1.2. Illustration of the mechanism underlying scintillation radiation detectors.
 (Image courtesy of EQUIPCO. Used with permission.)

The most common type of semiconductor detector in recent years is the high-purity germanium (HPGe) detector used for gamma-ray spectroscopy in Section 2.2.4, which detects photons while the HPGe crystal is maintained at a high voltage. When a photon enters the crystal, it creates numerous electron-hole pairs that are quickly pulled toward the anode and cathode, respectively, by the large bias on the crystal, creating an electric pulse (Figure 1.3). The number of electron-hole pairs and the magnitude of the electric pulse are proportional to the energy of the incident photon, so this detector can also detect photon energy with much better energy resolution than the NaI(Tl) detector.

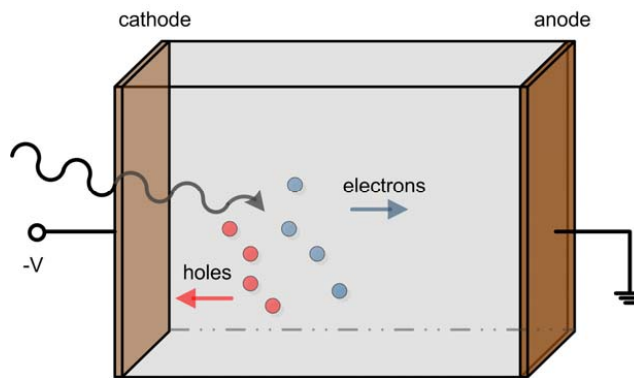


Figure 1.3. Illustration of the mechanism underlying semiconductor radiation detectors.
 (Image from Q. Zhang, et al., 2013. Creative Commons.)

Finally, autoradiography presents a method for two-dimensional mapping of the distribution of radioactivity. This technique is best applied to mapping radioactivity in a planar region, such as in a thin layer chromatography (TLC) plate, thinly sectioned *ex vivo* tissues, or other applications. One common method for autoradiography utilizes a storage phosphor screen, which consists of a layer of microparticles of BaFBr doped with Eu^{2+} . Incident radiation of sufficient energy will excite electrons in Eu^{2+} to a highly mobile state, causing Eu^{2+} to oxidize to Eu^{3+} , and BaFBr to be reduced to BaFBr^- . These new states are maintained for up to a few weeks until the screen is read in a scanner that excites the screen with 635 nm light and, using a band-pass filter, measured the blue light emitted by the screen at wavelengths surrounding ~ 390 nm. The intensity of this light at each spot on the screen is proportional to the radioactivity originally detected by the screen at that location, and this signal can be mapped in the control software to form images. For anatomical imaging corresponding to the autoradiography, the tissue sections are imaged in bright field by photography. Autoradiography presents a useful option for mapping distribution of radioactivity that emits various types and energies of radiation, including gamma-rays and charged particles. Table 1.2 summarizes the different mechanisms and instruments that were discussed that could be used to detect and quantify radiomanganese in experiments that do not require *in vivo* nuclear emission imaging.

Table 1.2. Summary of non-imaging technologies for detecting radioactivity.

	Typical Particles Detected^a	Examples of Applications
Gaseous Ionization Detectors		
Ionization chamber	γ	Dose calibrator, survey meters
Scintillation counter	γ	NaI(Tl) gamma spectroscopy, gamma counter, detector for radio-HPLC
Semiconductor detector	γ	HPGe detector
Storage phosphor screen	α, β, γ, n	Autoradiography for radioTLC plates, sectioned tissues, whole body autoradiography of sliced small animals

^aDetection of positrons is not listed specifically in this table, but the 511 keV annihilation photons can be detected by any detector that is capable of detecting gamma-rays with energy of 511 keV.

1.3.3. Techniques for In Vivo Imaging of Emitted Radiation

Despite the useful characteristics of these detectors, our goal was to perform *in vivo* nuclear emission imaging. In general, for *in vivo* imaging applications, the best emissions are photons that have either a low energy of or a specific known energy, specifically 511 keV photons that result when a positron is emitted then annihilates with a nearby electron (Section 1.3.3.2). Photons with energy 30-250 keV (Peterson and Furenlid, 2011) have an energy that is great enough that, on average, they are not completely attenuated within a body, but low enough to be useful for imaging modalities based on gamma cameras (i.e., planar scintigraphy and SPECT). The 511 keV photons are useful for PET imaging, which uses a filter that will only count photons with an energy surrounding 511 keV (~350-650 keV (Phelps, et al., 2006)). This ability to resolve the energy of photons and then select signal from photons in a specific energy range enables rejection of counts from photons that originated from another location and have lost energy from significant scattering, thereby increasing the signal-to-noise ratio (SNR) in the

imaging. These factors are important to consider when selecting radioisotopes for experiments because of the different kinds of radiation required for different nuclear imaging modalities.

1.3.3.1. Non-PET Nuclear Emission In Vivo Imaging Modalities

For isotopes that emit photons in the 30-250 keV window, gamma cameras present a very useful technology for detecting radiation to produce signals that can be reconstructed into images. Gamma cameras, also known as an Anger camera after its inventor, operate on similar principles as scintillation counters (Section 1.3.2) and in some ways are simply an array of these counters that are used to produce two-dimensional maps of radiation emitted from the imaging subject. Gamma cameras are the detectors behind the modalities of conventional nuclear medicine: planar scintigraphy and single photon emission computed tomography (SPECT).

1.3.3.2. Positron Emission Tomography

The positron emission mode of nuclear decay is of particular importance in medical imaging. In a typical medium, positrons will scatter inelastically off orbital electrons, causing ionization of atoms, over a range of only a few millimeters before annihilating with an electron. This annihilation converts the mass of the positron and the electron into two photons that are released at 511 keV each in directions that are almost exactly 180° from each other due to conservation of momentum. The physics of positron annihilation, particularly the specific direction and energy of the annihilation photons, form the basis of positron emission tomography (PET), which is an imaging modality in clinical nuclear medicine.

PET has important advantages over the more traditional nuclear medicine modalities based on its underlying physics. PET is optimized to only image the distribution of annihilation

events from positrons, which gives PET high specificity in terms of signal. This signal specificity relies on a few special aspects of positron emission and annihilation:

- (1) Positrons in tissue have a short range before annihilation.
- (2) The photons emitted from annihilation are always $\sim 180^\circ$ in opposite directions.
- (3) The annihilation photons always have energy of 511 keV.
- (4) Both photons, travelling through different amounts of tissue and air, have high enough velocities that they will reach a ring of detectors quickly and with very little difference in time of arrival (i.e., in coincidence).

These characteristics mean that determining the concentration of annihilation events is related to the concentration of parent nuclei. Furthermore, the location of annihilation events in each slice can be detected by a ring of detectors that only count photons with energy in a range surrounding 511 keV and only when another photon is detected in a detector located $\sim 180^\circ$ away within a very short time window (on the order of nanoseconds). The mechanism of PET is illustrated in Figure 1.4.

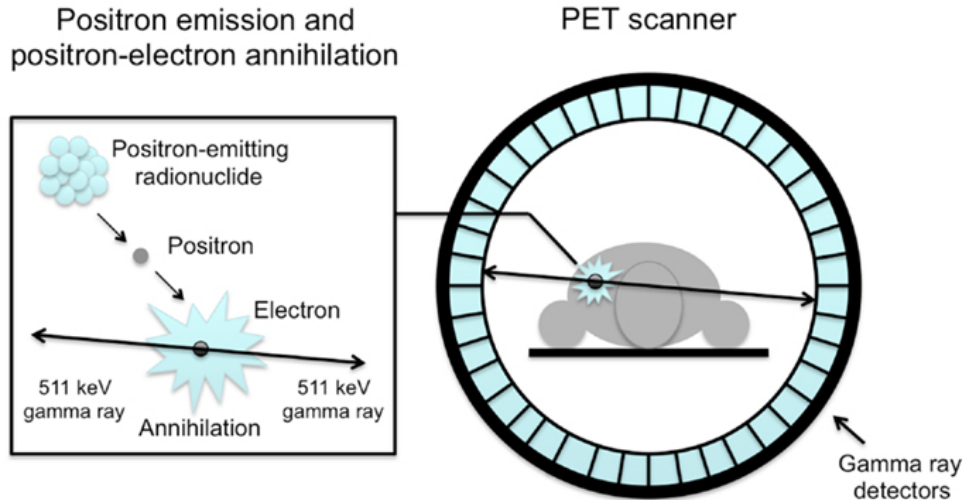


Figure 1.4. Illustration of the physics of positron emission tomography.
 (Image: van der Veldt, et al., 2013. Creative Commons.)

After detecting coincident photons that meet these criteria, the PET system can define a line of response (LOR) for those two photons. As the number of counts of coincident photons increase during a scan the many LORs that are created begin to intersect in regions with the highest density of annihilation events during the scan time, which closely describes areas that had high concentration of positron emitting nuclei during the scan. This information can be acquired as two-dimensional regions if only a single ring of detectors is used for each image slice, or as three-dimensional regions if multiple rings are used. At this point, various signal processing algorithms can be applied to improve the image that will result from image reconstruction. The image slices are reconstructed into a three-dimensional tomograph that reflects the distribution of a PET radiotracer *in vivo*.

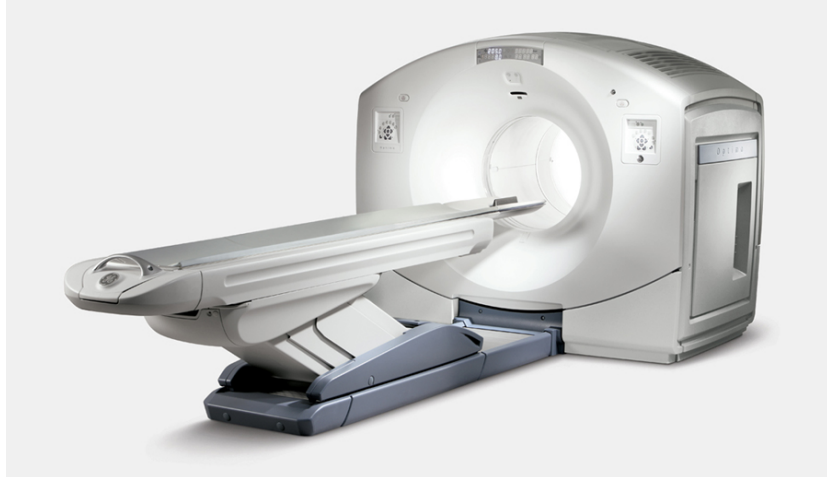


Figure 1.5. Photograph of a General Electric (GE) Optima PET/CT 560 human scanner.
(Image courtesy of GE Healthcare. Used and adapted with permission.)

Detailed anatomical imaging is provided by computed tomography (CT) or magnetic resonance imaging (MRI) and is frequently co-registered with a PET image in multimodality techniques known as PET/CT or PET/MR, respectively. When two-dimensional presentation is desired, the co-registered tomographs are often converted to a maximum intensity projection (MIP) in the direction of a selected point of view. Figure 1.6 shows examples for PET, CT, and MR images (with fusion) from a 62 year-old woman with multiple myeloma (Fowler, et al., 2013). Signal from PET clearly shows a lesion in the region of the left shoulder that was avid for [^{18}F]-fluorodeoxyglucose (^{18}F -FDG), which is a simple analog for glucose that has been radiolabelled with the positron-emitting radionuclide ^{18}F . ^{18}F -FDG is currently the most commonly used radiotracer for PET worldwide, and it can detect regions of high glucose consumption, such as tumors that demonstrate sufficient contrast in PET imaging by not being near areas of naturally high signal, especially the brain and bladder.

The physics of PET translates into advantages for this modality, including extremely high sensitivity because all radiation is rejected except for that which has a specific energy,

directionality, and coincidence timing. The sensitivity of PET is on the order of picomolar concentration of radiotracer, and better sensitivity means that much less total mass of a contrast agent needs to be administered, which can decrease concerns for chemical toxicity and radiation dosimetry in patients. Although nuclear imaging in general has poor resolution compared to other medical imaging modalities such as CT or MRI, PET generally boasts better spatial resolution than SPECT.

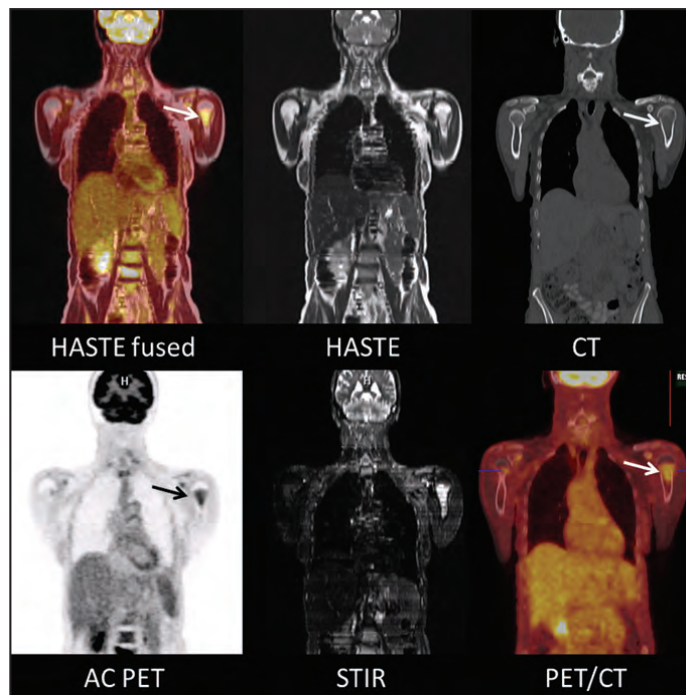


Figure 1.6. Lesion from multiple myeloma viewed with FDG-PET, CT, and MR.

Arrow: lesion; AC: attenuation correction; HASTE, STIR: pulse sequences for MRI. (Image: Fowler, et al., 2013. Reprinted with permission of Anderson Publishing Ltd. From Fowler, K.; McConathy, J.; Khanna, G.; Dehdashti, F.; Benzinger, T.L.S., et al., 2013. Simultaneous PET/MRI acquisition: Clinical potential in anatomically focused and whole-body examinations, Applied Radiology, pp. 9-14. ©Anderson Publishing Ltd.)

1.4. Selection of ^{52}Mn as a Radiotracer

A need exists for a tracer of manganese that is radioactive, detectable, and imageable, specifically by PET, at timepoints of hours and days. The radioisotope that best satisfied our criteria was ^{52}Mn , which can be produced on-site at our medical center using cyclotrons from a low-energy, biomedical cyclotron.

1.4.1. Selection Criteria for a Radioisotope of Manganese

Many different factors, including scientific, engineering, facilities, and cost reasons contribute to the selection of a radioisotope for experiments. These considerations result from the following factors related to the production of medical isotopes: capabilities and limitations of radiation detection and imaging, decay properties and radiation emissions of radioisotopes, requirements for nuclear reaction channels, and production costs associated primarily associated with target materials and beam time for a cyclotron. This section discusses these selection factors, which are also summarized in Table 1.3.

Based on the technologies discussed earlier (Sections 1.3.2-1.3.3), many different types of emitted radiation can be useful for imaging and non-imaging applications. For both imaging and non-imaging technologies, these different kinds of radiation can be detected directly or indirectly. However, when selecting the radionuclide, it also must emit the desired radiation at a sufficient total intensity (I_{tot}), which is the total fraction of radionuclides that will emit a particular radiation type, at a certain energy as a part of their decay to a daughter nuclide.

Table 1.3. Selection considerations for radionuclides in biomedical experiments.

Criteria	Application	Typical Choice
Radiation emitted can be detected	Ionization/Proportional counter	γ
	Semiconductor	γ
	Phosphor screen	γ
	Scintillation: counter	γ
	Scintillation: scintigraphy/SPECT	γ ($E_\gamma \sim 30\text{-}250$ keV)
	Scintillation: PET	511 keV coincident photons (from positron annihilation)
Nuclear half-life matched to biological half-life	Small molecules	Minutes-Hours
	Peptides, antibody fragments	Hours
	Intact antibodies, nanoparticles	Days
	Long-term biodistribution	Months
Production routes	Generator (from nuclear reactor)	
	Low-energy cyclotron	
	High-energy ion accelerator	
	Nuclear reactor	

It is also important to consider the timescale of the experiment that will be utilizing the radiotracer. Most benchtop chemistry and *in vivo* experiments require isotopes with half-life for nuclear decay ($t_{1/2}$) of at least 1 minute for very quick experiments and less than 1 year for the longer tracer experiments. In particular, radiolabelled compounds for *in vivo* experiments should use radiolabels that correspond to the biological half-life of the targeting agent, meaning the time from administration for one-half of the dose to either reach its target or to be excreted. These targeting times can vary over a broad range, typically increasing with the size of the radiolabelled compound: roughly minutes for small molecules, hours for peptides and antibody fragments, and days for nanoparticles and intact antibodies. It is essential to select a radiolabel with a half-life that is long enough for sufficient radioactivity to remain at the desired timepoints post-administration for detection or imaging. *In vivo* imaging studies require more emission signal than simple counting and spectroscopy experiments, so the half-life of an imaging

radioisotope should also be short enough to provide a sufficient rate of nuclear decay to produce enough counts in a reasonable scan time.

A final major consideration for radioisotope selection is the cost and ease of acquisition or in-house production. Many radioisotopes with sufficient market demand are available commercially, including numerous long-lived radiotracers and several isotopes for SPECT and PET, even the non-traditional PET isotopes ^{64}Cu , ^{89}Zr , and ^{124}I . Certain government laboratories and universities are capable of producing a variety of radioisotopes from large instruments, such as nuclear reactors, linear accelerators, ion beams, and spallation targets. These instruments are necessary for isotope production via certain nuclear reaction channels that require different incident particles and/or higher incident energies, and these facilities supply commercial vendors with large batches of parent isotopes for generators, alpha- and beta-emitting radioisotopes for therapy, and certain SPECT isotopes.

However, the vast majority of production of PET isotopes is performed by proton bombardment from a low-energy cyclotron located on-site at academic or commercial medical centers. The cost of target material can be reduced by selecting isotope products and reaction channels that require target nuclei with high natural abundance. Due to the costs charged for isotopically enriched materials, even slight enrichment of the most abundant metals can cost more than naturally monoisotopic metals. Recovery and recycling of target material for future productions, which can be a time consuming process can also help keep costs down. A good example of a cost-efficient cyclotron target is production of the PET isotope ^{89}Zr by the $^{89}\text{Y}(p,n)$ reaction. Natural yttrium is monoisotopic (as ^{89}Y), affordable, and, therefore, the dissolved target material does not necessitate recovery from its chemical processing and can simple be disposed as waste.

1.4.2. Potentially Useful Radioisotopes of Manganese

There are several radioisotopes of manganese that satisfy broad criteria for being useful for radiochemistry experiments, and a smaller number satisfy practicality criteria for half-life and production. Nuclear decay properties for several of these potentially useful radioisotopes of manganese are summarized in Table 1.4. The radioisotope ^{54}Mn emits positrons and beta particles that might be useful for various applications, but the intensities are $I_{\beta^+}=5.8\times 10^{-7}\%$ and $I_{\beta^-}=2.9\times 10^{-4}\%$, which are much too low to be practically useful. However, ^{54}Mn also emits a gamma-ray at an energy ($E_{\gamma}=835\text{ keV}$) that is not suitable for *in vivo* imaging but very feasible for several non-imaging detection methods, and the intensity of this gamma-ray is more than sufficient ($I_{\beta^+}=99.98\%$). Many other radioisotopes of manganese emit radiation that meets the criteria described above, yet only a few of these radioisotopes satisfy the half-life requirements for most radiolabelling and *in vivo* experiments. The radioisotopes $^{46-52,46\text{m},50\text{m},52\text{m},54}\text{Mn}$ all emit positrons, and the intensities exceed, to varying degrees, the intensities of several other PET radiometals: $I_{\beta^+}>99\%$ for $^{46-50}\text{Mn}$, $I_{\beta^+}>95\%$ for $^{51,52\text{m}}\text{Mn}$, and $I_{\beta^+}=29.6\%$ for ^{52}Mn . However, only positron emitters $^{50\text{m},51,52,52\text{m}}\text{Mn}$ have nuclear half-lives that are in the realistic range to be of practical use in terms of half-life of nuclear decay.

Table 1.4. Comparison of decay properties of radioisotopes of manganese.

Applications	Candidate Isotopes	Half-Life ^a	Pertinent Emission ^a
Long-lived gamma-emitter	⁵⁴ Mn	312 days	834.8 keV (99.98%)
PET	⁴⁶⁻⁵⁰ Mn	<0.5 sec	Various (≥99%)
	^{50m} Mn	1.8 min	1.54 MeV (106%)
	⁵¹ Mn	46.2 min	963 keV (97.1%)
	^{52m} Mn	21.1 min	1.17 MeV (95.0%)
	⁵² Mn	5.6 days	242 keV (29.6%)
SPECT		None	
Radiotherapy	⁵⁶ Mn	2.6 hours	833 keV (99.9%)

Percentages reflect total intensities for each type of emission. (Data accessed via:
^aBNL/NNDC/ENSDF.)

Only ⁵²Mn satisfied our preferences for a positron-emitting radioisotope of manganese with a relatively long half-life, so we selected ⁵²Mn as the radiotracer for manganese behavior in our experiments. This isotope had the additional benefit that it can be produced in-house by proton bombardment from a low-energy cyclotron, instead of requiring a large-scale ion accelerator or a nuclear reactor.

1.4.3. Characteristics of ⁵²Mn

Manganese-52 is unique in its half-life of several days which, was ideal for our applications. The total intensity and average energy of positron emission makes ⁵²Mn a strong candidate for PET imaging; the abundance of gamma-rays make it a good candidate for non-imaging radiotracer experiments where a detector for gamma-rays is used. Figure 1.7 and Table 1.5 show simplified decay data for ^{52,52m}Mn.

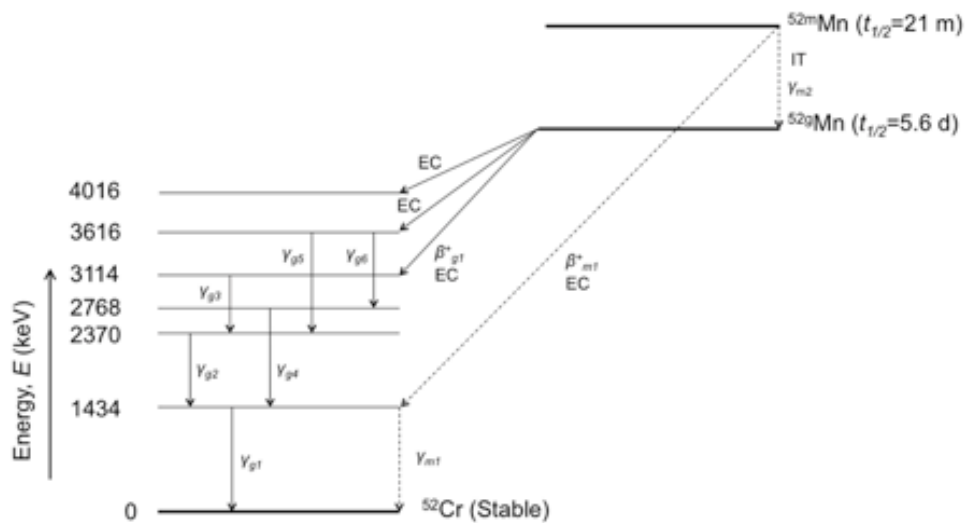


Figure 1.7. Simplified level decay scheme for $^{52,52m}\text{Mn}$.
 Only showing emissions with $I_{\text{tot}} > 1\%$. (Data accessed via BNL/NNDC/ENSDF.)

Table 1.5. Data for radioactive decay of ^{52}Mn .

^{52m}Mn			^{52}Mn		
<u>Modes:</u>			<u>Modes:</u>		
ϵ decay		98.3%	ϵ decay		100.0%
β^+ emission		95.0%	β^+ emission		29.6%
e^- capture		3.3%	e^- capture		70.4%
Isomeric Transition		1.8%			
<u>β^+ and γ Emissions:</u>			<u>β^+ and γ Emissions:</u>		
	Energy (keV)	Intensity (%)		Energy (keV)	Intensity (%)
β^+_{m1}	1174	94.8%	β^+_{g1}	242	29.6%
	Mean: 1172	Total: 95.0%		(only β^+ spectrum)	
γ_{m1}	1434	98.3%	γ_{g1}	1434	100.0%
γ_{m2}	378	1.7%	γ_{g2}	936	94.5%
			γ_{g3}	744	90.0%
			γ_{g4}	1334	5.1%
			γ_{g5}	1246	4.2%
			γ_{g6}	848	3.3%

(Data accessed via BNL/NNDC/ENSDF.)

1.4.4. Comparison of ^{52}Mn to Other PET Isotopes

Our primary motivation for using ^{52}Mn for PET imaging is to study the interesting *in vivo* behavior of manganese and manganese-labeled compounds. The radioactive decay characteristics of ^{52}Mn as compared to other PET isotopes is provided in Table 1.6.

Table 1.6. Comparison of decay characteristics of ^{52}Mn to other PET radionuclides.

	Half-Life ^a	Positron Emission		Gamma Radiation
		Weighted Average Energy ^a (keV)	Total Intensity ^a	Gamma Factor ^b ($\text{R}\cdot\text{cm}^2\cdot\text{mCi}^{-1}\cdot\text{h}^{-1}$)
^{52}Mn	5.6 d	242	29.6%	18.4
^{124}I	4.2 d	820	22.7%	6.6
^{89}Zr	3.3 d	396	22.7%	6.6
^{86}Y	14.7 h	660	31.9%	18.9
^{64}Cu	12.7 h	278	17.6%	1.1
^{18}F	110 m	250	96.7%	5.7
^{68}Ga	68 m	830	88.9%	5.4
^{11}C	20 m	386	99.8%	5.9

(^aData accessed via BNL/NNDC/ENSDF. ^bData from: Smith and Stabin, 2012.)

In terms of acquiring the radionuclide needed for a PET study, Table 1.7 compares the routes for producing the PET isotopes that were listed in Table 1.6.

Table 1.7. Comparison of ^{52}Mn to other PET radionuclides.

	Production	
	Most Common Target	Target Natural Abundance ^a
^{52}Mn	$^{52}\text{Cr}(p,n)$ (Solid)	83.8%
^{124}I	$^{124}\text{Te}(p,n)$ (Solid)	4.7%
^{89}Zr	$^{\text{nat}}\text{Y}(p,n)$ (Solid)	100.0%
^{86}Y	$^{86}\text{Sr}(p,n)$ (Solid)	9.9%
^{64}Cu	$^{64}\text{Ni}(p,n)$ (Solid)	0.9%
^{18}F	$^{18}\text{O}(p,n)$ (Liquid)	0.2%
^{68}Ga	^{68}Ge (Generator)	-
^{11}C	$^{14}\text{N}(p,\alpha)$ (Gas)	99.6%

(^aData accessed via: BNL/NNDC/ENSDF.)

In summary, the $^{52}\text{Cr}(p,n)$ reaction provides a route for producing ^{52}Mn , an imageable radiotracer with a half-life of several days, for experiments that depend on the chemistry of manganese.

1.5. Thesis and Scope of this Dissertation

The thesis for this dissertation is: Manganese-52 (^{52}Mn) is feasible to produce using a biomedical cyclotron and simple chemical isolation that can be automated, and ^{52}Mn can be a useful PET radioisotope for detecting and imaging the chemical and biological behavior of Mn(II) cations, salts, and radiolabelled compounds. The scope for this dissertation can best be grouped into four categories that are reflected in the chapters herein:

- Nuclear cross-sections and chemical separation (Chapter 2)
- Biodistribution and PET imaging of ^{52}Mn (Chapter 3)
- Applications of ^{52}Mn in PET/MR imaging (Chapter 4)
- Remotely-controlled modules for the isolation of PET radiometals (Chapter 5)

1.6. References

- Australian Government, Department of the Environment, National Pollutant Inventory, accessed: 2015. Manganese & compounds.
- Averill, B.A.; Eldredge, P., 2011. General Chemistry: Principles, Patterns, and Applications. Flat World, Available online.
- Avila, D.S.; Puntel, R.L.; Aschner, M., 2013. Manganese in Health and Disease, in: Sigel, A.; Sigel, H.; Sigel, R.K.O. (Eds.), Interrelations between Essential Metal Ions and Human Diseases. Springer Science+Business, Dordrecht, The Netherlands, pp. 199-227.

- Boros, E.; Gale, E.M.; Caravan, P., 2015. MR imaging probes: design and applications. Dalton transactions 44, 4804-4818.
- Bousquet, J.C.; Saini, S.; Stark, D.D.; Hahn, P.F.; Nigam, M., et al., 1988. Gd-DOTA: characterization of a new paramagnetic complex. Radiology 166, 693-698.
- Brismar, T.B.; Kartalis, N.; Kylander, C.; Albiin, N., 2012. MRI of colorectal cancer liver metastases: comparison of orally administered manganese with intravenously administered gadobenate dimeglumine. European radiology 22, 633-641.
- Brown, T.L.; Lemay, H.E.; Bursten, B.E., 2000. Chemistry: The Central Science. Prentice Hall, Upper Saddle River, New Jersey, United States.
- Burton, N.C.; Guilarte, T.R., 2009. Manganese neurotoxicity: lessons learned from longitudinal studies in nonhuman primates. Environmental health perspectives 117, 325-332.
- Calne, D.B.; Chu, N.S.; Huang, C.C.; Lu, C.S.; Olanow, W., 1994. Manganism and idiopathic parkinsonism: similarities and differences. Neurology 44, 1583-1586.
- Caravan, P.; Ellison, J.J.; McMurry, T.J.; Lauffer, R.B., 1999. Gadolinium(III) chelates as MRI contrast agents: Structure, dynamics, and applications. Chem. Rev. 99, 2293-2352.
- Center for Clinical Imaging Research (CCIR), Washington University School of Medicine in St. Louis (WUSM).
- Cersosimo, M.G.; Koller, W.C., 2006. The diagnosis of manganese-induced parkinsonism. Neurotoxicology 27, 340-346.
- Cheng, W.; Ganesh, T.; Martinez, F.; Lam, J.; Yoon, H., et al., 2014. Binding of a dimeric manganese porphyrin to serum albumin: towards a gadolinium-free blood-pool T1 MRI contrast agent. Journal of biological inorganic chemistry : JBIC : a publication of the Society of Biological Inorganic Chemistry 19, 229-235.
- Clay, R.J.; Morris, J.B., 1989. Comparative pneumotoxicity of cyclopentadienyl manganese tricarbonyl and methylcyclopentadienyl manganese tricarbonyl. Toxicology and applied pharmacology 98, 434-443.
- Coenen, H.H.; Buchholz, M.; Spahn, I.; Vanasschen, C.; Ermert, J., et al., 2014. Towards authentically labelled bi-modal PET (SPECT)/MR-probes. Springer, p. A79.
- Committee on Data for Science and Technology (CODATA), International Council of Science (ICSU). The NIST Reference on Constants, Units, and Uncertainty. Accessed via: Physical Measurement Laboratory, National Institute of Standards and Technology, (NIST). Accessed: 2015.
- Couper, J., 1837. On the effects of black oxide of manganese when inhaled into the lungs. Br. Ann. Med. Pharm. Vital. Stat. Gen. Sci. 1, 41-42.
- Criswell, S.R.; Perlmutter, J.S.; Huang, J.L.; Golchin, N.; Flores, H.P., et al., 2012. Basal ganglia intensity indices and diffusion weighted imaging in manganese-exposed welders. Occupational and environmental medicine 69, 437-443.
- Crossgrove, J.S.; Allen, D.D.; Bukaveckas, B.L.; Rhineheimer, S.S.; Yokel, R.A., 2003. Manganese distribution across the blood-brain barrier. I. Evidence for carrier-mediated influx of manganese citrate as well as manganese and manganese transferrin. Neurotoxicology 24, 3-13.

- Crossgrove, J.S.; Yokel, R.A., 2005. Manganese distribution across the blood-brain barrier. IV. Evidence for brain influx through store-operated calcium channels. *Neurotoxicology* 26, 297-307.
- de Bie, R.M.; Gladstone, R.M.; Strafella, A.P.; Ko, J.H.; Lang, A.E., 2007. Manganese-induced Parkinsonism associated with methcathinone (Ephedrone) abuse. *Archives of neurology* 64, 886-889.
- Elizondo, G.; Fretz, C.J.; Stark, D.D.; Rocklage, S.M.; Quay, S.C., et al., 1991. Preclinical evaluation of MnDPDP: new paramagnetic hepatobiliary contrast agent for MR imaging. *Radiology* 178, 73-78.
- Elsner, R.J.; Spangler, J.G., 2005. Neurotoxicity of inhaled manganese: public health danger in the shower? *Medical hypotheses* 65, 607-616.
- EQUIPCO Rentals Corp. and EQUIPCO Sales & Service Corp. Introduction to Radiation Detectors. Online: <<http://www.equipcervices.com/support/tutorials/introduction-to-radiation-monitors/>>. Accessed: Apr. 2016.
- Evaluated Nuclear Structure Data File (ENSDF), National Nuclear Data Center (NNDC), Brookhaven National Laboratory (BNL). Online database accessed via: <<http://www.nndc.bnl.gov/chart/>>.
- Ferraz, H.B.; Bertolucci, P.H.; Pereira, J.S.; Lima, J.G.; Andrade, L.A., 1988. Chronic exposure to the fungicide maneb may produce symptoms and signs of CNS manganese intoxication. *Neurology* 38, 550-553.
- Flynn, M.R.; Susi, P., 2009. Neurological risks associated with manganese exposure from welding operations--a literature review. *International journal of hygiene and environmental health* 212, 459-469.
- Fored, C.M.; Fryzek, J.P.; Brandt, L.; Nise, G.; Sjogren, B., et al., 2006. Parkinson's disease and other basal ganglia or movement disorders in a large nationwide cohort of Swedish welders. *Occupational and environmental medicine* 63, 135-140.
- Fowler, K.; McConathy, J.; Khanna, G.; Dehdashti, F.; Benzinger, T.L.S., et al., 2013. Simultaneous PET/MRI acquisition: Clinical potential in anatomically focused and whole-body examinations, *Applied Radiology*, pp. 9-14.
- Fryzek, J.P.; Hansen, J.; Cohen, S.; Bonde, J.P.; Llabias, M.T., et al., 2005. A cohort study of Parkinson's disease and other neurodegenerative disorders in Danish welders. *Journal of occupational and environmental medicine* 47, 466-472.
- Gale, E.M.; Mukherjee, S.; Liu, C.; Loving, G.S.; Caravan, P., 2014. Structure-redox-relaxivity relationships for redox responsive manganese-based magnetic resonance imaging probes. *Inorganic chemistry* 53, 10748-10761.
- Gambhir, S.S., 2010. General Principles of Molecular Imaging, in: Weissleder, R.R., B.D.; Rehemtulla, A.; Gambhir, S.S. (Ed.), *Molecular imaging*. People's Medical Publishing House-USA, Shelton, Connecticut, United States, pp. 1-9.
- Gibbons, R.A.; Dixon, S.N.; Hallis, K.; Russell, A.M.; Sansom, B.F., et al., 1976. Manganese metabolism in cows and goats. *Biochimica et biophysica acta* 444, 1-10.
- Gimi, B.; Leoni, L.; Oberholzer, J.; Braun, M.; Avila, J., et al., 2006. Functional MR microimaging of pancreatic beta-cell activation. *Cell Transplant* 15, 195-203.
- Gonzalez-Cuyar, L.F.; Nelson, G.; Criswell, S.R.; Ho, P.; Lonzanida, J.A., et al., 2014. Quantitative neuropathology associated with chronic manganese exposure in South African mine workers. *Neurotoxicology* 45, 260-266.

- Greenwood, N.N.; Earnshaw, A., 1997. *Chemistry of the Elements*, 2nd ed. Butterworth-Heinemann, Oxford, United Kingdom.
- Guilarte, T.R., 2010. Manganese and Parkinson's disease: a critical review and new findings. *Environmental health perspectives* 118, 1071-1080.
- Harris, R.C.; Lundin, J.I.; Criswell, S.R.; Hobson, A.; Swisher, L.M., et al., 2011. Effects of parkinsonism on health status in welding exposed workers. *Parkinsonism & related disorders* 17, 672-676.
- Hevesy, G., 1923. The Absorption and Translocation of Lead by Plants: A Contribution to the Application of the Method of Radioactive Indicators in the Investigation of the Change of Substance in Plants. *The Biochemical journal* 17, 439-445.
- Hiraishi, K.; Narabayashi, I.; Fujita, O.; Yamamoto, K.; Sagami, A., et al., 1995. Blueberry juice: preliminary evaluation as an oral contrast agent in gastrointestinal MR imaging. *Radiology* 194, 119-123.
- Hudnell, H.K., 1999. Effects from environmental Mn exposures: a review of the evidence from non-occupational exposure studies. *Neurotoxicology* 20, 379-397.
- Israeli, R.; Sculsky, M.; Tiberin, P., Acute central nervous system changes due to intoxication by Manzidan (a combined dithiocarbamate of maneb and zineb), pp. 238-243.
- Israeli, R.; Sculsky, M.; Tiberin, P., 1983. Acute intoxication due to exposure to maneb and zineb. A case with behavioral and central nervous system changes. *Scandinavian journal of work, environment & health* 9, 47-51.
- Janus, N.; Launay-Vacher, V.; Karie, S.; Clement, O.; Ledneva, E., et al., 2010. Prevalence of nephrogenic systemic fibrosis in renal insufficiency patients: results of the FINEST study. *European journal of radiology* 73, 357-359.
- Josephs, K.A.; Ahlskog, J.E.; Klos, K.J.; Kumar, N.; Fealey, R.D., et al., 2005. Neurologic manifestations in welders with pallidal MRI T1 hyperintensity. *Neurology* 64, 2033-2039.
- Kahakachchi, C.L.; Moore, D.A., 2010. Identification and characterization of gadolinium(iii) complexes in biological tissue extracts. *Metallomics : integrated biometal science* 2, 490-497.
- Kenangil, G.; Ertan, S.; Sayilir, I.; Ozekmekci, S., 2006. Progressive motor syndrome in a welder with pallidal T1 hyperintensity on MRI: A two-year follow-up. *Movement disorders : official journal of the Movement Disorder Society* 21, 2197-2200.
- Klein, A.T.J.; Rosch, F.; Coenen, H.H.; Qaim, S.M., 2005. Labelling of manganese-based magnetic resonance imaging (MRI) contrast agents with the positron emitter ^{51}Mn , as exemplified by manganese-tetraphenylporphin-sulfonate (MnTPPS4). *Appl. Radiat. Isot.* 62, 711-720.
- Komura, J.; Sakamoto, M., 1992. Disposition, behavior, and toxicity of methylcyclopentadienyl manganese tricarbonyl in the mouse. *Archives of environmental contamination and toxicology* 23, 473-475.
- Komura, J.; Sakamoto, M., 1994. Chronic oral administration of methylcyclopentadienyl manganese tricarbonyl altered brain biogenic amines in the mouse: comparison with inorganic manganese. *Toxicology letters* 73, 65-73.
- Kondakis, X.G.; Makris, N.; Leotsinidis, M.; Prinou, M.; Papapetropoulos, T., 1989. Possible health effects of high manganese concentration in drinking water. *Archives of environmental health* 44, 175-178.

- Laohaudomchok, W.; Lin, X.; Herrick, R.F.; Fang, S.C.; Cavallari, J.M., et al., 2011. Neuropsychological effects of low-level manganese exposure in welders. *Neurotoxicology* 32, 171-179.
- Lau, S.J.; Sarkar, B., 1984. Comparative studies of manganese(II)-, nickel(II)-, zinc(II)-, copper(II)-, cadmium(II)-, and iron(III)-binding components in human cord and adult sera. *Canadian journal of biochemistry and cell biology* 62, 449-455.
- Lauffer, R.B., 1987. Paramagnetic Metal-Complexes as Water Proton Relaxation Agents for Nmr Imaging - Theory and Design. *Chem. Rev.* 87, 901-927.
- Ledneva, E.; Karie, S.; Launay-Vacher, V.; Janus, N.; Deray, G., 2009. Renal Safety of Gadolinium-based Contrast Media in Patients with Chronic Renal Insufficiency. *Radiology* 250, 618-628.
- Lobatto, M.E.; Fuster, V.; Fayad, Z.A.; Mulder, W.J., 2011. Perspectives and opportunities for nanomedicine in the management of atherosclerosis. *Nature reviews drug discovery* 10, 835-852.
- Loving, G.S.; Mukherjee, S.; Caravan, P., 2013. Redox-activated manganese-based MR contrast agent. *J Am Chem Soc* 135, 4620-4623.
- Mankoff, D.A., 2007. A definition of molecular imaging. *Journal of nuclear medicine* 48, 18N, 21N.
- Marsh, G.M.; Gula, M.J., 2006. Employment as a welder and Parkinson disease among heavy equipment manufacturing workers. *Journal of occupational and environmental medicine* 48, 1031-1046.
- Meco, G.; Bonifati, V.; Vanacore, N.; Fabrizio, E., 1994. Parkinsonism after chronic exposure to the fungicide maneb (manganese ethylene-bis-dithiocarbamate). *Scandinavian journal of work, environment & health* 20, 301-305.
- Mendonca-Dias, M.H.; Gaggelli, E.; Lauterbur, P.C., 1983. Paramagnetic contrast agents in nuclear magnetic resonance medical imaging. *Seminars in nuclear medicine* 13, 364-376.
- Mergler, D.; Huel, G.; Bowler, R.; Iregren, A.; Belanger, S., et al., 1994. Nervous system dysfunction among workers with long-term exposure to manganese. *Environmental research* 64, 151-180.
- Morato, G.S.; Lemos, T.; Takahashi, R.N., 1989. Acute exposure to maneb alters some behavioral functions in the mouse. *Neurotoxicology and teratology* 11, 421-425.
- Linus Pauling Institute (LPI), Oregon State University (OSU), updated: 2010. Manganese. <lpi.oregonstate.edu/mic/minerals/manganese>.
- Pan, D.; Caruthers, S.D.; Hu, G.; Senpan, A.; Scott, M.J., et al., 2008. Ligand-directed nanobialys as theranostic agent for drug delivery and manganese-based magnetic resonance imaging of vascular targets. *J Am Chem Soc* 130, 9186-9187.
- Pan, D.; Caruthers, S.D.; Senpan, A.; Schmieder, A.H.; Wickline, S.A., et al., 2010. Revisiting an old friend: manganese-based MRI contrast agents. *WIREs nanomedicine and nanobiotechnology* 3, 162-173.
- Pan, D.; Senpan, A.; Caruthers, S.D.; Williams, T.A.; Scott, M.J., et al., 2009. Sensitive and efficient detection of thrombus with fibrin-specific manganese nanocolloids. *Chemical communications* 22, 3234-3236.
- Peterson, T.E.; Furenlid, L.R., 2011. SPECT detectors: the Anger Camera and beyond. *Phys Med Biol* 56, R145-R182.

- Phelps, M.E.; Cherry, S.R.; Dahlbom, M., 2006. PET: Physics, Instrumentation, and Scanners. Springer, New York.
- Pierre, V.C.; Allen, M.J.; Caravan, P., 2014. Contrast agents for MRI: 30+ years and where are we going? *Journal of biological inorganic chemistry* 19, 127-131.
- Qazi, S.; Uchida, M.; Usselman, R.; Shearer, R.; Edwards, E., et al., 2014. Manganese(III) porphyrins complexed with P22 virus-like particles as T1-enhanced contrast agents for magnetic resonance imaging. *Journal of biological inorganic chemistry* 19, 237-246.
- Racette, B.A.; Aschner, M.; Guilarte, T.R.; Dydak, U.; Criswell, S.R., et al., 2012a. Pathophysiology of manganese-associated neurotoxicity. *Neurotoxicology* 33, 881-886.
- Racette, B.A.; Criswell, S.R.; Lundin, J.I.; Hobson, A.; Seixas, N., et al., 2012b. Increased risk of parkinsonism associated with welding exposure. *Neurotoxicology* 33, 1356-1361.
- Rocklage, S.M.; Cacheris, W.P.; Quay, S.C.; Hahn, F.E.; Raymond, K.N., 1989. Manganese(II) N,N'-Dipyridoxylethylenediamine-N,N'-Diacetate 5,5'-Bis(Phosphate) - Synthesis and Characterization of a Paramagnetic Chelate for Magnetic-Resonance Imaging Enhancement. *Inorganic chemistry* 28, 477-485.
- Rodier, J., 1955. Manganese poisoning in Moroccan miners. *British journal of industrial medicine* 12, 21-35.
- Rodriguez-Vargas, E.; Chen, J.W., 2010. Magnetic Resonance Imaging Agents. In: Weissleder, R.R., B.D.; Rehemtulla, A.; Gambhir, S.S. (Ed.), *Molecular imaging*. People's Medical Publishing House-USA, Shelton, Connecticut, United States, pp. 389-404.
- Roth, J.A., 2006. Homeostatic and toxic mechanisms regulating manganese uptake, retention, and elimination. *Biological research* 39, 45-57.
- Roth, J.A., 2009. Are there common biochemical and molecular mechanisms controlling manganese and parkinsonism. *Neuromolecular medicine* 11, 281-296.
- Royal Society of Chemistry, Radiochemical Methods Group. Alpha, Beta and Gamma Radioactivity. Essay, No. 3. United Kingdom.
- Ruben, S.; Hassid, W.Z.; Kamen, M.D., 1939. Radioactive Carbon in the Study of Photosynthesis. *J. Am. Chem. Soc.* 61, 661-663.
- Sanotsky, Y.; Lesyk, R.; Fedoryshyn, L.; Komnatska, I.; Matviyenko, Y., et al., 2007. Manganic encephalopathy due to "ephedrone" abuse. *Movement disorders* 22, 1337-1343.
- Scheuhammer, A.M.; Cherian, M.G., 1985. Binding of manganese in human and rat plasma. *Biochimica et biophysica acta* 840, 163-169.
- Searles Nielsen, S.; Checkoway, H.; Criswell, S.R.; Farin, F.M.; Stapleton, P.L., et al., 2015. Inducible nitric oxide synthase gene methylation and parkinsonism in manganese-exposed welders. *Parkinsonism & related disorders* 21, 355-360.
- Sigma-Aldrich Co., 2014. SAFETY DATA SHEET. Gadolinium(III) chloride hexahydrate. v. 5.2. Revised: 28 Jun. 2014. Document no.: G7532. p. 5.
- Sigma-Aldrich Co., 2015. SAFETY DATA SHEET. Manganese(ii) chloride tetrahydrate. v. 4.10. Revised: 26 Feb. 2015. Document no.: 203734. p. 5.

- Sikk, K.; Haldre, S.; Aquilonius, S.M.; Asser, A.; Paris, M., et al., 2013. Manganese-induced parkinsonism in methcathinone abusers: bio-markers of exposure and follow-up. *European journal of neurology* 20, 915-920.
- Sikk, K.; Haldre, S.; Aquilonius, S.M.; Taba, P., 2011. Manganese-Induced Parkinsonism due to Ephedrone Abuse. *Parkinson's disease* 2011, 865319, 8 pages.
- Sikk, K.; Taba, P.; Haldre, S.; Bergquist, J.; Nyholm, D., et al., 2010. Clinical, neuroimaging and neurophysiological features in addicts with manganese-ephedrone exposure. *Acta neurologica Scandinavica* 121, 237-243.
- Silva, A.C.; Bock, N.A., 2008. Manganese-enhanced MRI: an exceptional tool in translational neuroimaging. *Schizophrenia bulletin* 34, 595-604.
- Sjogren, B.; Gustavsson, P.; Hogstedt, C., 1990. Neuropsychiatric symptoms among welders exposed to neurotoxic metals. *British journal of industrial medicine* 47, 704-707.
- Sjogren, B.; Iregren, A.; Frech, W.; Hagman, M.; Johansson, L., et al., 1996. Effects on the nervous system among welders exposed to aluminium and manganese. *Occupational and environmental medicine* 53, 32-40.
- Smith, D.S.; Stabin, M.G., 2012. Exposure rate constants and lead shielding values for over 1,100 radionuclides. *Health Phys.* 102, 271-291.
- Sriram, K.; Lin, G.X.; Jefferson, A.M.; Roberts, J.R.; Wirth, O., et al., 2010. Mitochondrial dysfunction and loss of Parkinson's disease-linked proteins contribute to neurotoxicity of manganese-containing welding fumes. *FASEB J.* 24, 4989-5002.
- Thiruchelvam, M.; Brockel, B.J.; Richfield, E.K.; Baggs, R.B.; Cory-Slechta, D.A., 2000a. Potentiated and preferential effects of combined paraquat and maneb on nigrostriatal dopamine systems: environmental risk factors for Parkinson's disease? *Brain research* 873, 225-234.
- Thiruchelvam, M.; Richfield, E.K.; Baggs, R.B.; Tank, A.W.; Cory-Slechta, D.A., 2000b. The nigrostriatal dopaminergic system as a preferential target of repeated exposures to combined paraquat and maneb: implications for Parkinson's disease. *J. Neurosci.* 20, 9207-9214.
- Thomsen, H.S., 2009. Nephrogenic systemic fibrosis: history and epidemiology. *Radiologic clinics of North America* 47, 827-831, vi.
- Thomas Jefferson National Accelerator Facility (TJNAF) - Office of Science Education. "It's Elemental". Web Page. Accessed: 3 Jun. 2015. Series: It's Elemental.
- United States Department of Agriculture (USDA), Agricultural Research Service (ARS), 2009. USDA National Nutrient Database for Standard Reference. Release 22. Nutrient data laboratory home page: <<http://www.ars.usda.gov/ba/bhnrc/ndl>>.
- United States Environmental Protection Agency (EPA), 2009. National Primary Drinking Water Regulations. Report no.: EPA 816-F-09-004. p. 6.
- VanBrocklin, H.F., 2010. Radiochemistry of PET, in: Weissleder, R.R., B.D.; Rehemtulla, A.; Gambhir, S.S. (Ed.), *Molecular imaging*. People's Medical Publishing House-USA, Shelton, Connecticut, United States, pp. 304-326.
- van der Veldt, A.A.M.; Smit, E.F.; Lammertsma, A.A., 2013. Positron emission tomography as a method for measuring drug delivery to tumors in vivo: the example of [¹¹C]docetaxel. *Front. Oncol.* 3, Article 208.

- Wagner Jr., H.N., 2010. Foreword, in: Weissleder, R.R., B.D.; Rehemtulla, A.; Gambhir, S.S. (Ed.), *Molecular imaging*. People's Medical Publishing House-USA, Shelton, Connecticut, United States, pp. iii-v.
- Weinmann, H.J.; Brasch, R.C.; Press, W.R.; Wesbey, G.E., 1984. Characteristics of gadolinium-DTPA complex: a potential NMR contrast agent. *American journal of roentgenology* 142, 619-624.
- Werner, S.C.; Quimby, E.H.; Schmidt, C., 1949. The use of tracer doses of radioactive iodine, I131, in the study of normal and disordered thyroid function in man. *The Journal of Clinical Endocrinology & Metabolism* 9, 342-354.
- Williams, M.; Todd, G.D.; Roney, N.; Crawford, J.; Coles, C., et al., 2012. Toxicological Profile for Manganese, in: Public Health Service, United States Department of Health and Human Services.
- Williams-Johnson, M., 1999. Manganese and Its Compounds. World Health Organization, Geneva. Concise International Chemical Assessment, document no. 12.
- Wolf, G.L.; Burnett, K.R.; Goldstein, E.J.; Joseph, P.M., 1985. Contrast Agents for Magnetic Resonance Imaging. *Magnetic Resonance Annual*, 231-266.
- Yin, Z.; Jiang, H.; Lee, E.S.; Ni, M.; Erikson, K.M., et al., 2010. Ferroportin is a manganese-responsive protein that decreases manganese cytotoxicity and accumulation. *Journal of neurochemistry* 112, 1190-1198.
- Yokel, R.A., 2006. Blood-brain barrier flux of aluminum, manganese, iron and other metals suspected to contribute to metal-induced neurodegeneration. *Journal of Alzheimer's disease* 10, 223-253.
- Yokel, R.A., 2009. Manganese flux across the blood-brain barrier. *Neuromolecular medicine* 11, 297-310.
- Zhang, J.; Fitsanakis, V.A.; Gu, G.; Jing, D.; Ao, M., et al., 2003. Manganese ethylene-bis-dithiocarbamate and selective dopaminergic neurodegeneration in rat: a link through mitochondrial dysfunction. *Journal of neurochemistry* 84, 336-346.
- Zhang, Q.; Zhang, C.; Lu, Y.; Yang, K.; Ren, Q., 2013. Progress in the development of CdZnTe unipolar detectors for different anode geometries and data corrections. *Sensors* 13, 2447-2474.
- Zheng, W.; Kim, H.; Zhao, Q., 2000. Comparative toxicokinetics of manganese chloride and methylcyclopentadienyl manganese tricarbonyl (MMT) in Sprague-Dawley rats. *Toxicological sciences* 54, 295-301.
- Zhu, J.; Gale, E.M.; Atanasova, I.; Rietz, T.A.; Caravan, P., 2014. Hexameric Mn(II) dendrimer as MRI contrast agent. *Chemistry* 20, 14507-14513.

Chapter 2. Nuclear Cross-Sections and Chemical Separation of ^{52}Mn ^{1,2,3,4}

2.1. Background

Essential to any routine isotope production protocol is the ability to select target thickness, beam energy, beam current, and bombardment time based on predicted yield, which in turn is based on nuclear cross-section data. Nuclear cross-sections are a means of expressing the probability of a nuclear reaction channel occurring when matter is bombarded with ions, neutrons, etc. It is expressed as the effective cross-sectional area of the target nuclei, hence its name and dimensions of length squared. Cross-section is often expressed as cm^2 or barns,

¹ Much of this chapter was published previously:

Wooten, A.L.[†]; Lewis, B.C.[†]; Lapi, S.E., 2015. Cross-sections for (p,x) reactions on natural chromium for the production of $^{52,52m,54}\text{Mn}$ radioisotopes. *Appl. Radiat. Isot.* 96, 154-161.
([†]Contributed approximately equally to the work in this article.)

² A.L.W. contributed to: cross-section data analysis, advising Ben Lewis, cyclotron targetry and bombardment planning, chemical separations, preparation of figures and tables, and writing.

³ Acknowledgments: B.C. Lewis performed much of the laboratory work for the cross-section measurements, and he is a co-first author on the article in which the cross-section results were published (Wooten, et al., 2015). A.E. Wooten performed much or all of the work in the *SRIM/TRIM* software package. R.B. Gross, B.C. Lewis, and J. Unnerstall contributed to preliminary trials of separation chemistry. Kyle Brown (Dept. of Chemistry, WUSTL) performed cross-section simulations. The authors also acknowledge much helpful advice and instruction from T.E. Mastren and V.N. Richards (Lapi group); T.D. Whitehead (WUSM/MIR); R.T. Curry (University of Kansas, Department of Physics); and C.P. Grant (University of California-Davis, Department of Physics). We are also grateful to D.T. Trame, J.R. Kreidler, and D.G. Tapella (WUSM) for machine shop work; to A. Heidbreder (WUSM) for soldering; to Four Star Finishing in Saint Louis (esp. E.K. Sprung) for advice and electroplating of chromium; to W.H. Margenau, P.M. Margenau, and G.G. Gaehle (WUSM/MIR) for operation and maintenance of the CS-15 cyclotron; to W.H. Margenau for construction the sample ladder above the HPGe detector; and to L.D. Mullins, Jr. (Canberra) for performing the peak location (gamma-ray energy) calibration on the HPGe detector.

⁴ Project-specific funding: This work was funded in part by an internal award from WUSM/MIR.

although millibarns are more appropriate for many reaction channels that are induced by low-energy protons, such as those from the cyclotrons at our institution.

Target thickness and beam energy are typically selected so that the entry and exit energies of the beam will span a region of the excitation function with high cross-sections for the product and little or no cross-sections for other, competing reaction channels that may produce contaminant isotopes. Designing production runs to optimize this energy “window” can improve yield and radionuclidic purity of the final product. Thus, it is important to have accurate cross-section data for not only the reactions that produce the desired product, but also for the reactions that would produce contaminant isotopes. In this investigation, we bombarded chromium targets of natural isotopic abundance ($^{\text{nat}}\text{Cr} = ^{50}\text{Cr}$ (4.3%), ^{52}Cr (83.8%), ^{53}Cr (9.5%), ^{54}Cr (2.4%)), which could potentially produce several product isotopes. This work focused primarily on measurements for the production of ^{52}Mn , but also for $^{52\text{m}}\text{Mn}$ and ^{54}Mn as radiocontaminants. Only a few data sets are currently available with points at proton beam energy (E_p) ≤ 14 MeV for the $^{\text{nat}}\text{Cr}(p,x)$ reactions that produce $^{52,52\text{m}}\text{Mn}$ (Buchholz, et al., 2013; West Jr, et al., 1987; Barrandon, et al., 1975), and there are only data sets from enriched targets available for ^{54}Mn at these low energies (Levkovskij, 1991; Gusev, et al., 1990; Skakun, et al., 1986; Zyskind, et al., 1978; Kailas, et al., 1975; Johnson, et al., 1960). In this work, we contribute new experimental cross-section data for each of these (p,x) reactions that produce $^{52,52\text{m},54}\text{Mn}$ from bombardment of natural chromium with protons at low-energies.

The excitation peak for the $^{52}\text{Cr}(p,n)^{52}\text{Mn}$ reaction is in the 24 \rightarrow 6 MeV range of proton energies, meaning that production is optimized with ~ 24 MeV incident protons bombarding a target containing ^{52}Cr that is thick enough to degrade the proton energy all the way to ~ 6 MeV (threshold for the $^{52}\text{Cr}(p,n)^{52}\text{Mn}$ reaction: $E_p = 5.6$ MeV). This is also the optimal energy range

for producing the metastable isomer ^{52m}Mn , which has an excitation function $\sim 2\text{-}3\text{x}$ greater than the ground state. However, this short-lived radiocontaminant ($t_{1/2}=21.1$ min.) is practically eliminated by decay within hours, without contributing significantly to production of the ground state because ^{52m}Mn has a branching ratio of $<2\%$ for isomeric transition to ^{52}Mn .

2.2. Experimental

2.2.1. Materials

Copper sheet (0.762 mm thick, 99.9% purity) was purchased from ESPI Metals (Ashland, Oregon, United States), and copper foil (0.025 mm, 99.999% purity) was purchased from Alfa Aesar (Ward Hill, Massachusetts, United States). Natural abundance chromium was electroplated by Four Star Finishing (Saint Louis). The aluminum for the target holders were 6061-T6 aluminum alloy, pure aluminum (A.D. MACKAY, Denver North Carolina, United States), or pure niobium metal (A.D. MACKAY). All other solid and liquid chemicals were purchased from Sigma-Aldrich (Saint Louis, Missouri, United States), unless otherwise indicated. Nitrogen (N_2) gas was purchased from Cee Kay Supply (Saint Louis).

2.2.2. Target Preparation

Copper monitor foils were produced by punching ~ 9.5 mm discs from 0.762 mm (nominal) copper foil. However, Cr metal is very brittle, so cutting or punching discs from thin Cr foil was not feasible. Furthermore, thin Cr foil was not commercially available without a permanently attached Mylar (polyethylene terephthalate) backing.

Therefore, we developed a method for fabricating batches of thin Cr foils that would fit into target holders. Thin, circular foil discs were produced through a process of electrodeposition of non-enriched Cr onto small plugs of Cu backing material, followed by removal of the Cu backing, similar to a method used in the past (Tanaka and Furukawa, 1959). Holes (~10 mm diameter) were cut or punched from Cu sheet, and these holes were then filled using ~9.8 mm Cu discs that were punched from elsewhere on the Cu sheet. On the “back” side of the plate, these discs were fixed in place by soldering the back of each disc to one of several long strips of thick (~1-2 mm diameter) bus bar wire that was also soldered to the large copper plate. Figure 2.1 shows a sample that contained a 13x13 grid of copper plugs soldered in place on the back.

The back of the sample was masked with a lacquer, and the entire sample was submerged (while connected to the cathode) into an industrial-scale chrome plating bath, and the unmasked side of the sample was electroplated with Cr. This bath electroplated with “hard chrome,” meaning thick (tens to hundreds of μm), ultra hard deposits of pure Cr metal. (The more popular type of chrome plating, “decorative chrome”, is roughly 1,000x thinner and usually plated over nickel or copper.) The bath was an aqueous solution of 100:1 chromic acid (H_2CrO_4) and sulfuric acid (H_2SO_4). (Safety note: The chromic acid was made from chromium(VI) oxide (CrO_3 powder), which is acutely toxic (Sigma-Aldrich, 2014).) The sulfuric acid was a commonly used additive that contributed sulfate groups to the solution, which catalyzed the electroplating reaction (Mandich and Snyder, 2010). To produce individual Cr discs, the bus bar wire was clipped on either side of each copper plug in the assembly, producing individual copper plugs plated on one side with chromium. These plugs were placed in ~3-8 M nitric acid in a large glass container. The nitric acid digested the copper while leaving the chromium intact, and the acid

solution was changed several times during this process. The final result was circular discs of thin (and very brittle) Cr metal foils with a diameter of 9.8 mm.

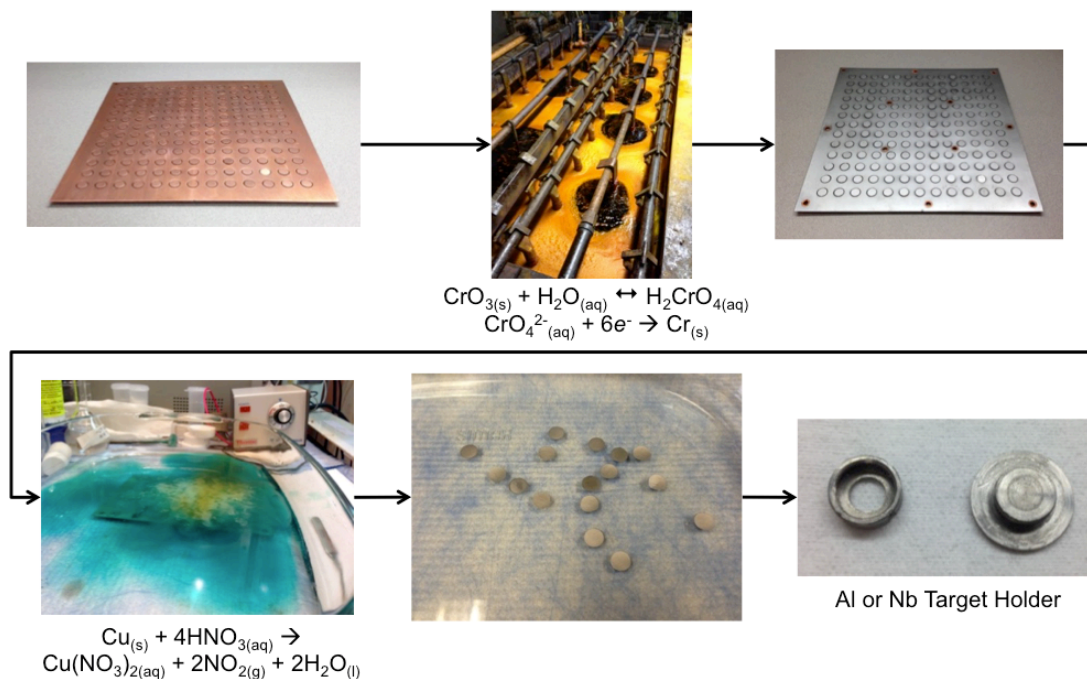


Figure 2.1. Photographs illustrating the process for the fabrication of thin Cr foil discs.

These images are representative images and not from the same production. (A similar figure was published in Wooten, et al., 2015 (supplementary information). Image courtesy of Elsevier. Used with permission.)

Before each stack of foils was assembled, the thickness of each Cr and Cu foil was calculated based on its diameter and mass, assuming cylindrical geometry. Based on instrumental uncertainty from the measurements of diameter and mass, the uncertainty in the calculated thickness of each Cu or Cr foil was <1.1%. Across all the Cr foil discs in all configurations and bombardments the diameter was 9.8 mm for all discs, with an average thickness of 82 μm ($\pm 10.5\%$), and the Cu foil discs had a diameter of 9.5 mm and an average thickness of 18.6 μm ($\pm 2.6\%$).

Cr foils were tested for elemental purity by a sixty-element screening performed by Galbraith Laboratories (Knoxville, Tennessee, United States). The foil was dissolved in acid and analyzed by inductively coupled plasma mass spectrometry (ICP-MS). The only contaminants >100 ppm (within uncertainty) were Sn (1195 ppm) and Se (134 ppm). This was a semi-quantitative screening with relative error of up to 50% for all measurements.

A custom target holder was designed and machined out of 6061-T6 aluminum alloy (95.8-98.6% aluminum) to hold the stacks of foils during cyclotron bombardment. Our design consisted of a base containing a dish with smooth vertical walls to hold the stack of foils yet allow for quick, easy removal of the foils from the dish after bombardment. The base had a blind hole on the non-vacuum side for improved contact with the circulating cooling water. The target holder also included a screw-on cap to hold the stack of foils in the holder when the foils were held vertically in the target station—perpendicular to the incident beam. This cap was threaded to match corresponding threads on the base, and the cap had a circular “window” to expose the foils directly to the beam.

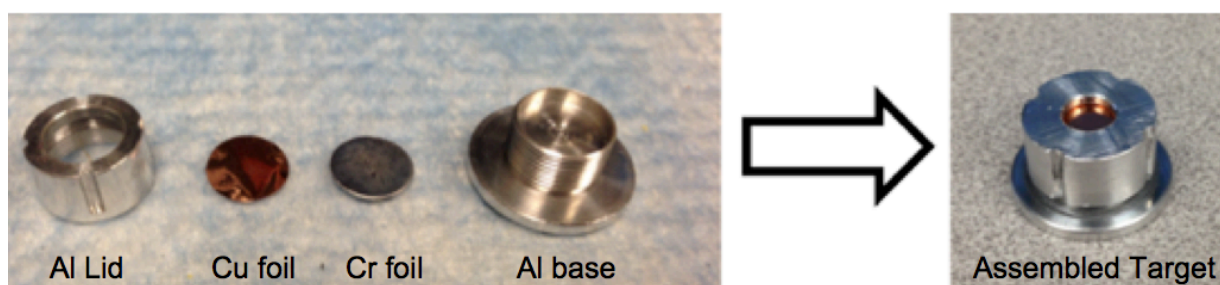


Figure 2.2. Photograph of one style of target holder used in this dissertation.

(The photographs on the left and right sides of the arrow are representative images, since they are not pictures of the exact same components or even the exact same designs.)

Four different stacked foil configurations consisting of Cu and Cr foils were used in this work to measure cross-sections in the Cr foils. The Cu foils were included for determination of

flux (Section 2.2.4.5) and entry energy (Section 2.2.4.4) of the proton beam based on monitor reactions in the Cu. Each configuration was bombarded in three separate targets, for a total of 12 bombarded targets in this work. The energy of the proton beam at the middle of every chromium foil was predicted using *The Stopping Range of Ions in Matter (SRIM)* software (Ziegler, et al., 2010), which implements the perturbative Bethe formula (with Bloch correction) for the stopping power (i.e., energy loss) of charged particles due to interactions with orbital electrons in a material.

2.2.3. Cyclotron Bombardment

Each target assembly was bombarded with low-energy ($E_p < 15$ MeV) protons from the CS-15 cyclotron (The Cyclotron Corporation, Berkeley, California, United States) at the Mallinckrodt Institute of Radiology (MIR) at Washington University School of Medicine (WUSM). During bombardment, the back of the target holder was cooled by circulating chilled water ($T \approx 2-5$ °C), and the front of the target was cooled by a He gas jet. Bombardments used in this work were typically 1-3 μ A for a duration of bombardment (t_b) that varied between 105 and 135 sec, (120 ± 15 sec). This uncertainty was accounted for (Section 2.2.4.8) in our determination of beam energy, beam current, cross-sections, and saturation yields.

2.2.4. Cross-Section Measurement

2.2.4.1. Gamma-Ray Spectroscopy

Proton bombardment of the stacked foil targets produced radioisotopes in each Cu and Cr foil, and these product isotopes were identified and quantified by gamma-ray spectroscopy from

a high-purity germanium (HPGe) detector (model: GC2018; relative efficiency: 24.5%) that was connected to a digital spectrum analyzer (DSA; model: DSA-1000) and operated by the *Gamma Acquisition & Analysis* module of the *Genie 2000* spectroscopy software package (v. 3.3). All three components were from Canberra (Meriden, Connecticut, United States). The principal isotopes measured were $^{63,65}\text{Zn}$ in the Cu foils and $^{52,52\text{m},54}\text{Mn}$ in the Cr foils, and their production and decay characteristics are summarized in Table 2.1.

A few hours after each bombardment, the stacked foil target was carefully disassembled. For each gamma-ray counting experiment, one foil was placed in a small weigh boat that was then placed on a 3 mm thick plastic shelf positioned at one of several distances directly above the open end of the HPGe crystal. Various positions were utilized so that samples could be counted at different distances from the detector to ensure a detector dead time (t_d) that was $\leq 5\%$ of detector real time (t_r). Each Cu and Cr foil was counted for at least 10 min. of detector live time (t_l). Additionally, all of the Cu foils were counted again several months later for 10 h each to measure a greater number of counts from the long-lived product ^{65}Zn ($t_{1/2}=244$ days) for better statistics.

Table 2.1. Summary of the radioisotope products in irradiated Cu and Cr foils.

Primary Target [†] (Natural Abundance)	Product (Half-Life)	Gamma-Rays [‡] (Branching Ratio)	Daughter (Half-Life)
<i>Cu foil:</i>			
⁶³ Cu (69.2%)	⁶³ Zn (38.5 min.)	670 keV (8.2%)	⁶³ Cu (stable)
⁶⁵ Cu (30.9%)	⁶⁵ Zn (244 d)	962 keV (6.5%) 1116 keV (50.0%)	⁶⁵ Cu (stable)
<i>Cr foil:</i>			
⁵² Cr (83.8%)	⁵² Mn (5.6 d)	1434 keV (100%) 936 keV (94.5%) 744 keV (90.0%) 1334 keV (5.1%) 1246 keV (4.2%)	⁵² Cr (stable)
⁵² Cr (83.8%)	^{52m} Mn (21.1 m)	848 keV (3.3%) 1434 keV (98.3%) 378 keV (1.7%)	⁵² Cr (stable) ^{52m} Mn (5.6 d)
⁵⁴ Cr (2.4%)	⁵⁴ Mn (312 d)	835 keV (99.98%)	⁵⁴ Cr (stable)

[†]All of the product isotopes in this table are produced primarily by (*p,n*) reactions from proton bombardment of $E_p < 15$ MeV. [‡]In our analysis, we only considered gamma-rays that were emitted by only one isotope/isomer, so the 1434 keV gamma-rays emitted by both ⁵²Mn and ^{52m}Mn was excluded from analysis. (Nuclear data accessed via: BNL/NNDC/ENSDF.)

The HPGe detector was calibrated for photopeak energy and detector efficiency. The energy calibration was performed using a mixed-gamma source in a sealed microcentrifuge tube (Eckert & Ziegler Analytics, Atlanta, Georgia, United States). We also performed our own detector efficiency calibrations using a mixed-gamma “point source” (Eckert & Ziegler Analytics). The detector efficiency (ϵ_c) was calculated for each gamma-ray energy (E_γ), and $\ln \epsilon_c$ was plotted versus $\ln E_\gamma$. This plot was linear between 166-1836 keV, so the data in this range were fit to the equation:

$$\ln \epsilon_c = m \cdot \ln E_\gamma + b , \quad (2.1)$$

where m and b are the slope and intercept of the linear fit. All gamma-rays measured in this investigation were within this range and are listed in Table 2.1. Equation 2.1 was solved for ϵ_c and fitted by floating for m and b using the *gnuplot* software (v. 4.6.6) (Williams, 1986), which implemented a non-linear least squares algorithm (Levenberg-Marquardt algorithm) (Crawford, 2014). The resulting fits served as calibration curves for calculating detector efficiencies for gamma-rays emitted by radionuclide products in the irradiated Cu or Cr foils. This calibration was performed for each geometry counting of irradiated Cu or Cr foils.

The fitting method weighted the fit parameters based on y-direction uncertainty in the data points. This uncertainty represented the uncertainty of the gamma emission rates for each gamma-ray from the calibration source (taken from the reference sheet), as well as the uncertainty in the counting of these emissions (Section 2.2.4.8). To improve the goodness-of-fit value, we would sometimes increase the level of statistical error to 1.5 or 2 standard deviations. This improved the fitting, and the additional uncertainty was accounted for in the uncertainty of the fitted parameters and propagated accordingly.

Additionally, to test for self-shielding in our Cr foils, we performed a calibration with the point source positioned directly above the same type of Cr foil used in our stacked foil experiments. The resulting efficiency calibration curve had a slope and y-intercept that were both within 0.5% of the values in the efficiency curve that we used for foils that were counted from the same geometry, thus illustrating that there was no significant attenuation of gamma rays by the foils themselves.

2.2.4.2. Data Analysis

We concur with Gagnon, et al. (2011a) that transparent, detailed explanation of analysis in cross-section experiments can reduce confusion in comparing and categorizing these studies. Here, we explain in detail the analysis that was used to transform counts from gamma spectroscopy into activity, then beam energy, then beam current, and finally into cross-section results for $^{52,52m,54}\text{Mn}$. We also describe our uncertainty analysis. Unless otherwise stated, all analysis work was performed in *Excel for Mac 2011* (v. 14.4.4) (Microsoft, Redmond, Washington, United States) or *Excel 2002* (v. 10) (Microsoft) for *Windows* (Microsoft).

2.2.4.3. Calculating Radioactivities of Radionuclide Products

The principle raw data for this investigation came from gamma spectroscopy, specifically the net peak area or number of counts (N_c) in each full-absorption photopeak of interest. For each such peak, the activity of the corresponding radioisotope at the beginning of counting (A_c) was proportional to the number of counts according to the following equation (Canberra, 2009):

$$A_c = \frac{N_c}{\epsilon_c I_\gamma C_d t_l}, \quad (2.2)$$

where I_γ is the branching ratio for the gamma-ray, and C_d is the following correction factor for decay during counting of the first member of a decay chain (Canberra, 2009; IEEE, 1999; Moore, 1973):

$$C_d = \frac{1 - e^{-\lambda t_r}}{\lambda t_r}, \quad (2.3)$$

where λ is the decay constant for the isotope ($\lambda=\ln(2)/t_{1/2}$). For isotopes with multiple characteristic gamma-rays, the activities (and uncertainties) calculated for the gamma-ray peaks were combined to a single value by an inverse-variance weighted average. Then, each activity was decay-corrected to the activity at EOB (A_{EOB}).

2.2.4.4. Calculating Energy of Proton Beam

The entry beam energy was calculated based on monitor reactions (Gagnon, et al., 2011a; Avila-Rodriguez, et al., 2008; Kim, et al., 2006; Takacs, et al., 1997; Blessing, et al., 1995; Scholten, et al., 1994; Kopecky, et al., 1993; Piel, et al., 1992; Tarkanyi, et al., 1991; Kopecký, 1985). In this work, we used the $^{nat}\text{Cu}(p,x)^{63,65}\text{Zn}$ monitor reactions with recommended cross-section data provided by the Nuclear Data Section of the International Atomic Energy Agency (IAEA/NDS). The activities were measured (Section 2.2.4.3) for ^{63}Zn and ^{65}Zn produced in a Cu monitor foil on top of the stack in n=5 different targets, and the ratio of the activities, A_{Zn-63} / A_{Zn-65} , was used to find the corresponding proton beam entry energy. This was determined by linear interpolation between two adjacent points of the activity ratio calculated using the IAEA-recommended cross-section data (increment=0.1 MeV) in the following equation (Gagnon, et al., 2011a; 2011b; Avila-Rodriguez, et al., 2009):

$$\frac{A_{Zn-63EOB}}{A_{Zn-65EOB}} = \frac{\sigma_{Zn-63}(1-e^{-\lambda_{Zn-63}t_b})}{\sigma_{Zn-65}(1-e^{-\lambda_{Zn-65}t_b})}, \quad (2.4)$$

where σ is the cross-section and $t_b=120\pm 15$ sec. Uncertainty was propagated through Equation 2.4 and through the linear interpolation.

After determining the proton beam energy in those foils, the inverse-variance mean of those energies was determined to be the beam energy at the midpoint of the Cu foil on top of the stack ($E_p=13.10\pm 0.04$ MeV) (Figure 2.3). The *Transport of Ion in Matter (TRIM)* module within the *SRIM* software package was used to perform Monte Carlo simulations of transmitted ions to determine that the entry energy was 13.285 ± 0.065 MeV, thus this was used as the entry energy for simulating the energy of the proton beam at the midpoint of all foils in all targets. Because of the spread in the thickness of our Cr foils, the beam energies for all foils in all configurations (excluding top Cu foils) were simulated using individual thicknesses that had been determined by mass (Section 2.2.2). We excluded from the data set any Cr foils where the beam energy was degraded >1.5 MeV from the midpoint of the previous foil to the midpoint of that Cr foil because of the thickness of the foils and the energy of the beam. The longitudinal straggling of the protons was estimated as the population standard deviation of the energies of $N\approx 1,000$ transmitted protons. We estimated that the uncertainty in the entry energy (± 0.04 MeV) was not correlated to the uncertainty in the beam energy in each foil in the stack, so we added this value (in quadrature) to the uncertainty due to longitudinal straggling in each *TRIM* simulation. We increased this uncertainty for the simulated beam energy at the midpoint of each foil by 1.1% to estimate the effect of the uncertainty in the measured thickness of each Cu and Cr foil (Section 2.2.2).

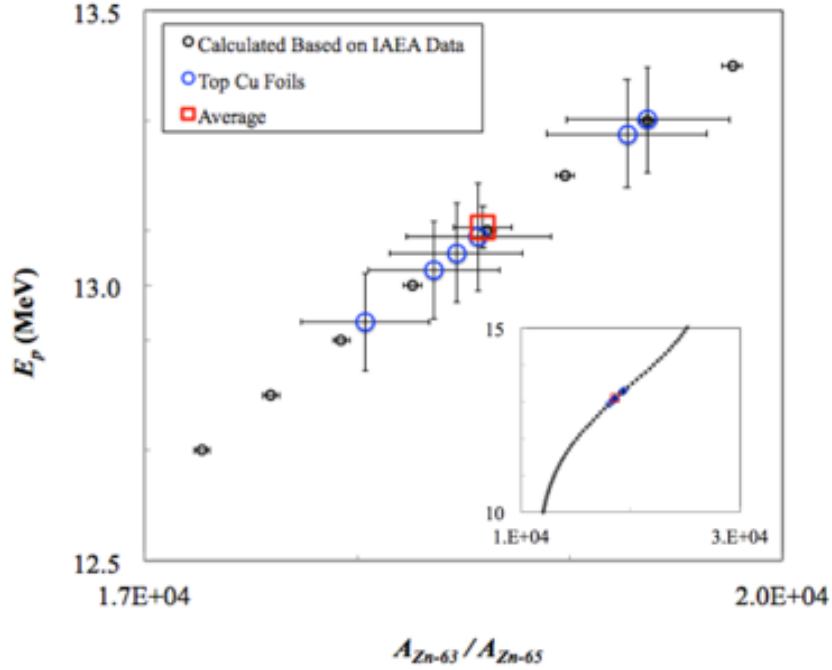


Figure 2.3. Plot showing the activity ratios calculated using $t_b=120$ sec and recommended cross-section data from the IAEA for the $^{nat}\text{Cu}(p,x)^{63,65}\text{Zn}$ monitor reactions.

A 6th-order polynomial fit to those results between 10-16 MeV proton energies; and beam energies for the copper foil on top of stacked targets in Configurations E and F that were calculated using this equation. Based on these results, the average beam energy at the midpoint of the top Cu foil was 13.10 ± 0.04 MeV. This translated to an entry beam energy of 13.285 ± 0.065 MeV, which was used for all calculations and simulations for all bombardments. Horizontal and vertical error bars for the experimental points are plotted but small. (IAEA data from: IAEA/NDS.) (Image: Wooten, et al., 2015. Image courtesy of Elsevier. Used with permission.)

2.2.4.5. Calculating Flux of Proton Beam

Similar to published methods (Lapi, et al., 2007; Kopecký, 1985; Greene and Lebowitz, 1972), the beam current was determined by production of ^{63}Zn in the Cu monitor foils. The standard activation equation was used to calculate current:

$$A_{EOB} = n\phi\sigma(1 - e^{-\lambda t_b}), \quad (2.5)$$

where A_{EOB} is the activity of a product at EOB; n is the number of target nuclei per area; and ϕ is the flux of beam particles passing through the target. The activity of ^{63}Zn produced from the

$^{nat}\text{Cu}(p,x)^{63}\text{Zn}$ reaction was calculated as described in Section 2.2.4.3. The number of target nuclei per area was calculated by the following equation:

$$n=N_A \left(\frac{\rho}{A_r} \right) h , \quad (2.6)$$

where N_A was Avogadro's constant; ρ was the density of Cu metal; A_r was the relative atomic mass of the non-enriched Cu metal; and h was the individual thickness of the Cu foil (determined by mass). To determine the cross-section for calculating beam current, we interpolated between adjacent cross-section points (interval: 0.1 MeV) from the IAEA-recommended excitation curve for the $^{nat}\text{Cu}(p,x)^{63}\text{Zn}$ reaction (IAEA/NDS). Uncertainty in the beam energy was propagated (Section 2.2.4.8) through the interpolation. Equation 2.5 was solved for ϕ , calculated based on the production of ^{63}Zn in the topmost Cu foil in each stacked foil target. The uncertainties in the values entered in these calculations were propagated to give the uncertainty in the beam current for that bombardment and eventually were propagated to the uncertainty of the proton energies in the final results.

2.2.4.6. Calculating Nuclear Cross-Section Results

Cross-sections were measured solving Equation 5 for σ . The following values were used: A_{EOB} calculated for $^{52,52m,54}\text{Mn}$ in each Cr foil (Section 2.2.4.3); n calculated using the mean thickness of our Cr foils; ϕ calculated for each bombardment; and $t_b=120\pm 15$ sec. We bombarded three targets for each configuration, and the same beam energy was assumed for every foil in the same position within a configuration, as calculated using the *TRIM* module. Cross-section results

from foils across different configurations were grouped into “bins” based on beam energy. For each bin, the energy and cross-section result (and uncertainties) were determined by inverse-variance weighted averages in the x- and y-directions and reported as our final results (Figure 2.4-Figure 2.6, Table 2.2-Table 2.4). As not all irradiated chromium foils were counted soon enough to detect ^{52m}Mn , our calculation neglects its contribution to production of ^{52}Mn .

2.2.4.7. Calculation of Predicted Yields at Saturation

Cross-section results were used to calculate the saturation activity yield. The activation equation (Equation 2.5) was used to calculate yields at saturation from our cross-section data, with a proton flux of 1 μA . Table 2.5 shows the predicted saturation yields that we calculated for each isotope product using our measured cross-section data.

2.2.4.8. Uncertainty Analysis

Error was propagated from the origin to final results as absolute uncertainty, not as percentages. Uncertainties $<0.05\%$ were neglected. Instrumental uncertainty was considered for every measurement, and random uncertainty was calculated for every repeated measurement and for counting of a random process (i.e., gamma spectroscopy). Our statistics are presented in a descriptive (not inferential) manner and thus we present the mean, standard deviation, and sample size for all of our final cross-section results (Table 2.2-Table 2.4).

Instrumental uncertainty was typically either provided by the instrument, or otherwise estimated to be ± 0.5 times the most precise digit of the measurement from that instrument. All random uncertainties were calculated as \pm one standard deviation for a sample, population, or Poisson distribution, and this standard deviation was propagated onward. For the foil counting,

we estimated that the uncertainty in the net peak area to be one standard deviation of the Poisson distribution (i.e., the square root of the number of counts in each peak). Whenever an average was calculated, the error was expressed as either a sample standard deviation (for sample size, N , <20) or a population standard deviation was calculated (e.g., for Monte Carlo results for $\sim 1,000$ transmitted ions from simulations in *TRIM*). Whenever a weighted average was appropriate, the inverse-variance weighted mean, \bar{x}_w , was calculated by the equation:

$$\bar{x}_w = \frac{\sum_i x_i / s_i^2}{\sum_i 1 / s_i^2}, \quad (2.7)$$

where x_i is a measurement and s_i is the uncertainty in that value. This type of weighting minimizes the uncertainty in the mean, which was:

$$s^2(\bar{x}_w) = \frac{1}{\sum_i 1 / s_i^2}. \quad (2.8)$$

Uncertainties were propagated by applying the following equation (Arras, 1998; Croarkin, 2003) for the propagation of relatively small uncertainties through any calculation that used input values that had uncertainty:

$$s^2(f) = \sum_i \left(\frac{\partial f}{\partial X_i} \right)^2 s_i^2 + \sum \sum_{i \neq j} \left(\frac{\partial f}{\partial X_i} \right) \left(\frac{\partial f}{\partial X_j} \right) s_{ij}, \quad (2.9)$$

where $s(f)$ is the error in the calculated value f ; X_i is each variable used to calculate f ; s_i is the standard deviation in X_i ; and s_{ij} is the covariance for variables i and j (for $i \neq j$). Our only

correlated sources of error were the fitted parameters for our efficiency calibrations, so the second term of Equation 2.9. This equation was zero for all other propagations of error. The partial derivative(s) in Equation 2.9 account for the relative influences of the uncertainty of each quantity on the uncertainty of the calculated quantity. All uncorrelated uncertainties for the same value, such as rounding error, instrumental error, and statistical error, were added in quadrature to give the total uncertainty for that quantity.

2.2.5. Chemical Separation

2.2.5.1. Chemical Isolation by Cation-Exchange Chromatography

Following a method published by Buchholz, et al. (2013), we used cation-exchange chromatography to separate ^{52}Mn from the chromium metal target after proton bombardment. The irradiated chromium metal was dissolved in approximately 0.5-1 mL hydrochloric acid that was diluted to a final concentrations of approximately 0.6-6.1 M. The solution was then repeatedly evaporated and resuspended in sulfuric acid to replace the chloride anions with sulfate, then diluted to form ~ 0.1 M sulfuric acid. Under these conditions, the solution was transferred to a pre-conditioned column of AG 50W-X8 cation-exchange resin (Bio-Rad, Hercules, California, United States). Much of the chromium(III) passed through the column and was further eluted in 0.1 M sulfuric acid, while $^{52}\text{Mn(II)}$ was immobilized on the column. Frequently, a visible band of Cr(III) was also immobilized on the column. Manganese-52(II), along with this band of Cr(III), was eluted in ammonium citrate (which was used by Buchholz, et al.), as well as aqueous solutions of ammonium oxalate, hydrochloric acid, or sodium(I) chloride.

Chloride (Cl⁻) anions were removed from the solutions of HCl and NaCl by evaporating the product solution to dryness using heat and, sometimes, simultaneous evaporation with nitrogen (N₂) gas. To remove the oxalate and citrate anions from their respective solutions, the solution was dried and elevated heat was used to decompose those molecules, leaving behind a dry residue containing metal solutes. This method had been validated previously by heating a visible mass of ammonium oxalate until all visible solid had disappeared. The remaining dried ⁵²Mn could be resuspended in another solvent, for example saline. Before animal injections, the pH of the solution containing ⁵²Mn was tested and, if necessary, raised to the range of pH~4-7 using dilute sodium hydroxide (NaOH).

2.2.5.2. Chemical Isolation by Anion-Exchange Chromatography

An alternative method for isolating ⁵²Mn from chromium metal was published recently by Graves, et al. (2015), which utilized anion-exchange chromatography. The key to this method was adding a large volume of ethanol to the digested target solution, presumably to complex with the Cr(III) cations (Severin, 2015), which would leave more chloride ions to complex with the Mn(II) cations. A method similar to the one described in the article was shared with us by the authors before publication, and we rapidly adapted it as our preferred separation method.

First, the bombarded target was digested in ≤0.5 mL of concentrated (12.1 M) hydrochloric acid with gentle heat. Next, 200 proof ethanol was added to make the resulting solution 96% ethanol and 4% concentrated HCl (both percentages by volume). The resulting solution was transferred to a pre-conditioned column of ~100-300 mg of AG 1-X8 strong anion-exchange resin. Under these conditions, most Cr(III) ions were eluted, while Mn(II) was

immobilized on the small resin column. After rinsing the column with additional 96%/4% ethanol/HCl, most of the $^{52}\text{Mn(II)}$ and Cr(III) that were on the column were eluted in dilute HCl.

Although the Cr(III) had decreased significantly from the original target solution, its presence in the eluted product meant that the above separation procedure needed to be repeated. Graves, et al. recommended performing the separation a total of three times. The eluted product was dried down with heat and sometimes N_2 gas and then redissolved in a small volume (~0.1-0.5 mL) of concentrated HCl. Next, 200 proof ethanol was added to make the resulting solution into 96%/4% ethanol/HCl. In later experiments we were able to “recondition” the same column by rinsing it with >10x column volume of each of the following solvents: 2 M HCl, 6 M HCl, 96%/4% ethanol/HCl, and water, always ending with the 96%/4% ethanol/HCl solution. The ^{52}Mn in ethanol/HCl was transferred to either a fresh, pre-conditioned column or the “reconditioned” original column, and the separation process was repeated at least two more times to further reduce Cr(III) content.

Chromium(III) content was determined at various check-points in the procedure using microwave plasma atomic emission spectroscopy (MP-AES). These samples were tested for Cr(III) by ICP-AES that had been calibrated using an atomic absorption spectroscopy (AAS) standard solution for Cr(III) in dilute HCl. Additional metal contaminants were assayed by ICP-AES following a similar procedure and using standard solutions for the corresponding metal cation, always in dilute HCl.

2.2.6. Characterization of Products

The recovery of the separation was assayed by measuring the radioactivity of the product using an ionization dose calibrator. The radionuclidic purity was tested using gamma-ray

spectroscopy by calculating the amount of any radionuclide other than ^{52}Mn and then expressing this amount as a percentage of the total radioactivity or total number of radioactive atoms detected by gamma-ray spectroscopy. Manganese-52m was removed by overnight decay, and ^{54}Mn was produced at a very low reaction rate because the $^{\text{nat}}\text{Cr}(p,x)^{54}\text{Mn}$ reaction had a cross-section that was $\sim 10\times$ lower than the $^{\text{nat}}\text{Cr}(p,x)^{52}\text{Mn}$ reaction, presumably due to the low natural abundance of ^{54}Cr (n.a.=2.4%) needed for the $^{54}\text{Cr}(p,n)^{54}\text{Mn}$ reaction.

Since many transition metals form bold colors in solution, visual observation with the unaided eye can be a good quick test for significant concentrations of the dissolved metal target in the separated product. Since Cr(III) is green in solution, we could quickly observe by eye the presence of Cr(III) above a certain threshold. Future work would include developing a protocol for determining effective specific activity (Section 5.2.5) by titration with a chelator, followed by radio-TLC. DOTA has been shown to be a suitable chelator for manganese (Graves, et al., 2015). For all of the methods mentioned above for characterizing chemical purity, it is worth noting that although $^{52,52\text{m},54}\text{Mn}$ all decay to stable daughter isotopes of chromium, and any other radiometal contaminants would decay to stable daughter isotopes of other transition metals, none of these stable daughters would be present in great enough concentrations to contribute significantly to chemical impurities.

2.3. Results

2.3.1. Nuclear Cross-Section Results

The stacked-foil experiments performed in this work produced cross-section data for the ${}^{\text{nat}}\text{Cr}(p,x){}^{52,52\text{m},54}\text{Mn}$ reactions for proton energies <14 MeV. We did not observe any other isotopes in the Cr foils from any other reactions or from the two other stable isotopes of Cr: ${}^{50}\text{Cr}$ (4.3% natural abundance) or ${}^{53}\text{Cr}$ (9.5% natural abundance). Our final cross-section results are plotted in Figure 2.4-Figure 2.6.

2.3.1.1. ${}^{\text{nat}}\text{Cr}(p,x){}^{52}\text{Mn}$

At low proton energies, ${}^{52}\text{Mn}$ was likely only produced by the ${}^{52}\text{Cr}(p,n){}^{52}\text{Mn}$ reaction (threshold: 5.600 MeV; ${}^{52}\text{Cr}$: 83.8% natural abundance) as the ${}^{53}\text{Cr}(p,2n){}^{52}\text{Mn}$ reaction (threshold: 13.688 MeV; ${}^{53}\text{Cr}$: 9.5% natural abundance) (BNL/NNDC/QCalc, 2014) has an energy threshold above the upper limit for our calculated entry beam energy. Therefore, results can be compared to published cross-sections for not only the ${}^{\text{nat}}\text{Cr}(p,x){}^{52}\text{Mn}$ reaction, but also the ${}^{52}\text{Cr}(p,n){}^{52}\text{Mn}$ reaction, after scaling down the published results from enriched targets based on natural abundance of ${}^{52}\text{Cr}$. Results for the ${}^{\text{nat}}\text{Cr}(p,x){}^{52}\text{Mn}$ reaction are shown in Figure 2.4. Our results are in agreement with published results for natural chromium targets (Buchholz, et al., 2013; West Jr, et al., 1987; Barrandon, et al., 1975), as well as re-scaled results from enriched targets (Levkovskij, 1991; Skakun, et al., 1986; Wing and Huizenga, 1962; Linder and James, 1959; Boehm, et al., 1952).

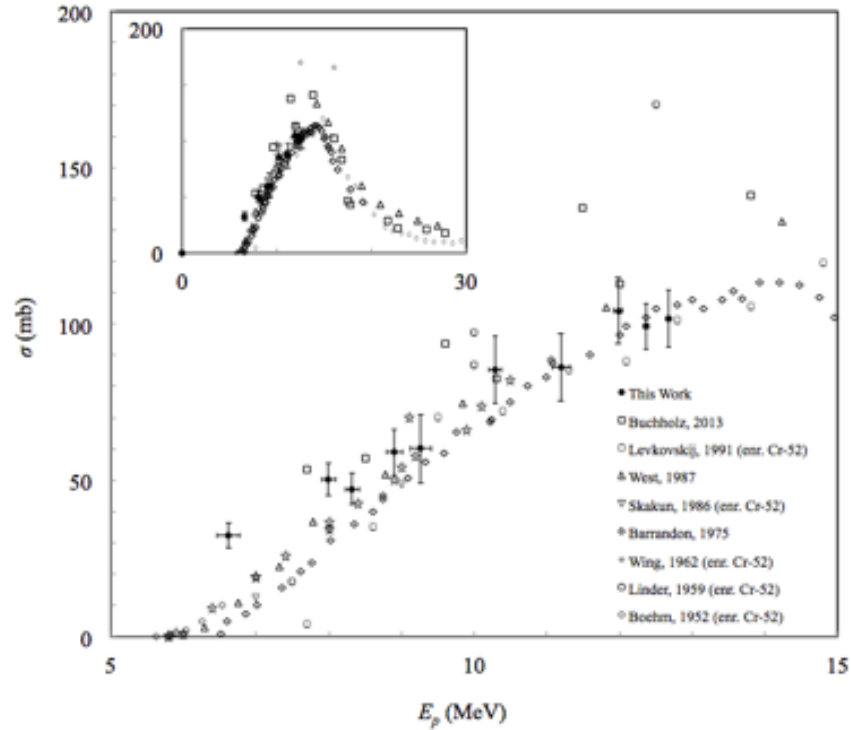


Figure 2.4: Cumulative cross-section results for the ${}^{\text{nat}}\text{Cr}(p,x){}^{52}\text{Mn}$ reaction. Other published data sets are also plotted, including rescaled results from enriched ${}^{52}\text{Cr}$ targets. (Image: Wooten, et al., 2015. Image courtesy of Elsevier. Used with permission.)

Table 2.2 Cross-section results for the ${}^{\text{nat}}\text{Cr}(p,x){}^{52}\text{Mn}$ reaction.

Energy E_p (MeV)	Cross-Section σ (b)
12.68 ± 0.04	0.102 ± 0.009
12.37 ± 0.04	0.099 ± 0.007
12.0 ± 0.1	0.104 ± 0.011
11.2 ± 0.1	0.086 ± 0.011
10.3 ± 0.1	0.085 ± 0.011
9.3 ± 0.1	0.060 ± 0.011
8.9 ± 0.1	0.059 ± 0.007
8.3 ± 0.1	0.047 ± 0.005
8.0 ± 0.1	0.050 ± 0.005
6.6 ± 0.2	0.032 ± 0.004

(Data: Wooten, et al., 2015. Data courtesy of Elsevier. Used with permission.)

2.3.1.2. $^{nat}\text{Cr}(p,x)^{52m}\text{Mn}$

^{52m}Mn has cross-sections roughly three times larger than ^{52}Mn in our energy range, and ^{52m}Mn can be produced by the $^{52}\text{Cr}(p,n)^{52m}\text{Mn}$ reaction (same threshold as the ground-state reaction) (BNL/NNDC/QCalc, 2014). Just as with the $^{nat}\text{Cr}(p,x)^{52}\text{Mn}$ results, there are no competing reactions that produce ^{52m}Mn from natural Cr in our proton energy regime. Therefore, our cross-section results can be compared to published results for both the $^{nat}\text{Cr}(p,n)^{52m}\text{Mn}$ reaction, as well as for the $^{52}\text{Cr}(p,n)^{52m}\text{Mn}$ reaction, after scaling down the published results from enriched targets based on natural abundance of ^{52}Cr . Our results for the $^{nat}\text{Cr}(p,x)^{52m}\text{Mn}$ reaction are shown in Figure 2. For this reaction product, only five values were reported because many Cr foils were not counted quickly enough to detect ^{52m}Mn before it decayed. The results from Barrandon, *et al.* (1975) are noticeably less than all other published results at $E_p > 10$ MeV. However, our results agree well with ^{52m}Mn cross-section data from other natural chromium target publications that were also cited for ^{52}Mn in Section 2.3.1 (Buchholz, et al., 2013; West Jr, et al., 1987; Barrandon, et al., 1975), as well as re-scaled results from enriched targets (Levkovskij, 1991; Skakun, et al., 1986; Wing and Huizenga, 1962; Linder and James, 1959; Boehm, et al., 1952). It appears that the excitation peak from Barrandon, *et al.* (1975) is not as high as all of these other published cross-sections, and our results are closer to the other studies.

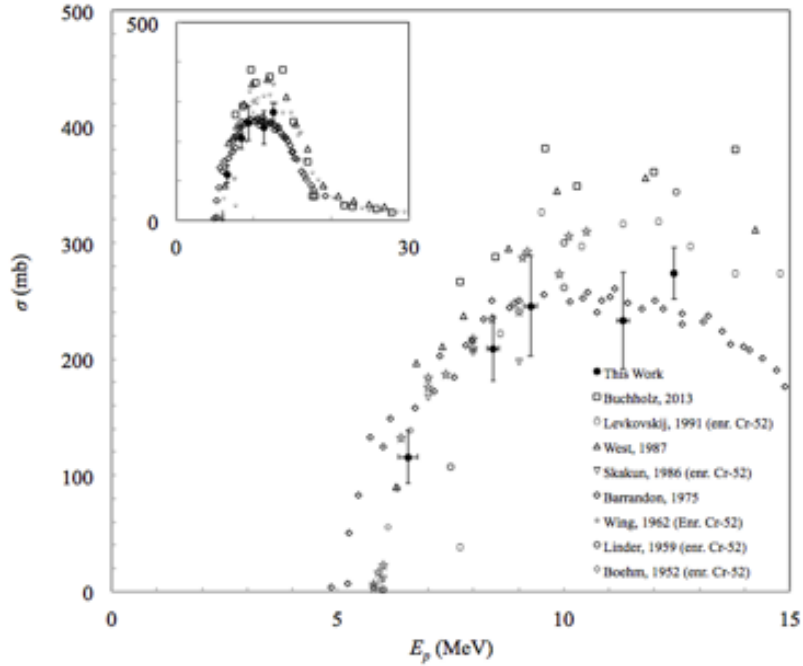


Figure 2.5. Cross-section results for the ${}^{\text{nat}}\text{Cr}(p,x){}^{52\text{m}}\text{Mn}$ reaction. Other published data sets are also plotted, including rescaled results from enriched ${}^{52}\text{Cr}$ targets. (Image: Wooten, et al., 2015. Image courtesy of Elsevier. Used with permission.)

Table 2.3. Cross-section results for the ${}^{\text{nat}}\text{Cr}(p,x){}^{52\text{m}}\text{Mn}$ reaction.

Energy	Cross-Section
E_p	σ
MeV	b
12.45 ± 0.04	0.274 ± 0.022
11.3 ± 0.1	0.233 ± 0.042
9.3 ± 0.1	0.246 ± 0.043
8.4 ± 0.1	0.209 ± 0.028
6.6 ± 0.2	0.116 ± 0.023

(Data: Wooten, et al., 2015. Data courtesy of Elsevier. Used with permission.)

2.3.1.3. $^{nat}\text{Cr}(p,x)^{54}\text{Mn}$

^{54}Mn was detected in lower yields than $^{52,52m}\text{Mn}$. The only logical reaction channel that would have produced this isotope in natural Cr was the $^{54}\text{Cr}(p,n)^{54}\text{Mn}$ reaction (threshold: 2.200 MeV; ^{54}Cr : 2.4% natural abundance) (BNL/NNDC/QCalc, 2014). Results were also compared to cross-section results from enriched targets that were scaled down based on the natural abundance of ^{54}Cr . Our results for the $^{nat}\text{Cr}(p,x)^{54}\text{Mn}$ reaction are shown in Figure 2.6. Only one published data set was reported for the production of ^{54}Mn from natural chromium with $E_p \leq 30$ MeV, and this data set only included cross-sections for $E_p \sim 17\text{-}38$ MeV. Therefore, we compared our results with published cross-sections from enriched ^{54}Mn targets (Levkovskij, 1991; Gusev, et al., 1990; Skakun, et al., 1986; Zyskind, et al., 1978; Kailas, et al., 1975; Johnson, et al., 1960) by rescaling the published cross-sections according to the natural abundance of ^{54}Cr .

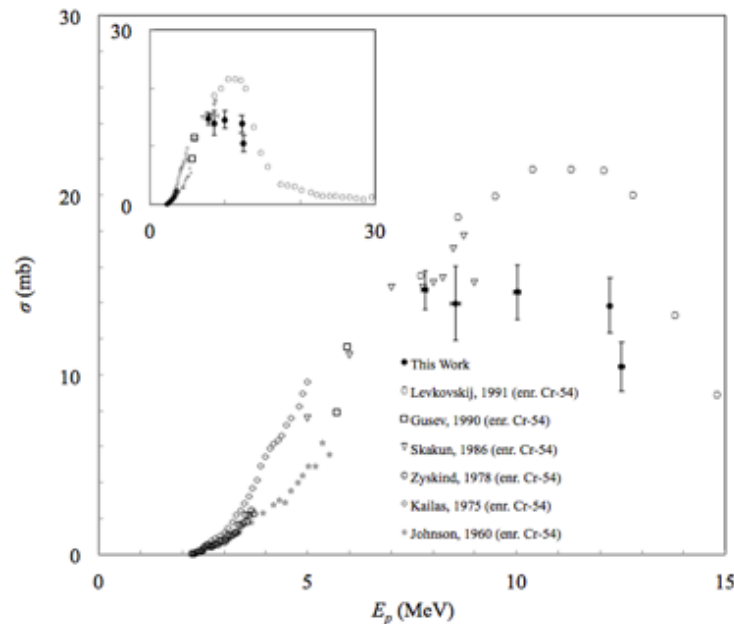


Figure 2.6. Cross-section results for the $^{nat}\text{Cr}(p,x)^{54}\text{Mn}$ reaction.

Other published data sets are also plotted, including rescaled results from enriched ^{54}Cr targets. (Image: Wooten, et al., 2015. Image courtesy of Elsevier. Used with permission.)

Table 2.4. Cross-section results for the $^{nat}\text{Cr}(p,x)^{54}\text{Mn}$ reaction.

Energy	Cross-Section
E_p	σ
MeV	b
12.5±0.1	0.0105±0.0014
12.24±0.05	0.0138±0.0015
10.0±0.1	0.0146±0.0015
8.5±0.1	0.014±0.002
7.8±0.1	0.0147±0.0011

(Data: Wooten, et al., 2015. Data courtesy of Elsevier. Used with permission.)

2.3.1.4. Predicted Saturation Yields

Table 2.5 shows the predicted saturation yields for $^{52,52m,54}\text{Mn}$ from $^{nat}\text{Cr}(p,x)$ reactions in the range of proton energies that was encompassed in our cross-section results for each isotope (Sections 2.3.1.1-2.3.1.3).

Table 2.5. Predicted yields for $^{nat}\text{Cr}(p,x)$ reactions at saturation.

Product	Energy Range	Predicted Yield at Saturation ^a	
	E_p	$Y_{predicted}$	
	MeV	mCi· μA^{-1}	GBq· μA^{-1}
^{52}Mn	12.7→6.6	27.1±1.0	1.00±0.04
^{52m}Mn	12.4→6.6	82.2±5.1	3.0±0.2
^{54}Mn	12.5→7.8	4.5±0.2	0.165±0.008

^aSaturation defined as bombardment time, $t_b=10t_{1/2}$. (Data: Wooten, et al., 2015. Data courtesy of Elsevier. Used with permission.)

2.3.2. Chemical Separation of ^{52}Mn

For the cation-exchange method, Figure 2.7 shows elution profiles for Cr(III), eluted in 0.1 M H_2SO_4 and measured by UV-Vis spectroscopy, plotted along with ^{52}Mn , eluted in various solutions and measured by radioactivity using a gas ionization dose calibrator. Not shown in

Figure 2.7 is the quantity of Cr(III) that was present in the eluted product, which was also visible often, especially when the volume of the product was concentrated. Preliminary separations using the anion-exchange isolation method demonstrated approximately equivalent durations for the procedure and resulted in lower recovery rates that were in the range of 40-70% (without decay correction).

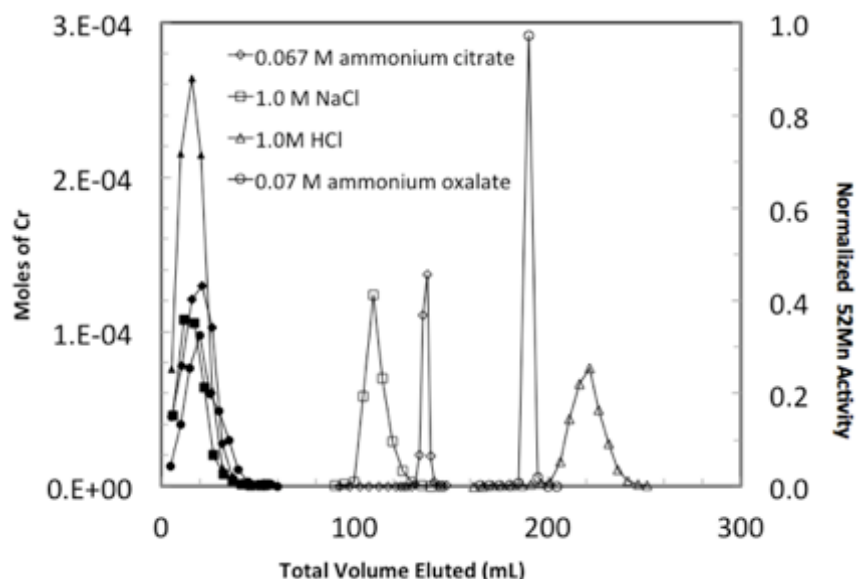


Figure 2.7. Elution profiles showing the elution of Cr(III) in 0.1 M H₂SO₄ and ⁵²Mn(II) in various eluents.

Cr(III) was measured by ultraviolet-visible spectroscopy, and ⁵²Mn(II) was measured by radioactivity using a gas ionization dose calibrator. Solid and hollow symbols with the same shape correspond to the same experiment. The gap between plots includes intermediate rinses with various solutions between eluting Cr(III) and ⁵²Mn(II). Not plotted: Cr(III) eluted after the initial elution of Cr(III), such as with the ⁵²Mn product or in any of the intermediate rinses.

2.4. Discussion

We have bombarded 2-3 stacked Cr foils with thickness of ~60-90 μm with ~13-14 MeV protons at 10-15 μA beam current. Typically, the top Cr foil contains enough activity for each subsequent experiment, but this incident beam energy only exploits approximately half of the

excitation peak for the $^{52}\text{Cr}(p,n)^{52}\text{Mn}$ reaction. At proton energies of 13-14 MeV greater activities are required for scaled-up production, an incident proton energy of ~ 24 MeV and a thicker Cr metal target could significantly increase bombardment yields for ^{52}Mn , while radiocontaminants could still be removed: ^{51}Cr ($t_{1/2}=27.7$ days) by chemical separation with the Cr target material, and ^{51}Mn ($t_{1/2}=46.2$ min.) by radioactive decay.

Reliable cross-section data that includes results from multiple groups is beneficial for confirming cross-section results, which in turn affect several parameters for accelerator-based isotope production that are essential to product yield and radionuclidic purity. However, few published studies currently exist for the reaction channels that produce ^{52g}Mn and other isotopes from bombardment of natural Cr with protons at energies <14 MeV, which is an important energy range for many biomedical cyclotrons worldwide. In this work, we have measured cross-sections for the $^{\text{nat}}\text{Cr}(p,x)^{52,52m,54}\text{Mn}$ reactions. Our results were in general agreement with published results from natural Cr targets and re-scaled results from isotopically enriched Cr targets. Cross-section results reported here will contribute to more accurate yield predictions and enhanced radionuclidic purity in the production of the isotopes studied here, particularly ^{52}Mn .

2.5. Conclusions and Recommendations

- Nuclear cross-sections have been measured for the $^{\text{nat}}\text{Cr}(p,x)^{52,52m,54}\text{Mn}$ reactions for incident protons with energy ≤ 13 MeV, which is easily achieved by most cyclotrons at medical centers. The cross-section results agreed closely with theoretical simulations, and they can be used to predict yields of $^{52,52m,54}\text{Mn}$ when bombarding natural chromium with low-energy protons.

- Chemical isolation was performed using a published method that involved digesting the chromium target in HCl, replacing the HCl with dilute H₂SO₄ and then immobilizing ⁵²Mn(II) on a cation-exchange column. This method resulted with visible amounts of Cr(III) in the product.
- Chemical isolation using a recently published method was more effective. This method involved digesting the chromium target in HCl, diluting this solution in ethanol, immobilizing ⁵²Mn(II) on an anion-exchange column, and performing this process repeatedly.
- *Recommended future directions:* Trace metal analysis after each round of the anion-exchange separation method to determine how many rounds are necessary; characterization of routine production including cyclotron yields, chemical recovery percentage, radionuclidic purity, and trace metals analysis.

2.6. References

- Arras, K.O., 1998. An Introduction To Error Propagation: Derivation, Meaning and Examples of Equation $C_y = F_x C_x F_x T$. Technical Report EPFL-ASL-TR-98-01 R3. Swiss Federal Institute of Technology Lausanne, Lausanne, Switzerland, p. 6.
- Avila-Rodriguez, M.A.; Rajander, J.; Lill, J.O.; Gagnon, K.; Schlesinger, J., et al., 2009. Proton energy determination using activated yttrium foils and ionization chambers for activity assay. Nucl. Instrum. Meth. Phys. Res. B 267, 1867-1872.
- Avila-Rodriguez, M.A.; Wilson, J.S.; Schueller, M.J.; McQuarrie, S.A., 2008. Measurement of the activation cross section for the (p,xn) reactions in niobium with potential applications as monitor reactions. Nucl. Instrum. Meth. Phys. Res. B 266, 3353-3358.
- Barrandon, J.N.; Debrun, J.L.; Kohn, A.; Spear, R.H., 1975. Study of Level of Ti, V, Cr, Fe, Ni, Cu and Zn by Activation with Protons Whose Energy Is Limited to 20 Mev. Nucl. Instr. Meth. 127, 269-278.
- Blessing, G.; Brautigam, W.; Boge, H.G.; Gad, N.; Scholten, B., et al., 1995. Internal Irradiation System for Excitation-Function Measurement Via the Stacked-Foil Technique. Appl. Radiat. Isot. 46, 955-960.

- Boehm, F.; Marmier, P.; Preiswerk, P., 1952. Relative cross sections for the excitation of isomers and ground states by (p,n) reaction. *Helvetica Physica Acta* 25, 599-604.
- Brookhaven National Laboratory (BNL)/National Nuclear Data Center (NNDC), 2014. Q-value Calculator (QCalc). Online: <<http://www.nndc.bnl.gov/qcalc/>>. Accessed: 2014. Mass values from: Wang, M.; et al., 2012. The AME2012 atomic mass evaluation (II). Tables, graphs and references. *Chinese Phys. C* 36, 1603-2014. Web programming: Pritychenko, B.; Sonzogni, A. Additional source of data: Atomic Mass Data Center (AMDC), International Atomic Energy Agency (IAEA).
- Buchholz, M.; Spahn, I.; Scholten, B.; Coenen, H.H., 2013. Cross-section measurements for the formation of manganese-52 and its isolation with a non-hazardous eluent. *Radiochim Acta* 101, 491-499.
- Canberra Industries Inc., 2009. Genie 2000 Spectroscopy Software: Customization Tools, V3.2, pp. 346-347.
- Crawford, D., 2014. User manual for gnuplot v. 4.6.6.
- Croarkin, C., Measurement Process Characterization, in: NIST/SEMATECH e-Handbook of Statistical Methods. Croarkin, C.; Tobias, P. (Eds.), Measurement Process Characterization, SEMATECH, State University of New York Polytechnic Institute (SUNY Poly)/National Institute of Standards and Technology (NIST). Online only: <<http://www.itl.nist.gov/div898/handbook/mpc/section5/mpc55.htm>>. Created: 1 Jun. 2003 (updated frequently since then).
- Evaluated Nuclear Structure Data File (ENSDF), National Nuclear Data Center (NNDC), Brookhaven National Laboratory (BNL). Online database accessed via: <<http://www.nndc.bnl.gov/chart/>>.
- Gagnon, K.; Benard, F.; Kovacs, M.; Ruth, T.J.; Schaffer, P., et al., 2011a. Cyclotron production of (99m)Tc: experimental measurement of the (100)Mo(p,x)(99)Mo, (99m)Tc and (99g)Tc excitation functions from 8 to 18 MeV. *Nucl. Med. Biol.* 38, 907-916.
- Gagnon, K.; Jensen, M.; Thisgaard, H.; Publicover, J.; Lapi, S., et al., 2011b. A new and simple calibration-independent method for measuring the beam energy of a cyclotron. *Appl. Radiat. Isot.* 69, 247-253.
- Graves, S.A.; Hernandez, R.; Fonslet, J.; England, C.G.; Valdovinos, H.F., et al., 2015. Novel Preparation Methods of Mn for ImmunoPET Imaging. *Bioconjugate Chem.* 26, 2118-2124.
- Greene, M.W.; Lebowitz, E., 1972. Proton reactions with copper for auxiliary cyclotron beam monitoring. *International Journal of Applied Radiation and Isotopes* 23, 342-344.
- Gusev, V.P.; Kolozhvary, A.A.; Smirnov, A.V.; Antropov, A.E., 1990. Total Cross Sections of 54-Cr(P,N) Reactions at Proton Energy 5.70 and 5.94 MeV, Conference on Nuclear Spectroscopy and Nuclear Structure, Leningrad, Soviet Union, 10-13 Apr. 1990. Report no.: INIS-SU--229. p. 262.
- International Atomic Energy Agency (IAEA)/Nuclear Data Section (NDS), 2014. "Monitor Reactions". Online: <https://www-nds.iaea.org/medical/monitor_reactions.html>.
- Johnson, C.H.; Galonsky, A.; Inskip, C.N., 1960. Cross Sections for (p,n) Reactions in Intermediate-Weight Nuclei, Oak Ridge National Lab. Reports. Oak Ridge National Laboratory, Oak Ridge, Tennessee, United States, p. 25.
- Kailas, S.; Gupta, S.K.; Mehta, M.K.; Kerekatte, S.S.; Namjoshi, L.V., et al., 1975. Total(P,N) Reaction Cross-Section Measurements on Ti-50, Cr-54, and Co-59. *Physical Review C* 12, 1789-1796.
- Kim, J.H.; Park, H.; Kim, S.; Lee, J.S.; Chun, K.S., 2006. Proton beam energy measurement with the stacked Cu foil technique for medical radioisotope production. *J Korean Phys Soc* 48, 755-758.

- Kopecký, P., 1985. Proton beam monitoring via the $\text{Cu}(p, x) \text{ } ^{58}\text{Co}$, $^{63}\text{Cu}(p, 2n) \text{ } ^{62}\text{Zn}$ and $^{65}\text{Cu}(p, n) \text{ } ^{65}\text{Zn}$ reactions in copper. *The International Journal of Applied Radiation and Isotopes* 36, 657-661.
- Kopecky, P.; Szelecsenyi, F.; Molnar, T.; Mikecz, P.; Tarkanyi, F., 1993. Excitation-Functions of (P, Xn) Reactions on (Nat)Ti - Monitoring of Bombarding Proton-Beams. *Appl. Radiat. Isot.* 44, 687-692.
- Levkovskij, V.N., 1991. Activation cross section nuclides of average masses ($A=40-100$) by protons and alpha-particles with average energies ($E=10-50$ MeV). Published in: Moscow.
- Linder, B.; James, R., 1959. Cross Sections for Nuclear Reactions Involving Nuclear Isomers. *Physical Review* 114, 322-325.
- Mandich, N.V.; Snyder, D.L., 2010. Electrodeposition of Chromium, in: Schlesinger, M.; Paunovic, M. (Eds.), *Modern Electroplating*. John Wiley & Sons, Inc., pp. 205-248.
- Moore, H., 1973. Correction for Change in Activity during Counting. *J. Radioanal. Chem.* 13, 165-168.
- Piel, H.; Qaim, S.M.; Stocklin, G., 1992. Excitation-Functions of (P,Xn)-Reactions on Ni-Nat and Highly Enriched Ni-62 - Possibility of Production of Medically Important Radioisotope Cu-62 at a Small Cyclotron. *Radiochim. Acta* 57, 1-5.
- Publicover, J.G.; Lapi, S.E.; Ruth, T.J., 2007. Method for calibrating particle beam energy. United States patent no.: US 2007/0040115 A1. Other patents: WO 2007016783 A1.
- Scholten, B.; Qaim, S.M.; Stocklin, G., 1994. Radiochemical Studies of Proton-Induced Be-7 Emission Reactions in the Energy-Range of 40 to 100 MeV. *Radiochim. Acta* 65, 81-86.
- Severin, G.W., 2015. Personal communication to: Wooten, A.L.
- Sigma-Aldrich Co., 2014. SAFETY DATA SHEET. Chromium(VI) oxide. v. 4.9. Revised: 28 Feb. 2015. Document no.: 236470. pp. 1,2,7,8.
- Skakun, E.A.; Batij, V.G.; Rakivnenko, J.N.; Rastrepin, O.A., 1986. Investigation of cross sections of $\text{Cr-52}(p,n)\text{Mn-52-m,g}$ and $\text{Cr-54}(p,n)\text{Mn-54}$ reactions in the energy range from 5 to 9 MeV, Conference on Nuclear Spectroscopy and Nuclear Structure, Kharkov, Soviet Union, p. 277.
- Takacs, S.; Sonck, M.; Scholten, B.; Hermanne, A.; Tarkanyi, F., 1997. Excitation functions of deuteron induced nuclear reactions on Ti-nat up to 20 MeV for monitoring deuteron beams. *Appl. Radiat. Isot.* 48, 657-665.
- Tanaka, S.; Furukawa, M., 1959. Excitation Functions for (p,n) Reactions with titanium, Vanadium, Chromium, Iron and Nickel up to $E_p=14$ MeV. *Journal of the Physical Society of Japan* 14, 1269-1275.
- Tarkanyi, F.; Szelecsenyi, F.; Kopecky, P., 1991. Excitation-Functions of Proton-Induced Nuclear-Reactions on Natural Nickel for Monitoring Beam Energy and Intensity. *Appl. Radiat. Isot.* 42, 513-517.
- The Institute of Electrical and Electronics Engineers Inc. (IEEE), 1999, American National Standard for Calibration and Use of Germanium Spectrometers for the Measurement of Gamma-Ray Emission Rates of Radionuclides. ANSI N42.14-1999, p. 17.
- West Jr, H.I.; Lanier, R.G.; Mustafa, M.G., 1987. $\text{Cr52}(p,n)\text{52Mng,m}$ and $\text{Cr52}(d,2n)\text{52Mng,m}$ excitation functions. *Physical Review C* 35, 2067-2076.
- Williams, T.K., C.; others, 1986. gnuplot software, v. 4.6.6.

- Wing, J.; Huizenga, J., 1962. (p,n) Cross Sections of V51, Cr52, Cu63, Cu65, Ag107, Ag109, Cd111, Cd114, and La139 from 5 to 10.5 MeV. *Physical Review* 128, 280-290.
- Wooten, A.L.; Lewis, B.C.; Lapi, S.E., 2015. Cross-sections for (p,x) reactions on natural chromium for the production of ^{52}Mn , ^{54}Mn radioisotopes. *Appl. Radiat. Isot.* 96, 154-161.
- Ziegler, J.F.; Ziegler, M.D.; Biersack, J.P., 2010. SRIM - The stopping and range of ions in matter (2010). *Nucl. Instrum. Methods Phys. Res. B* 268, 1818-1823.
- Zyskind, J.L.; Davidson, J.M.; Esat, M.T.; Shapiro, M.H.; Spear, R.H., 1978. A cusp in the $^{54}\text{Cr}(p, \gamma)^{55}\text{Mn}$ reaction. *Nucl. Phys. A* 301, 179-188.

Chapter 3. Biodistribution and PET Imaging of ^{52}Mn ^{1,2,3,4}

3.1. Background

Although imaging of accumulated Mn(II) is possible by T_1 -weighted MRI, truly quantitative measurement of the biodistribution of manganese *in vivo* is difficult. Direct, quantitative testing of manganese concentrations in humans is difficult because the exact ingested or inhaled dose is typically unknown. However, preclinical imaging and biodistribution studies using tracer amounts of radiomanganese provide a route to quantify the amount of manganese as a percentage of administered dose in animal models. Past studies have examined the biodistribution of manganese in various forms administered by different routes in rodents and fish, and have generally found that manganese is distributed to many tissues throughout the body. Several studies have shown the distribution of manganese using the radiotracers ^{52}Mn or ^{54}Mn , or utilizing stable manganese (^{55}Mn : 100% natural abundance) (Baum, et al., 2010) and a

¹ Much of the material in this chapter is in preparation for publication elsewhere:

A. Lake Wooten, Tolulope A. Aweda, Benjamin C. Lewis, Rebecca B. Gross, Suzanne E. Lapi.
Biodistribution and PET Imaging of Pharmacokinetics of Manganese in Mice using Manganese-52. In preparation.

² A.L.W. contributed to: cyclotron targetry, chemical separation, animal study design, biodistribution data analysis, image co-registration, preparation of figures and tables, and writing.

³ Acknowledgments: All *in vivo* imaging, dissection, and biodistribution counting were performed by the Small Animal Imaging Facility at WUSM/MIR. I acknowledge various contributions by the co-authors on the manuscript that is in preparation. Additionally, I acknowledge W.H. Margenau, P.M. Margenau, and G.G. Gaehele (WUSM/MIR) for operation and maintenance of the CS-15 cyclotron at WUSM/MIR.

⁴ Project-specific funding: This work was funded in part by an internal award from WUSM/MIR.

non-radioactive technique for quantifying metals. In this work, we utilized the isotope ^{52}Mn to study the biodistribution of injected and inhaled solutions of free manganese in mice and rats.

As discussed in Section 1.4, ^{52}Mn is a radiotracer with a half-life that is useful for biomedical studies and emits positrons with a high enough branching ratio to make it a realistic radionuclide for *in vivo* imaging by PET. Therefore, we also performed a PET imaging study in mice following I.V. administration of ^{52}Mn in aqueous solution. CT imaging of the same mice provided anatomical imaging, and *ex vivo* biodistribution after completion of all imaging confirmed quantification of the distribution of ^{52}Mn that was visualized in the PET images.

In the literature, free manganese has been shown to accumulate in the human pancreas following administration of a weakly bound manganese(II) chelate for manganese-enhanced MRI (MEMRI) (Botsikas, et al., 2012). Published *ex vivo* biodistribution results (Graves, et al., 2015) and our own results determined that the pancreas tends to accumulate and retain free manganese. Studying uptake of $^{52}\text{Mn(II)}$ by the pancreas is of interest for possible imaging applications related to diabetes, which showed significantly lower uptake of the MEMRI contrast agent in humans (Botsikas, et al., 2012). Since many diabetes studies use rats as animal models, and since rats have larger organs that can be better for imaging than in mice, we also studied the biodistribution of manganese in rats. Relatively long timepoints up to seven days post-injection were examined to allow time for manganese to decrease in tissues near the pancreas to increase contrast on PET imaging. After performing a biodistribution study in rats at these timepoints, PET/CT imaging studies were also performed.

This chapter presents experiments using animal models investigating the biodistribution for free ^{52}Mn that was administered in either saline or water. The biodistribution results and PET/CT images presented here are potentially useful as supporting information for

environmental and occupational regulations, for designing PET studies utilizing free ^{52}Mn , such as pancreas imaging in diabetes applications, and for predicting biodistribution of free manganese that might dissociate *in vivo* from a MEMRI contrast agent.

3.2. Experimental

3.2.1. Radionuclide Production

The radioactivity that was used in this chapter was produced and isolated using methods that are described in Section 2.2.5. In almost every production, the ^{52}Mn was eluted in HCl, the product was dried down, then resuspended in saline. If necessary, the pH of the resuspended saline product was adjusted with HCl and/or NaOH.

However, for the PET/CT imaging (and post-imaging *ex vivo* biodistribution) in mice, the ^{52}Mn was eluted in 0.067 M ammonium oxalate solution, and the ligand was removed in the following manner. The ammonium oxalate product was heated to dryness, and then the heat was increased to burn away the ammonium oxalate, leaving behind a residue containing ^{52}Mn in the vessel. The remaining ^{52}Mn was resuspended by adding water followed by a drop of 6 M hydrochloric acid, then heated to dryness. This evaporation and resuspension was repeated without any hydrochloric acid, then the ^{52}Mn was finally resuspended in water, resulting in a solution with pH of ~6.5, so pH adjustment was not performed because this pH was considered safe for intravenous injection in the mice.

3.2.2. Animal Models

All animal models used in this dissertation were purchased from Charles River Laboratories (Wilmington, Massachusetts, United States). Mice were allowed to eat and drink *ad libitum*, except for during handling, injection, and imaging until sacrifice. No mice in any group died during injection, inhalation or otherwise prior to their designated timepoint. All animal keeping and husbandry conformed to regulations of the Division of Comparative Medicine (DCM) at WUSM, and all experiments involving animal subjects were performed under a protocol that was approved by the Animal Studies Committee of WUSTL.

The biodistribution-only studies in mice that compared intravenous injection and aerosol inhalation were performed using male CD-1 mice. The PET/CT and post-imaging biodistribution study was performed using two male C57-Black-6 mice. All rat studies used male Sprague-Dawley rats.

3.2.3. Intravenous Injection of ^{52}Mn

Mice and rats were injected via tail vein with ~100 μL volume that contained: ~5-10 μCi for biodistribution-only studies and ~80-120 μCi for PET imaging studies of rats. For the mouse PET/CT, each animal was injected with 41 μCi of ^{52}Mn in 50 μL volume. The sample sizes for the studies included in this chapter were as follows: n=4 for biodistribution-only in mice, n=3 for biodistribution only in rats, and n=2 for PET/CT imaging in mice or rats.

The standard dose for administration was based on a single extra syringe of the dose that was weighed before and after expelling its contents to determine the mass of this liquid. The expelled contents were diluted to 100 mL volume, and then the radioactivity was measured in an

aliquot from this dilution. This result was used to calculate the concentration of activity of the original dose solution.

3.2.4. Inhalation of Aerosols Containing ^{52}Mn

The inhaled doses of ^{52}Mn salt solutions were administered to mice as previously reported by our group (Aweda, et al., 2013; Aweda, et al., 2015) using other radiolabeled compounds. Solutions were loaded into a Small Volumetric Mean Diameter (VMD) Nebulizer Unit (Aeroneb Lab, Aerogen, Dangan, Galway, Ireland) with the following specifications (Aerogen, 2004): $>0.1 \text{ mL}\cdot\text{min}^{-1}$ flow rate, $4.0\text{-}6.0 \mu\text{m}$ VMD, $<0.2 \text{ mL}$ residual volume. The exit port of the nebulizer was inserted into a chamber made from a clear plastic (Figure 3.1).

Four mice were inserted individually into four tubes with a plastic plunger to gently push their body to the front of the tube and their snout through a small opening at the opposite end of the tube. The ^{52}Mn solution was pipetted into the liquid reservoir of the nebulizer and then the nebulizer was powered on, producing an aerosol that filled the chamber. The mice were allowed to inhale the aerosol for $\sim 4\text{-}7 \text{ min.}$, then the tubes were detached, and the mice were removed from their tubes. One of the mice from each inhalation group of four mice was euthanized immediately to serve as the standard dose received for its cohort—before activity could be excreted from its body. The remaining three mice would be used for *ex vivo* biodistribution studies, so the biodistribution results for each timepoint after inhalation of ^{52}Mn represent $n=3$ mice.

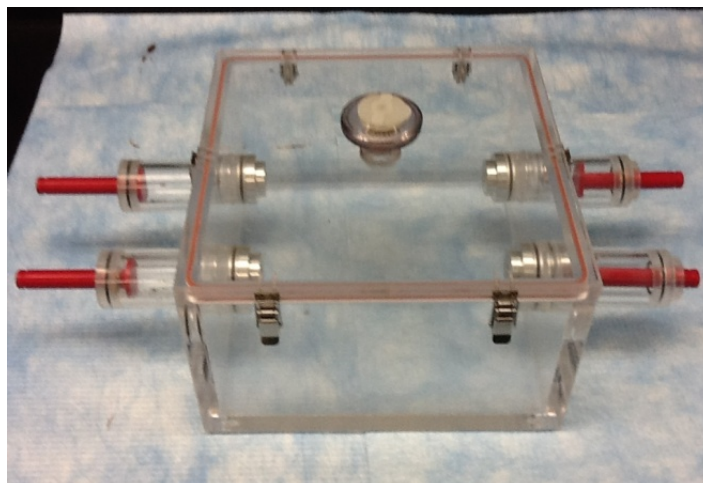


Figure 3.1. Plastic chamber for inhalation studies in mice.

Nebulizer shown inserted in the ceiling of the chamber, but not connected to its power supply. (Image: Aweda, et al., 2013 (supplementary information). Image courtesy of The Royal Society of Chemistry. Used with permission.)

3.2.5. Ex Vivo Biodistribution

At each timepoint post-administration, the mice or rats for that timepoint were euthanized, dissected, and each tissue was weighed and analyzed for radioactivity (Beckman Instruments, Irvine, California, United States) (De Silva, et al., 2012). The radioactivity in the diluted standard dose solution for the intravenous cohort (Section 3.2.3) and the carcass of the standard dose mouse from the inhalation cohort (Section 3.2.4) were each measured in the same manner. The percentage of injected or inhaled dose per gram of tissue (%ID/gram) was calculated. When comparing the results from these studies, we examined the magnitude of the uptake of ^{52}Mn in tissues as %ID/gram and as a function of time and mode of administration.

3.2.6. PET/CT Imaging

To reduce scanner time and because these mice were small enough, all imaging in the mouse study was performed simultaneously for both mice lying together side-by-side on a

specially made bed of each scanner. Rat imaging was performed individually. Shortly before each timepoint for PET imaging, anatomic images were obtained by non-contrast CT using an Inveon small animal PET/CT scanner (Siemens Preclinical Solutions, Knoxville, Tennessee, United States). CT imaging was repeated before each timepoint for PET imaging.

PET imaging was performed using either the Inveon PET/CT scanner or a microPET Focus 220 scanner (Siemens Preclinical Solutions). Static PET data were acquired for 30 minutes at the 1-hour timepoint and for 1 hour at the 3-day timepoint. Attenuation maps for each subject were obtained from either the CT scan in the Inveon scanner or by a transmission scan on the Focus 220 scanner. Images were analyzed using *Inveon Research Workplace* software (Siemens Preclinical Solutions).

3.3. Results

Figure 3.2 shows the results from *ex vivo* biodistribution of ^{52}Mn in saline administered via intravenous injection or by inhalation. Manganese-52 was cleared rapidly from the blood, as demonstrated by its rapid decrease from 1 to 24 hours p.i., and the activity in the gastrointestinal tract—stomach and intestines—also decreased rapidly between those same timepoints. At 1 hour p.i., the highest activity was found, in decreasing order, in the liver, kidney, lung, heart, pancreas, spleen, and salivary glands; however, by 24 hours p.i., the concentration of ^{52}Mn in all of these organs of high initial uptake had decreased greatly, except for the salivary glands, pancreas, and kidney. Among the tissues that had lower initial uptake at 1 hour p.i., ^{52}Mn was retained, to various degrees, in the brain, bone, and thyroid.

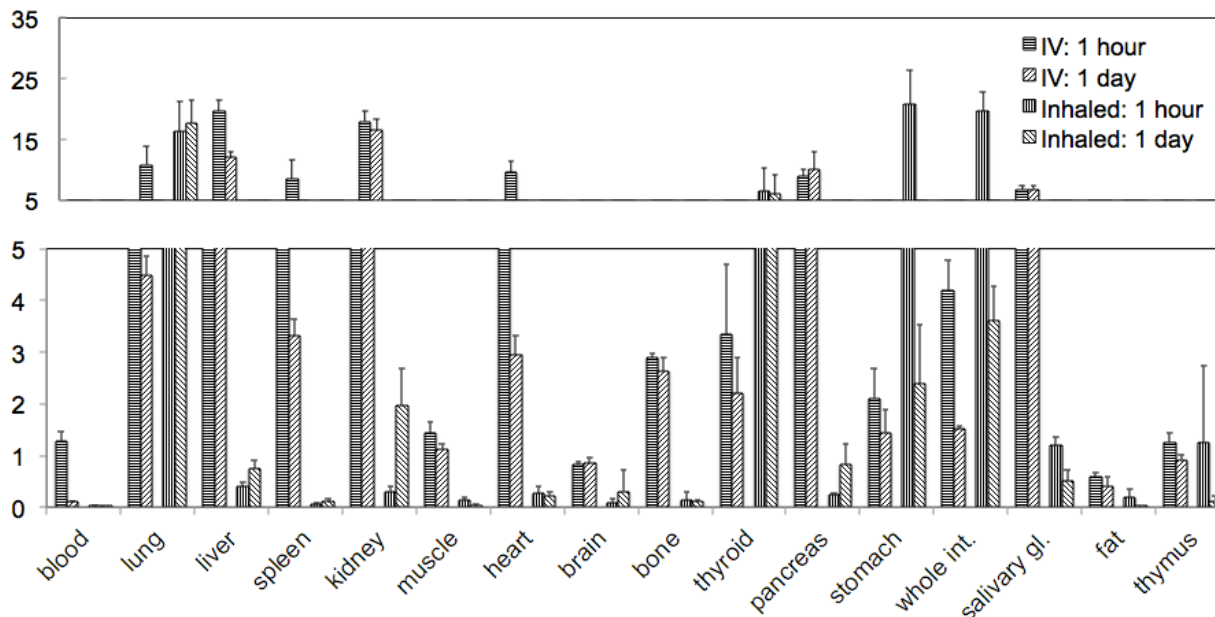


Figure 3.2. Plot showing results from ex vivo biodistribution of saline solutions containing ^{52}Mn administered via intravenous injection or inhalation.

The timepoints shown represent time after administration of the dose. Sample sizes for each timepoint were $n=4$ mice for injection and $n=3$ for inhalation. Error bars: negative error bars not shown for visual clarity; error bars represent statistical uncertainty across animals in each cohort and no propagated uncertainty from other sources of uncertainty.

The results from inhalation show high concentration of ^{52}Mn at 1 hour p.i., in decreasing order, stomach, intestines, lung, and thyroid. From the data at 24 hour p.i., ^{52}Mn was detected in the lungs and thyroid, but it was cleared from the stomach and intestines. Additionally, low activity of ^{52}Mn was observed in the blood, suggesting that manganese was cleared rapidly from the blood, just as in the results from IV injection. Figure 3.2 also shows that, from 1 to 24 hours p.i., ^{52}Mn accumulated in the kidney, pancreas, brain, liver, and spleen.

Figure 3.3 shows co-registered PET/CT images of the exact same two mice at 1 hour and 3 days following intravenous injection of ^{52}Mn in aqueous solution. The PET signal in this figure had been windowed for ease of visualizing signal from the abdomen. At 1 hour post-injection, ^{52}Mn is observed in the digestive tract, kidneys, and likely the pancreas, although the pancreas is

difficult to identify definitively. At 3 days post-injection, the ^{52}Mn left the digestive tract, while it is retained in the kidneys, as well as liver, pancreas, and thyroid gland. Figure 3.4 shows the results from the *ex vivo* biodistribution measurements that were performed after all PET and CT imaging were completed at 3 days post-injection.

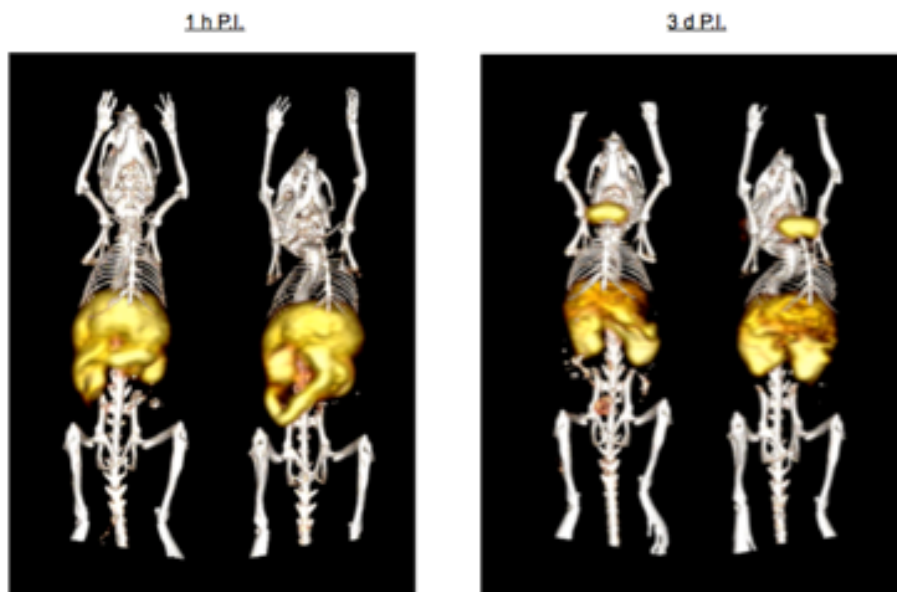


Figure 3.3. PET/CT images of mice at 1 h and 3 days following intravenous administration of ^{52}Mn in aqueous solution, windowed for visualizing activity in the abdomen.

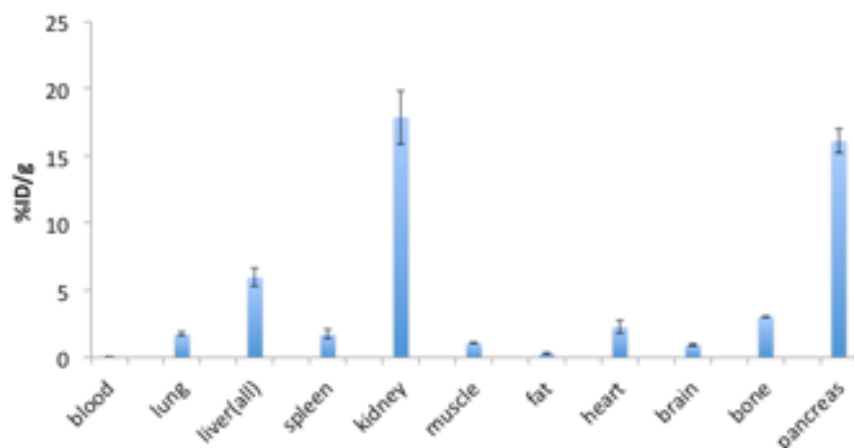


Figure 3.4. Results from *ex vivo* biodistribution performed shortly after imaging at 3 day timepoint.

The biodistribution results from CD-1 rats at 1 hour, 1 day, 3 days, and 7 days post injection of ^{52}Mn are shown in Figure 3.5.

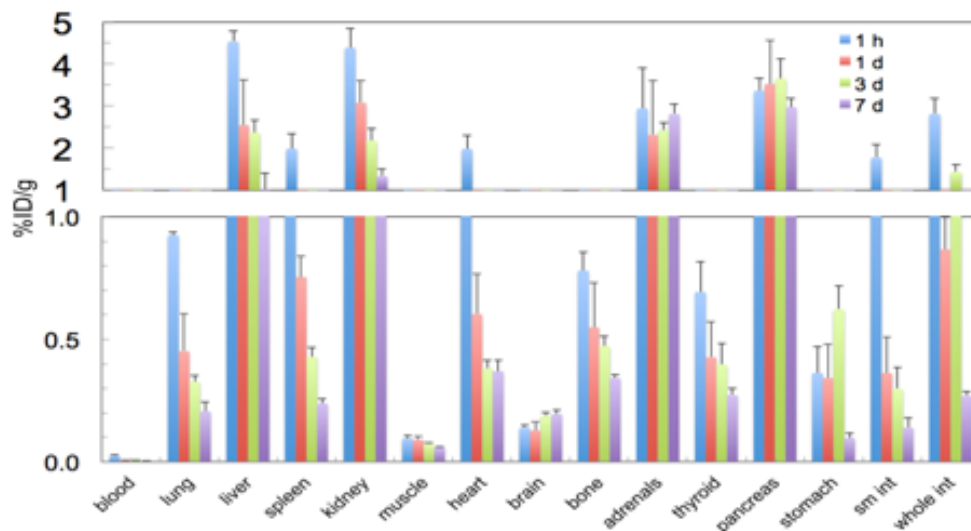


Figure 3.5. Biodistribution results of ^{52}Mn isolated by anion-exchange chromatography and administered in a saline solution by intravenous injection into male CD-1 rats.

The timepoints shown represent time from administration until sacrifice of rats. For each timepoint of intravenous injection, n=3.

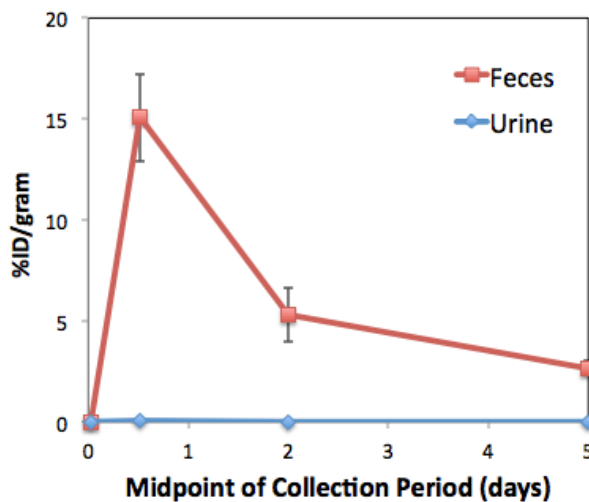


Figure 3.6. Excretion profile for male rats from the 7-day cohort that received intravenous administration of $[^{52}\text{Mn}]\text{MnCl}_2$.

Excretions were collected at 1 hour, 1, 3, and 7 days, so the timepoints plotted above are at the midpoint of each collection period. Error bars represent statistical uncertainty across animals in each cohort and no propagated uncertainty from other sources of uncertainty.

Figure 3.7 shows a typical co-registered PET/CT MIP image of a CD-1 rat at 7 days post-injection of ^{52}Mn , windowed for visualizing radioactivity in the abdomen, and Figure 3.8 shows the excretion profile and post-imaging biodistribution for the CD-1 rats (n=2) that were imaged by PET/CT.

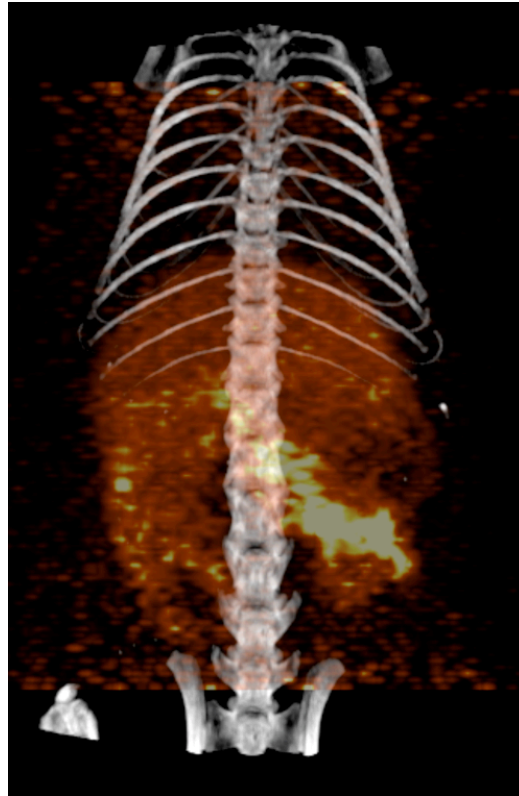


Figure 3.7. Approximately ventral view of a maximum intensity projection (MIP) image of PET signal co-registered with CT image of a male CD-1 rat at 7 days following intravenous administration of ^{52}Mn in saline.

CT was windowed for visualization of skeleton; PET signal was windowed for improved visualization of PET signal from the abdomen.

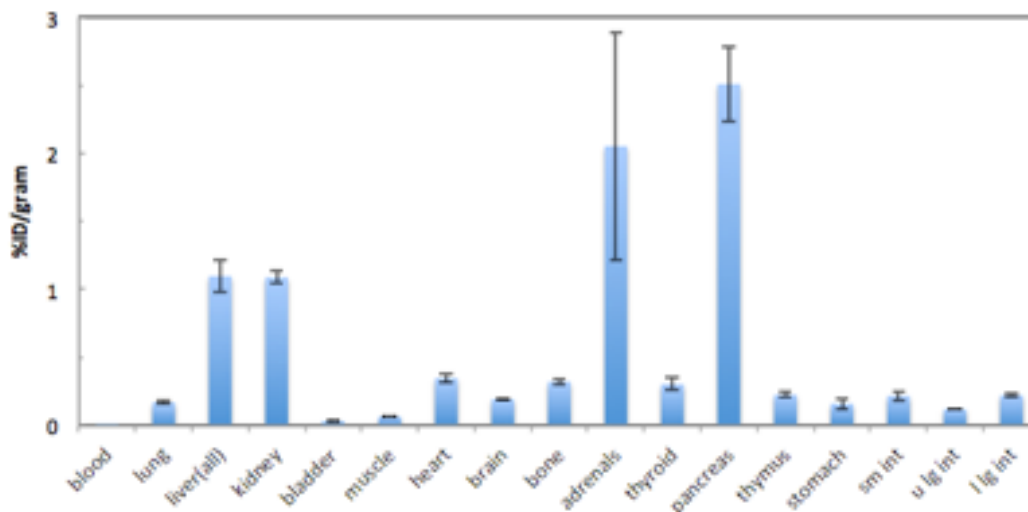


Figure 3.8. Post-imaging biodistribution results of ^{52}Mn in male CD-1 rats. Animals euthanized 7 days post-injection of ^{52}Mn (n=2).

3.4. Discussion

For the comparison of IV injection to inhalation of ^{52}Mn in mice, the concentration of ^{52}Mn in most tissues at both 1- and 24-hour timepoints is higher than in the inhalation results. The activity in the gastrointestinal tract was much greater in the inhalation results, suggesting that some of the dose may have been either swallowed directly from the aerosol or inhaled, cleared by mucociliary clearance, and then swallowed. Also in our studies, we observed uptake in the pancreas and brain, while ^{52}Mn that entered the stomach or intestines did not appear to be retained, although the one hour amounts were much higher in the inhalation groups likely due to putative swallowing of some of the dose. Retention of ^{52}Mn in the brain, thyroid, and thymus was observed in results from both injection and inhalation. We also found significant uptake of ^{52}Mn at 24 h in the bone (2.6%) resulting from injection, but not from inhalation.

For both injection and inhalation, ^{52}Mn was cleared rapidly from the blood, and the injection data showed ^{52}Mn in the liver and kidney in <1 hour. The inhalation data also suggest accumulation in the liver and kidneys, but this accumulation took much longer than one hour. Although manganese appears to accumulate in both liver and kidneys, results from the literature (Cikrt, 1972; Bertinchamps, et al., 1966; Papavasiliou, et al., 1966; Kato, 1963) suggest that very little manganese is excreted in urine. Instead, the vast majority of manganese is excreted in feces, primarily due to release of manganese from the liver into the enterohepatic circulation. In other studies, animals that were administered manganese or radiomanganese intravenously (Ni, et al., 1997; Chauncey, et al., 1977; Hughes, et al., 1966; Kato, 1963; Koshida, et al., 1963; Fore and Morton, 1952b), high uptake was generally observed in the kidney, pancreas, liver, adrenal glands, and intestine, as well as comparatively small amounts in the brain. Brain, et al. (2006) and Helig, et al. (2006) reported that, for intratracheal instillation, $^{54}\text{MnCl}_2$ was retained in the lungs to a large extent but was also found in significant concentrations in the intestines, liver, kidneys, and in a small concentration in the brain. These intratracheal instillation studies also showed that Mn can enter the bloodstream from the lungs, possibly by ion channels, but not by the divalent metal transporter-1 (DMT-1) in that particular tissue (Brain, et al., 2006; Heilig, et al., 2006). These general trends in manganese distribution agree with studies that focused more narrowly on the *in vitro* or *in vivo* uptake of manganese by cells or tissues that included liver (Kodama, et al., 1991; Cikrt, 1972), kidney (Kodama, et al., 1991), pancreas (Kodama, et al., 1991), intestines (Brain, et al., 2006; Leblondel and Allain, 1999), salivary glands (Seshadri and Hoy, 2010; Ni, et al., 1997), myocardium (Chauncey, et al., 1977), and bone (Fore and Morton, 1952a).

Owing to its neurotoxic effects, particular interest has been paid to uptake of manganese in the brain by various routes. Kanayama, *et al.* (2005) administered to mice by eight different routes a solution containing sixteen different radiotracers, mostly transition metals, and, for most administration routes, $^{54}\text{Mn}(\text{II})$ had higher brain uptake than most of the other tracers. In several other studies, rodents received radiomanganese by carotid injection or continuous *in situ* brain perfusion brain. These studies suggest that manganese enters the brain by more than one mechanism, including carrier-mediated uptake of Mn-citrate (Crossgrove, *et al.*, 2003), by store-operated calcium channels as Mn(II) (Crossgrove and Yokel, 2005), by transferrin-receptor mediated endocytosis as Mn-transferrin (Aschner and Gannon, 1994; Aschner and Aschner, 1990), or by other unspecified mechanism(s) that are faster than simple diffusion (Aschner and Gannon, 1994; Rabin, *et al.*, 1993). In a comparison of ^{54}Mn species administered by *in situ* brain perfusion, Mn-citrate was transported across the blood-brain barrier faster than either free Mn(II) or Mn-transferrin, suggesting that Mn-citrate might be an important route for manganese uptake in the brain (Crossgrove, *et al.*, 2003). Furthermore, it appears likely that manganese could accumulate in the brain because it appears to efflux at a rate that is consistent with simple diffusion (Yokel, *et al.*, 2003; Yokel, 2002).

Since it is known that certain inhaled substances can enter the brain directly from the olfactory bulb—without entering the bloodstream—there have been a considerable number of studies examining the possibility of manganese entering the brain by such mechanisms. Characterization of this mechanism(s) would be particularly relevant to the problem of inhaled manganese in metal workers. Animal studies using radiomanganese (Tjalve, *et al.*, 1996; Tjalve, *et al.*, 1995) or MEMRI (Pautler, *et al.*, 1998; Serrano, *et al.*, 2008), suggested that Mn(II) can be transported from the olfactory bulb and into olfactory neurons, transported through those

neurons, across synaptic junctions, into secondary olfactory neurons, and then into the diencephalon and cerebrum, and (in rats) into the spinal cord. Thompson *et al.* (2007) tested uptake in rats with defective divalent metal transporter-1 (DMT-1) proteins and confirmed that this transporter is involved in manganese uptake in the rat olfactory bulb based on higher uptake in healthy control rats. In rats, ninety minute nose-only inhalation of aerosolized [⁵⁴Mn]MnCl₂ (Brenneman, et al., 2000) or [⁵⁴Mn]MnHPO₄ (Dorman, et al., 2002) solution leads to uptake in the olfactory bulb and olfactory tubercle. In both studies, they observed uptake in lungs, liver, kidney, and pancreas, and—at much lower amounts—in the striatum of the brain. In a similar study, Lewis, *et al.* (2005) exposed mice and rats to nebulized, non-radioactive MnCl₂ for 10 nose-only doses of 6 hours each. Sample analysis by proton induced X-ray emission (PIXE) revealed elevated manganese in trigeminal ganglia, suggesting this nerve as a possible pathway for brain entry of manganese.

In our studies, relatively high uptake was observed in the lung and thyroid following either route of administration. Although several papers confirmed thyroid uptake of manganese from different administration routes in animal models (Nishida and Kawada, 1992; Kawada, et al., 1985; Deysach and Ray, 1949; Ray and Deysach, 1942), the biology of uptake of manganese in the thyroid does not seem clear (Nishida and Kawada, 1992). Interestingly, electron spin resonance (ESR) has shown that only a small fraction of the manganese naturally found in the rat thyroid is in the 2+ oxidation state (Sakurai, et al., 1985), perhaps suggesting that it is bound to serum protein(s) as Mn(III) and not present as a free Mn(II). Additionally, following subcutaneous injection of Mn(II)Cl₂ in guinea pigs (Deysach and Ray, 1949), manganese rapidly accumulated in thyroid by 24 hours p.i., but then 70% of the manganese in the thyroid at 24 hours had cleared by 48 hours p.i.; and then 85%, by 96 hours p.i. Inhaled manganese uptake in

salivary glands was in agreement with observations in welders exposed to manganese (Wang, et al., 2008). Interestingly, our results showed that injection of $^{52}\text{MnCl}_2$ exhibited higher and faster uptake in salivary gland than in the inhalation study. Our results demonstrate uptake of ^{52}Mn in the brain, thyroid, and pancreas in all trials. Interestingly, uptake from IV administration was higher in brain and pancreas, but lower in thyroid, compared to inhalation results. Also, IV administration resulted in very high activity in salivary glands. Manganese-52 might someday be used as a PET agent for niche clinical research applications, but our biodistribution results in mice can be used, in conjunction with other published results, to inform regulations for safe levels of environmental and occupational exposure to manganese.

Additionally, we have presented PET/CT images that visualize biodistribution of free $^{52}\text{Mn(II)}$ in mice, along with results from *ex vivo* biodistribution that was performed after imaging. The distribution of PET signal in the images from the final timepoint generally agrees with the biodistribution results. Building off the results presented, ongoing and future work could include: using a more effective method for separating ^{52}Mn from a chromium metal matrix; more complete characterization of the separated ^{52}Mn product, including radionuclidic purity, trace metals analysis, and/or effective specific activity titration; examining biodistribution at longer timepoints than 24 hours; contrast-enhanced CT that will reveal the pancreas on CT, making it possible to draw ROIs on the CT images for PET quantification; and possible applications in PET imaging of diseases that can alter the absolute magnitude or relative distribution of manganese *in vivo*.

One factor that motivated our interest in PET imaging of pancreas function with free cations of radiomanganese was a MEMRI study by Botsikas, et al. (2012). In that study, humans were imaged by T_1 -weighted MRI, and the signal in the pancreas of a normoglycemic (non-

diabetic) person increased dramatically (became brighter, as shown in Figure 3.9) after intravenous infusion of the manganese chelate mangafodipir trisodium (manganese dipyridoxal diphosphate (Mn-DPDP), *Teslascan*, GE Healthcare, Amersham, Buckinghamshire, United Kingdom; See Section 1.2.3). For patients with diabetes, signal also increased after infusion of mangafodipir, but by a significantly ($p=0.01$) smaller increase. Patients with advanced diabetes that required insulin treatment demonstrated even smaller average increase that was also significantly ($p=0.007$) less than the control group. Mangafodipir is a weakly bound chelate, and a significant portion of it dissociates *in vivo* (Gallez, et al., 1996; Harisinghani, et al., 2001), so it was likely that at least some of the enhanced signal observed by Botsikas, et al. was from free Mn(II) cations and not only from chelated Mn(II)-DPDP. This is not surprising because pancreas, like several other organs, naturally takes up manganese (Yokel, 2009). Uptake of manganese by healthy pancreas was further confirmed in our own *ex vivo* biodistribution studies in mice and rats, as well as in another similar study using radiomanganese (Graves, et al., 2015).

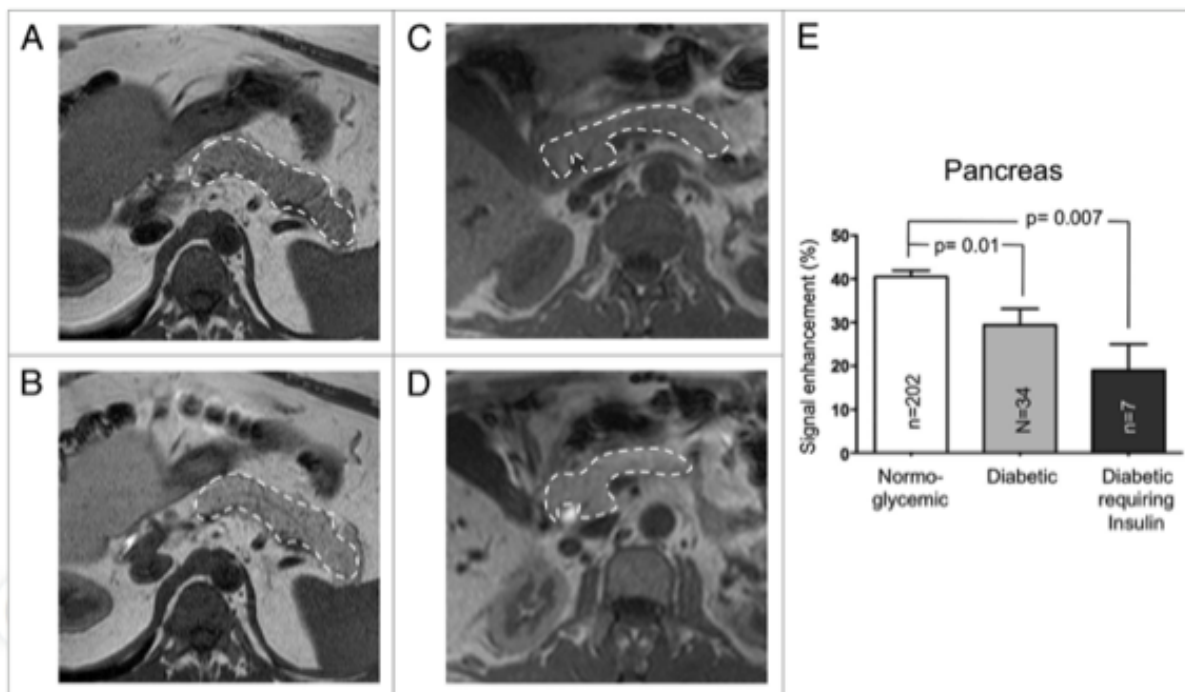


Figure 3.9. T_1 -weighted MRI images of a normoglycemic (non-diabetic) human and a human with type 2 diabetes.

Left column: normoglycemic patient; right column: patient with type-2 diabetes mellitus; top row: before contrast; bottom row: 20 min. following administration of Mn-DPDP, a manganese-based T_1 -shortening contrast agent. The graph at far right shows statistically significant lower enhancement of MR signal in patients with diabetes compared to normoglycemic controls. (Image: Botsikas, et al., 2012. Image courtesy of Taylor & Francis. Creative Commons.)

Based on this knowledge, we endeavored to use ^{52}Mn for PET imaging of pancreas function. For sufficient contrast to observe the pancreas, the signal from the pancreas needed to be significantly greater than from nearby tissues. Therefore, the high ^{52}Mn radioactivity that we observed in the liver and kidneys at 24-hour post-injection might pose a problem for imaging with ^{52}Mn at those timepoints. Therefore, we examined the biodistribution of free ^{52}Mn injected intravenously into healthy normal rats at timepoints extending up to 7 days. The results (Figure 3.5) showed that indeed the ^{52}Mn was retained at a higher level than the liver or kidneys at the longer timepoints of 3 and 7 days. For the same injections, we also examined the excretion profile of ^{52}Mn , and the results (Figure 3.6) agree with what we found in the literature that

manganese is excreted almost exclusively by the liver-bile-feces system, rather than through the kidneys and into the urine. The PET/CT imaging study in general-use rats (CD-1) revealed that by waiting 7-days post-injection can indeed provide adequate signal and contrast to visualize a healthy pancreas. A MIP of the co-registered PET/CT images (Figure 3.7) clearly shows signal from liver and kidneys, but much stronger signal from the region of the pancreas. This signal from the pancreas was confirmed by post-imaging *ex vivo* biodistribution (Figure 3.8).

3.5. Conclusions and Recommendations

- Biodistribution studies of intravenously injected $^{52}\text{Mn}(\text{II})$ in mice showed uptake in many organs, most interestingly: salivary glands, brain, thyroid, thymus, pancreas, liver, kidney, and bone.
- Similar studies in rats that extended to longer timepoints showed that activity in all of those organs decreases significantly over the course of seven days, except for brain, adrenals, and pancreas and confirmed that manganese is excreted almost exclusively through the feces and not the urine.
- Biodistribution studies of inhaled manganese in mice showed uptake in lung, brain, thyroid, pancreas, liver, and kidney.
- PET imaging of $[^{52}\text{Mn}]\text{MnCl}_2$ in mice and rats confirmed the observations from biodistribution, including high signal from ^{52}Mn in the pancreas at seven days post-injection, after the activity had significantly decreased in nearby tissues, such as the liver and kidneys.

- *Recommended future directions:* PET/CT imaging using a CT contrast agent that will reveal the pancreas on CT, which will enable quantitative imaging of free manganese in the pancreas with possible applications in diagnostic imaging of diabetes.

3.6. References

- Aerogen Corp., 2004. Aeroneb® Lab Nebulizer System Instruction Manual. Rev. C. Part no. AG-AL1010. Aerogen Corp., Dangan, Galway, Ireland.
- Aschner, M.; Aschner, J.L., 1990. Manganese transport across the blood-brain barrier: relationship to iron homeostasis. *Brain research bulletin* 24, 857-860.
- Aschner, M.; Gannon, M., 1994. Manganese (Mn) transport across the rat blood-brain barrier: saturable and transferrin-dependent transport mechanisms. *Brain research bulletin* 33, 345-349.
- Aweda, T.A.; Ikotun, O.; Mastren, T.; Cannon, C.L.; Wright, B., et al., 2013. The use of Ag as a tool for studying biological distribution of silver-based antimicrobials. *Med. Chem. Comm.* 4, 1015-1017.
- Aweda, T.A.; Zhang, S.; Mupanomunda, C.; Burkemper, J.; Heo, G.S., et al., 2015. Investigating the pharmacokinetics and biological distribution of silver-loaded polyphosphoester-based nanoparticles using (111) Ag as a radiotracer. *J. Labelled Comp. Radiopharm.* 58, 234-241.
- Baum, E.M.; Ernesti, M.C.; Knox, H.D.; Miller, T.R.; Watson, A.M., 2010. *Nuclides and Isotopes: Chart of the Nuclides*, 17th ed. Knolls Atomic Power Laboratory, Schenectady, New York, United States.
- Bertinchamps, A.J.; Miller, S.T.; Cotzias, G.C., 1966. Interdependence of routes excreting manganese. *Am. J. Physiol.* 211, 217-224.
- Botsikas, D.; Terraz, S.; Vinet, L.; Lamprianou, S.; Becker, C.D., et al., 2012. Pancreatic magnetic resonance imaging after manganese injection distinguishes type 2 diabetic and normoglycemic patients. *Islets* 4, 243-248.
- Brain, J.D.; Heilig, E.; Donaghey, T.C.; Knutson, M.D.; Wessling-Resnick, M., et al., 2006. Effects of iron status on transpulmonary transport and tissue distribution of Mn and Fe. *American journal of respiratory cell and molecular biology* 34, 330-337.
- Brenneman, K.A.; Wong, B.A.; Buccellato, M.A.; Costa, E.R.; Gross, E.A., et al., 2000. Direct olfactory transport of inhaled manganese ((54)MnCl(2)) to the rat brain: toxicokinetic investigations in a unilateral nasal occlusion model. *Toxicology and applied pharmacology* 169, 238-248.
- Buthieau, A.M.; Autissier, N., 1977. [The effect of Mn²⁺ on thyroid iodine metabolism in rats]. *Comptes rendus des seances de la Societe de biologie et de ses filiales* 171, 1024-1028.

- Chauncey, D.M., Jr.; Schelbert, H.R.; Halpern, S.E.; Delano, F.; McKegney, M.L., et al., 1977. Tissue distribution studies with radioactive manganese: a potential agent for myocardial imaging. *Journal of nuclear medicine* 18, 933-936.
- Cikrt, M., 1972. Biliary excretion of ²⁰³Hg, ⁶⁴Cu, ⁵²Mn, and ²¹⁰Pb in the rat. *British journal of industrial medicine* 29, 74-80.
- Crossgrove, J.S.; Allen, D.D.; Bukaveckas, B.L.; Rhineheimer, S.S.; Yokel, R.A., 2003. Manganese distribution across the blood-brain barrier. I. Evidence for carrier-mediated influx of manganese citrate as well as manganese and manganese transferrin. *Neurotoxicology* 24, 3-13.
- Crossgrove, J.S.; Yokel, R.A., 2005. Manganese distribution across the blood-brain barrier. IV. Evidence for brain influx through store-operated calcium channels. *Neurotoxicology* 26, 297-307.
- De Silva, R.A.; Jain, S.; Lears, K.A.; Chong, H.S.; Kang, C.S., et al., 2012. Copper-64 radiolabeling and biological evaluation of bifunctional chelators for radiopharmaceutical development. *Nucl. Med. Biol.* 39, 1099-1104.
- Deysach, L.J.; Ray, T.W., 1949. Absorption of Manganese by the Thyroid Gland of the Guinea Pig. *Experimental Biology and Medicine* 71, 188-189.
- Dorman, D.C.; Brenneman, K.A.; McElveen, A.M.; Lynch, S.E.; Roberts, K.C., et al., 2002. Olfactory transport: a direct route of delivery of inhaled manganese phosphate to the rat brain. *J. Toxicol. Environ. Health. Part A* 65, 1493-1511.
- Fore, H.; Morton, R.A., 1952a. The manganese in bone. *The Biochemical journal* 51, 598-600.
- Fore, H.; Morton, R.A., 1952b. Manganese in rabbit tissues. *The Biochemical journal* 51, 600-603.
- Gallez, B.; Bacic, G.; Swartz, H.M., 1996. Evidence for the dissociation of the hepatobiliary MRI contrast agent Mn-DPDP. *Magn Reson Med* 35, 14-19.
- Graves, S.A.; Hernandez, R.; Fonslet, J.; England, C.G.; Valdovinos, H.F., et al., 2015. Novel Preparation Methods of Mn for ImmunoPET Imaging. *Bioconjugate Chem.* 26, 2118-2124.
- Harisinghani, M.G.; Jhaveri, K.S.; Weissleder, R.; Schima, W.; Saini, S., et al., 2001. MRI contrast agents for evaluating focal hepatic lesions. *Clinical radiology* 56, 714-725.
- Heilig, E.A.; Thompson, K.J.; Molina, R.M.; Ivanov, A.R.; Brain, J.D., et al., 2006. Manganese and iron transport across pulmonary epithelium. *Am. J. Physiol. Lung Cell. Mol. Physiol.* 290, L1247-L1259.
- Hughes, E.R.; Miller, S.T.; Cotzias, G.C., 1966. Tissue concentrations of manganese and adrenal function. *Am. J. Physiol.* 211, 207-210.
- Kanayama, Y.; Tsuji, T.; Enomoto, S.; Amano, R., 2005. Multitracer screening: brain delivery of trace elements by eight different administration methods. *BioMetals* 18, 553-565.
- Kato, M., 1963. Distribution and Excretion of Radiomanganese Administered to the Mouse. *Q. J. Exp. Physiol. Cogn. Med. Sci.* 48, 355-369.
- Kawada, J.; Nishida, M.; Yoshimura, Y.; Yamashita, K., 1985. Manganese ion as a goitrogen in the female mouse. *Endocrinologia japonica* 32, 635-643.

- Kodama, H.; Shimojo, N.; Suzuki, K.T., 1991. Distribution of Manganese in Rat Pancreas and Identification of Its Primary Binding-Protein as Pro-Carboxypeptidase-B. *Biochemical Journal* 278, 857-862.
- Koshida, Y.; Kato, M.; Hara, T., 1963. Autoradiographic Observations of Manganese in Adult and Embryo Mice. *Q. J. Exp. Physiol. Cogn. Med. Sci.* 48, 370-378.
- Leblondel, G.; Allain, P., 1999. Manganese transport by Caco-2 cells. *Biological trace element research* 67, 13-28.
- Lewis, J.; Bench, G.; Myers, O.; Tinner, B.; Staines, W., et al., 2005. Trigeminal uptake and clearance of inhaled manganese chloride in rats and mice. *Neurotoxicology* 26, 113-123.
- Ni, Y.; Petre, C.; Bosmans, H.; Miao, Y.; Grant, D., et al., 1997. Comparison of manganese biodistribution and MR contrast enhancement in rats after intravenous injection of MnDPDP and MnCl₂. *Acta radiologica* 38, 700-707.
- Nishida, M.; Kawada, J., 1992. Hormonal control of manganese transport in the mouse thyroid. *Experientia* 48, 262-265.
- Papavasiliou, P.S.; Miller, S.T.; Cotzias, G.C., 1966. Role of liver in regulating distribution and excretion of manganese. *Am. J. Physiol.* 211, 211-216.
- Pautler, R.G.; Silva, A.C.; Koretsky, A.P., 1998. In vivo neuronal tract tracing using manganese-enhanced magnetic resonance imaging. *Magnet. Reson. Med.* 40, 740-748.
- Rabin, O.; Hegedus, L.; Bourre, J.M.; Smith, Q.R., 1993. Rapid brain uptake of manganese(II) across the blood-brain barrier. *Journal of neurochemistry* 61, 509-517.
- Ray, T.W.; Deysach, L.J., 1942. Storage of Manganese by Thyroid. Effect on Oxygen Consumption of the Guinea Pig. *Exp. Biol. Med.* 51, 228-229.
- Sakurai, H.; Nishida, M.; Yoshimura, T.; Takada, J.; Koyama, M., 1985. Partition of divalent and total manganese in organs and subcellular organelles of MnCl₂-treated rats studied by ESR and neutron activation analysis. *Biochimica et biophysica acta* 841, 208-214.
- Serrano, F.; Deshazer, M.; Smith, K.D.B.; Ananta, J.S.; Wilson, L.J., et al., 2008. Assessing transneuronal dysfunction utilizing manganese-enhanced MRI (MEMRI). *Magnet. Reson. Med.* 60, 169-175.
- Seshadri, M.; Hoy, A., 2010. Manganese-enhanced MRI of salivary glands and head and neck tumors in living subjects. *Magn. Reson. Med.* 64, 902-906.
- Suzuki, Y.; Mouri, T.; Suzuki, Y.; Nishiyama, K.; Fujii, N., 1975. Study of subacute toxicity of manganese dioxide in monkeys. *Tokushima J. Exp. Med.* 22, 5-10.
- Thompson, K.; Molina, R.M.; Donaghey, T.; Schwob, J.E.; Brain, J.D., et al., 2007. Olfactory uptake of manganese requires DMT1 and is enhanced by anemia. *FASEB J.* 21, 223-230.
- Tjälve, H.; Henriksson, J.; Tallkvist, J.; Larsson, B.S.; Lindquist, N.G., 1996. Uptake of manganese and cadmium from the nasal mucosa into the central nervous system via olfactory pathways in rats. *Pharmacol. Toxicol.* 79, 347-356.
- Tjälve, H.; Mejare, C.; Borg-Neczak, K., 1995. Uptake and transport of manganese in primary and secondary olfactory neurones in pike. *Pharmacol. Toxicol.* 77, 23-31.

- Wang, D.; Du, X.; Zheng, W., 2008. Alteration of saliva and serum concentrations of manganese, copper, zinc, cadmium and lead among career welders. *Toxicology letters* 176, 40-47.
- Yokel, R.A., 2002. Brain uptake, retention, and efflux of aluminum and manganese. *Environmental health perspectives* 110 Supp 5, 699-704.
- Yokel, R.A., 2006. Blood-brain barrier flux of aluminum, manganese, iron and other metals suspected to contribute to metal-induced neurodegeneration. *Journal of Alzheimer's disease* 10, 223-253.
- Yokel, R.A., 2009. Manganese flux across the blood-brain barrier. *Neuromol. Med.* 11, 297-310.
- Yokel, R.A.; Crossgrove, J.S.; Bukaveckas, B.L., 2003. Manganese distribution across the blood-brain barrier. II. Manganese efflux from the brain does not appear to be carrier mediated. *Neurotoxicology* 24, 15-22.

Chapter 4. Applications for ^{52}Mn in PET/MR Imaging^{1,2,3}

4.1. Background

An additional motivation for understanding the biodistribution of free manganese is that manganese(II) has been utilized in contrast agents for MR imaging. Manganese(II) is considered to be “high-spin” from its five unpaired valence electrons (Weinmann, et al., 1984; Wolf, et al., 1985), which shorten the spin-lattice time constant (T_1) for nearby ^1H nuclei, resulting in brighter signal when using a T_1 -weighted MR pulse sequence (Pan, et al., 2010; Rodriguez-Vargas, 2010; Silva and Bock, 2008), especially in anatomical regions with high water density. Since MRI is not inherently as quantitative as PET, and since MEMRI are not as widely studied as Gd-based agents, it could be useful to “authentically” radiolabel manganese-based MR contrast agents with radiomanganese (Klein, et al., 2005; Coenen, et al., 2014) for quantitative confirmation of their biodistribution—by dissection, autoradiography, and/or *in vivo* imaging.

¹ A.L.W. contributed to: experimental design, preparation of phantoms, and image analysis, preparation of figures and tables, and writing.

² Acknowledgments: Some of this work was performed by R.B. Gross and B.C. Lewis. I also acknowledge assistance with analysis of MR images from X. Nie (Lapi and Woodard groups); MR and PET/MR imaging performed at the Center for Clinical Imaging Research at WUSM/MIR with help from G.J. Foster and M.W. Harrod; and W.H. Margenau, P.M. Margenau, and G.G. Gaehle (WUSM/MIR) for operation and maintenance of the CS-15 cyclotron at WUSM/MIR.

³ Project-specific funding: This work was funded in part by an internal award from WUSM/MIR.

4.2. Experimental

4.2.1. MRI Phantom Imaging and Measurement of Relaxivity

In magnetic resonance techniques, including MRI, the magnetic spins of a sample are aligned to a strong external magnetic field and then a radiofrequency electromagnetic pulse temporarily realigns the magnetic spins of a selected frequency—typically the frequency of ^1H in the case of MRI. The exponential relaxation of nuclear spin to the original magnetic field is described by the spin-lattice relaxation constant (T_1), which is typically expressed in seconds. The T_1 relaxivity (r_1) of a T_1 contrast agent is often expressed in $\text{mM}^{-1}\cdot\text{sec}^{-1}$ (or similar units) and is the primary quantity used to compare the capability of a contrast agent to shorten T_1 for nearby nuclei. This change in T_1 causes brighter MR signal in that vicinity when imaging is performed using a T_1 -weighted pulse sequence.

We measured T_1 for several concentrations of Mn(II) in aqueous solution using an inversion-recovery experiment. Aqueous solutions of several different concentrations of $\text{Mn(II)Cl}_2\cdot 4\text{H}_2\text{O}$, ranging from 10 μM to 2 mM were prepared, and placed in several different conical centrifuge tubes upright in a rack. This rack was imaged using a birdcage head coil in the human-sized Biograph mMR PET/MR scanner (Siemens Medical Solutions USA, Malvern, Pennsylvania, United States) at the Center for Clinical Imaging Research (CCIR) at WUSM. The imaging was performed by an inversion-recovery MR pulse sequence at a range of values for the inversion time (TI). In this experiment, the real component of MR signal—positive or negative—in each concentration of MnCl_2 was imaged. Using the *ImageJ* software (Ferreira and Rasband, NIH/NIMH), the signal in the cross-section of each tube and the background was measured, and

the signal intensity (SI) from the background was subtracted from all signals. This was repeated for all values of TI , and the values for SI were plotted versus TI for each concentration of Mn(II).

Using the *Curve Fitting Toolbox* in the *MATLAB* software (MathWorks, Natick, Massachusetts, United States), the signal intensity (SI) versus TI data were fit to the equation (Hashemi, et al., 2010):

$$SI \propto M_0(1 - 2e^{-TI/T_1} + e^{-TR/T_1}), \quad (4.1)$$

where M_0 is the original longitudinal magnetization in arbitrary units, and TR is repetition time of the pulse sequence in sec. The result of the fit was a value for (T_1), expressed in seconds, for each concentration of Mn(II). The relaxation rate (R_1), which is expressed in sec^{-1} , for each concentration, was simply the inverse of T_1 , and r_1 was the slope of the linear fit of R_1 versus concentration of Mn(II).

4.2.2. PET/MR Phantom Imaging

This experiment was repeated as a PET/MR imaging study. Aqueous solutions of $\text{Mn(II)Cl}_2 \cdot 4\text{H}_2\text{O}$ were prepared in concentrations ranging from 10 μM to 2 mM and added different amounts of radioactivity of $^{52}\text{Mn(II)}$ ranging from 2-12 μCi . PET data was collected for 30 min. and MR images using an inversion recovery sequence for a variety of values for TI , with $TE=12$ msec using the Biograph mMR.

4.3. Results

A typical MR image from a phantom that included several different concentrations of non-radioactive Mn(II) at a few selected inversion times is shown in Figure 4.1. The signals resulting from an inversion-recovery sequence with numerous inversion times is shown in Figure 4.2, and the corresponding results for R_1 are plotted versus concentration of Mn(II) are plotted in Figure 4.3. The slope of the linear fit through those data yields the relaxivity of Mn(II)—specifically $\text{MnCl}_2 \cdot 4(\text{H}_2\text{O})$ —in water as $r_1 = 8.6 \text{ mM}^{-1}\text{sec}^{-1}$.

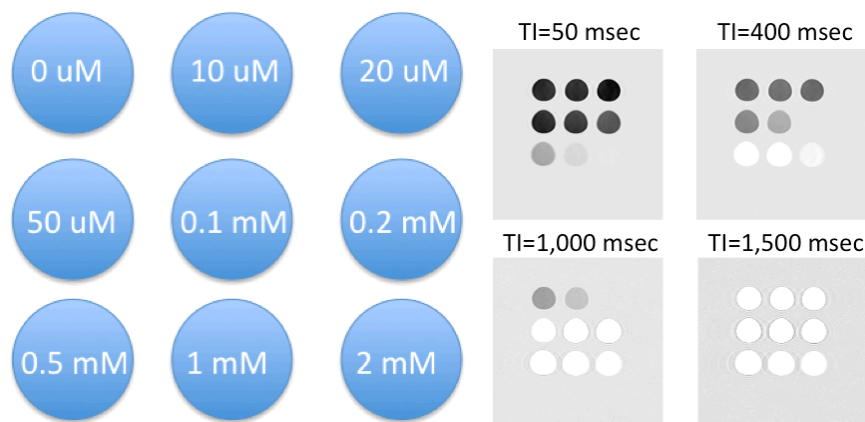


Figure 4.1. Phantom design and images from inversion-recovery MRI experiment with different concentrations of Mn(II) in water imaged at many different inversion times (TI). Images from only four of the TI values are shown here.

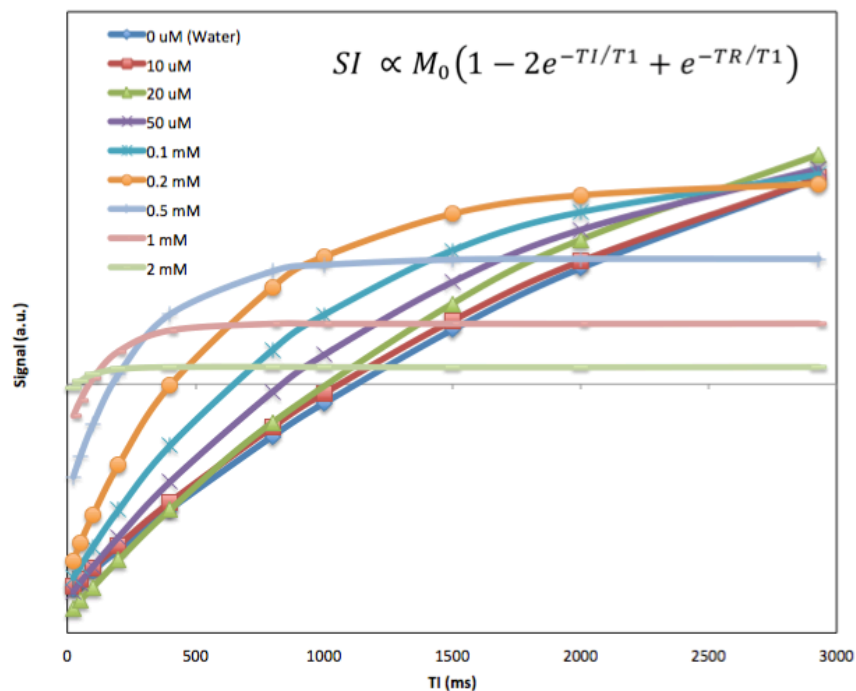


Figure 4.2. Results from inversion recovery experiment for several concentrations of Mn(II) solutions in water.

Signal acquired by real-component acquisition, signal from a region of the background was subtracted from all samples, and fitted to the equation shown. (Equation: Hashemi, et al., 2010).

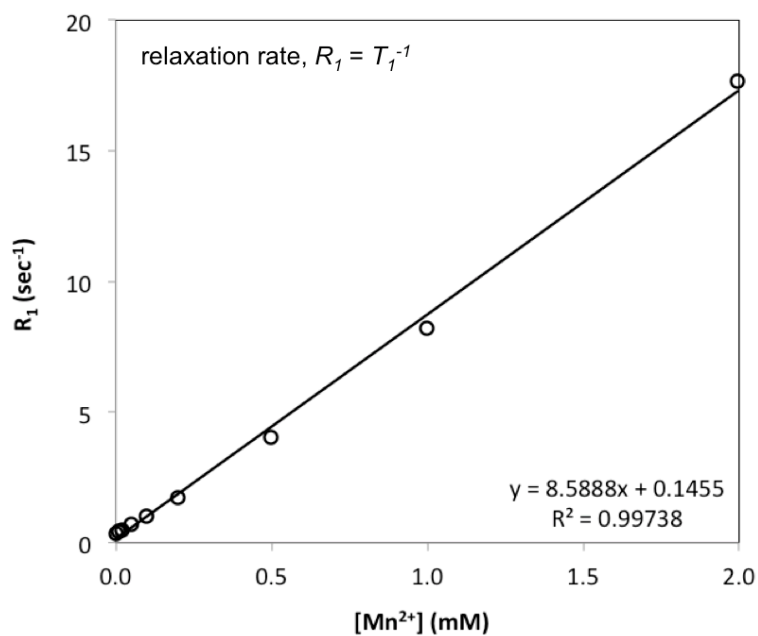


Figure 4.3. Plot of longitudinal relaxation rate (R_1) versus concentration of Mn(II) based on inversion recovery experiment.

Figure 4.4 shows the imaging results from PET/MR imaging of a phantom of aqueous solutions of different concentrations of non-radioactive Mn(II) as $\text{MnCl}_2 \cdot 4(\text{H}_2\text{O})$ and radioactive $^{52}\text{Mn}(\text{II})$. In both panels of Figure 4.4, the TE for MR and the PET imaging parameters were constant; however, the left panel shows MR signal from a pulse sequence with short TI and short TR , while the right panel shows MR signal from a pulse sequence with long TI and long TR .

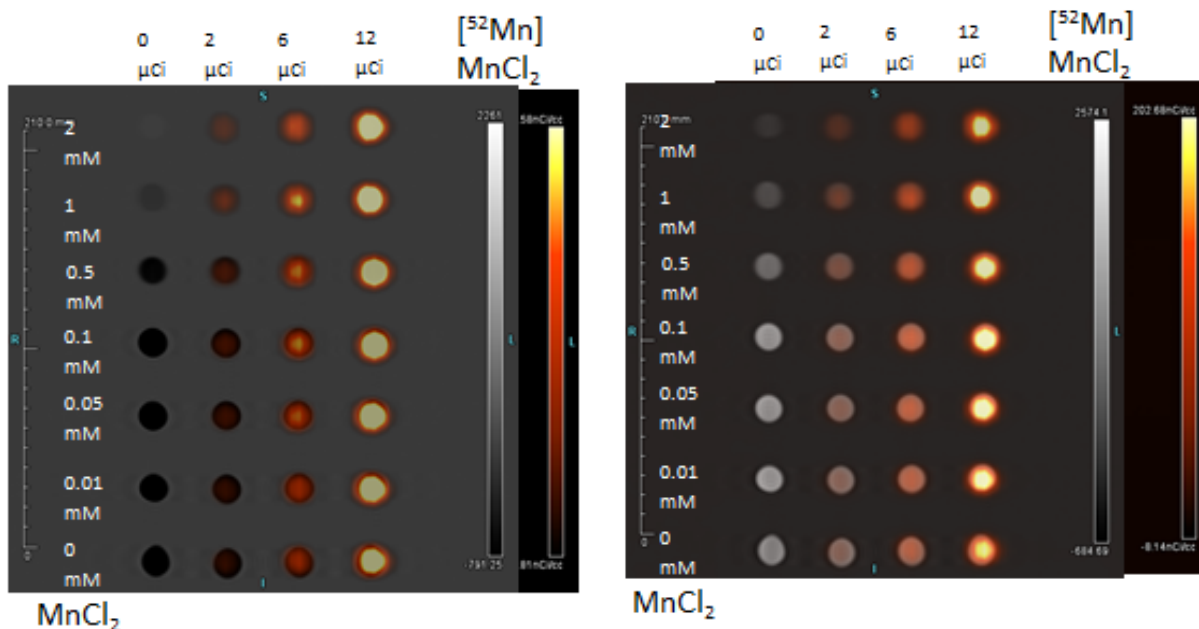


Figure 4.4. PET/MR images of phantom consisting of conical tubes containing aqueous solutions of different amounts of non-radioactive $\text{MnCl}_2 \cdot 4(\text{H}_2\text{O})$ and radioactive $^{52}\text{Mn}(\text{II})$. Images acquired in a Siemens mMR human scanner. PET: 30 min. acquisition; attenuation correction based on a Dixon sequence. MR: magnitude acquisition in an inversion-recovery sequence (left panel: $TR=3$ sec, $TE=12$ msec, $TI=50$ msec; right panel: $TR=10$ sec, $TE=12$ msec, $TI=9.93$ sec).

4.4. Discussion

The curve fits for both SI versus TI and R_I versus $[Mn(II)]$ were both very close, and the latter fit produced a result for r_I that was close to published values. These r_I values are less than for Gd(III) because it has seven unpaired valence electrons versus five for Mn(II), and the number of unpaired valence electrons is the most important characteristic of a T_1 -shortening contrast agent for MRI. The results from MRI-only images and quantification informed our selection of concentrations of non-radioactive Mn(II) for our phantom for PET/MR imaging. The PET/MR images demonstrated the feasibility of PET/MR imaging of dual-modality contrast agents that incorporate non-radioactive Mn(II) at sufficient concentrations to generate T_1 -weighted MR contrast and radiotracer concentrations of ^{52}Mn for generating PET signal. The phantom images from both short and long TI also provide examples of positive and negative MR signal resulting from different values of TI .

Compounds that can bind paramagnetic cations, such as Mn(II) (Section 1.2.3), hold potential for dual-modality PET/MR imaging if they can be radiolabelled with a radiotracer of the same cation. In unpublished results from collaborators at another institution, a compound has demonstrated the ability to bind manganese for potential MEMRI applications. In future work, we will endeavor to radiolabel this compound with ^{52}Mn for potential PET/MR imaging studies. This radiolabelling will be carried out by altering pH, confirmed by radio-HPLC, and applied to PET/MR imaging, first in phantom studies. Just as we demonstrated with our PET/MR imaging of free Mn(II)/ ^{52}Mn in solution in a phantom, any platform for a PET/MR contrast agent would require many times more atoms of non-radioactive metal compared to its PET radioisotope(s)

because PET inherently has much better sensitivity to PET radiotracers than MRI does to contrast agents for that modality.

4.5. Conclusions and Recommendations

- A phantom containing various concentrations of non-radioactive $\text{Mn(II)Cl}_2 \cdot (\text{H}_2\text{O})_4$ dissolved in water, was imaged by MRI using an inversion recovery pulse sequence. The signal from the images were analyzed, and these results were used to calculate the relaxivity of this compound in aqueous solution.
- Another phantom was constructed that contained a matrix of different concentrations of non-radioactive $\text{Mn(II)Cl}_2 \cdot (\text{H}_2\text{O})_4$ dissolved in water to which different amounts of ^{52}Mn had been added. This phantom was imaged by PET/MR and revealed changes in both MR and PET signals.
- *Recommended future directions:* Investigate the utility of ^{52}Mn by radiolabeling a compound that has been used to chelate Mn(II) for MRI imaging; perform PET/MR imaging of phantoms containing the compound complexed with non-radioactive Mn(II) and radioactive $^{52}\text{Mn(II)}$ in various concentrations and radioactivities.

4.6. References

Coenen, H.H.; Buchholz, M.; Spahn, I.; Vanasschen, C.; Ermert, J., et al., 2014. Towards authentically labelled bi-modal PET (SPECT)/MR-probes. Springer, p. A79.

- Hashemi, R.H.; Bradley, W.G.; Lisanti, C.J., 2010. MRI: The Basics, 3rd ed. Lippincott Williams & Wilkins, Philadelphia.
- Klein, A.T.J.; Rosch, F.; Coenen, H.H.; Qaim, S.M., 2005. Labelling of manganese-based magnetic resonance imaging (MRI) contrast agents with the positron emitter ^{51}Mn , as exemplified by manganese-tetraphenylporphin-sulfonate (MnTPPS4). *Appl. Radiat. Isot.* 62, 711-720.
- Pan, D.; Caruthers, S.D.; Senpan, A.; Schmieder, A.H.; Wickline, S.A., et al., 2010. Revisiting an old friend: manganese-based MRI contrast agents. *WIREs nanomedicine and nanobiotechnology* 3, 162-173.
- Rodriguez-Vargas, E.C., J.W., 2010. Magnetic Resonance Imaging Agents, in: Weissleder, R.R., B.D.; Rehemtulla, A.; Gambhir, S.S. (Ed.), *Molecular imaging*. People's Medical Publishing House-USA, Shelton, Connecticut, United States, pp. 389-404.
- Silva, A.C.; Bock, N.A., 2008. Manganese-enhanced MRI: an exceptional tool in translational neuroimaging. *Schizophrenia bulletin* 34, 595-604.
- Weinmann, H.J.; Brasch, R.C.; Press, W.R.; Wesbey, G.E., 1984. Characteristics of gadolinium-DTPA complex: a potential NMR contrast agent. *American journal of roentgenology* 142, 619-624.
- Wolf, G.L.; Burnett, K.R.; Goldstein, E.J.; Joseph, P.M., 1985. Contrast Agents for Magnetic Resonance Imaging. *Magnetic Resonance Annual*, 231-266.

Chapter 5. Remotely-Controlled Modules for the Isolation of PET Radiometals^{1,2,3,4}

This chapter describes purification modules that were designed, constructed, and wired for being controlled remotely by software running on a laptop. These modules are useful for isolating the product radionuclide from a bombarded solid target because the module can be placed inside of a lead hot cell, where the separation processes can be carried out. The user

¹ Much of this section was published previously or is being prepared for publication elsewhere:

Wooten, A.L.; Madrid, E.; Schweitzer, G.D.; Lawrence, L.A.; Mebrahtu, E., et al., 2013. Routine Production of ⁸⁹Zr Using an Automated Module. *Appl. Sci.* 3, 593-613.

Wooten, A.L.; Schweitzer, G.D.; Lawrence, L.A.; Madrid, E.; Lapi, S.E., 2012. An automated system for production of ⁸⁹Zr. *AIP Conf. Proc.* 1509, 201-205. 14th International Workshop on Targetry and Target Chemistry, Playa del Carmen, Mexico, 26-29 Aug. 2012.

Wooten, A.L.; Lawrence, L.A.; Lewis, B.C.; Mebrahtu, E.; Sultan, D.H.; Madrid, E.; Lapi, S.E. A remotely controlled, semi-automated module for the isolation of ⁸⁶Y from a proton-bombarded ⁸⁶SrO powder target. In preparation.

² A.L.W. contributed to the following aspects of projects in this chapter. For the ⁸⁹Zr module: module assembly, module installation inside hot cell, test productions of ⁸⁹Zr. For the ⁸⁶Y module: ordering and assembling components, electrical wiring, installation of module into hot cell, cold testing of module. For the ⁵²Mn module: design. For all modules: writing and preparation of figures and tables.

³ Project acknowledgments: The authors for the manuscripts mentioned above have contributed to design of the modules, assembly and automation of the modules, testing the modules with non-radioactive and radioactive materials. In particular, G.D.S. designed and assembled much of the ⁸⁹Zr module and participated in validation of the module; all *LabVIEW* programming for the ⁸⁹Zr and ⁸⁶Y modules was performed by L.A.L. (WUSM/MIR); most of the electronics were designed and installed by L.A.L.; and E. Madrid, E. Mebrahtu, and D.H.S. of the isotope production team (WUSM/MIR) have contributed to data from repeated productions during scaling up the levels of radioactivity and during routine production of isotopes. E. Mebrahtu performed much of the DFO titrations.

The authors acknowledge G.G. Gaehle (WUSM/MIR) for advice in designing automated modules; W.H. Margenau (WUSM/MIR) and J.W. Linders (Dept. of Chemistry, WUSTL) for constructing certain components of the systems; J.W. Linders and the WUSM Instrument Machine Shop for machining the Niobium target holders; G.G. Gaehle, W.H. Margenau, and P.M. Margenau (WUSM/MIR) for operation and maintenance of the cyclotron; and O.F. Ikotun (Lapi group) and B.V. Marquez (Lapi group) for general advice on ⁸⁹Zr separation chemistry and DFO titration.

⁴ Project-specific funding: This work was funded by the United States Department of Energy, Office of Science, Nuclear Physics Isotope Program under grant DESC0008657.

controls the module from outside the hot cell and thus receives significantly diminished radiation dose. Additionally, utilizing automated modules for separations can reduce opportunities for human error in a separation procedure and even improve the purity of the final product by reducing exposure to contaminants that may be present in a more open laboratory environment.

5.1. Background

Although the radionuclides and procedures can vary widely, certain design principles for production modules can be broadly applied. Section 5.1 provides background for the work presented later in this chapter by first examining other modules that have been published for production of radionuclides and radiopharmaceuticals. Despite increasing interest in recent years in using positron-emitting radiometals for pre-clinical and clinical PET imaging research, most of these isotopes are produced and shipped from only a few centers and companies worldwide. Consequently, there is not widespread demand for modules capable of producing PET radiometals. The vast majority of modules developed for production of PET radiometals are found in research literature, and special attention will be paid here to these examples.

Regardless of the radionuclide or the chemical process implemented, automated modules are typically designed to operate behind heavy radiation shielding, such as inside a hot cell, for scaled-up, high radioactivity processes. In addition to the primary objective of radiation shielding, a hot cell can provide a clean environment that is shielded from airborne contaminants in the lab, and the hot cell can also include air scrubbing, radiation monitoring, and live video feed of the module. Figure 5.1 shows examples of hot cells with and without a lead glass window.



Figure 5.1. Examples of commercially available hot cell capable of housing and integrating with automated modules.

A unit by Comecer (Castel Bolognese, Italy) containing two cells, one with a lead glass window, each containing a module connected by wire to an exterior laptop for monitoring and control. The top of the unit shows pressure monitors and radiation dose readouts for both cells and a video monitor for the bottom cell. The interior of these hot cells includes a tray on which to place a module for remotely-controlled chemistry, a video camera, vapor exhaust, power outlets, a rubber block of ports for feeding relatively large wires and tubes into the interior of the hot cell, and two septa for relatively small wires and tubes.

Several modules have been designed for the chemical isolation of PET radiometals. Production of PET radiometals tends to be centralized at a limited number of production centers that ship the radionuclides to end users. Thus, the modules that have been developed for production at these centers have not been imitated widely by other research institutions. In recent years, interest has increased in using antibodies and nanoparticles as platforms for imaging contrast agents, and certain positron-emitting radiometals, especially ^{64}Cu and ^{89}Zr , have emerged as valuable radiolabels for these potential agents (Section 1.4.4). Thus, there has been an increase automation for scaled-up production of ^{64}Cu and ^{89}Zr , and even a few commercially available modules have become available for these radionuclides. Table 5.1 summarizes a few published automated modules for the separation of $^{60,64}\text{Cu}$, ^{86}Y , and ^{89}Zr .

Table 5.1. Published automated modules for production of $^{60,64}\text{Cu}$, ^{86}Y , and ^{89}Zr .

Product Isotope	Chemical Form	Target ^a	Separation Process	Reference
$^{60/64}\text{Cu}$	$^{64}\text{Cu(II)}$ in 0.5 M HCl	enriched ^{64}Ni electroplated onto Au disc	Anion-exchange chromatography	(Kume, et al., 2012)
	$^{64}\text{Cu(II)}$ in 0.1 M HCl	"	"	(Burke, et al., 2010)
	$^{60/64}\text{Cu(II)}$ in 0.5 M HCl	enriched $^{60/64}\text{Ni}$ electroplated on Pt surface	"	(Matarrese, et al., 2010)
	$^{60/61/64}\text{Cu(II)}$ in 0.5 M HCl	enriched $^{60/61/64}\text{Ni}$ electroplated on Au surface	"	(Welch, et al., 2006)
^{86}Y	$^{86}\text{Y(III)}$ in 3 M HCl	$^{86}\text{SrCO}_3$ powder	Sr-specific resin, Y-specific resin, cation-exchange resin	(Park, et al., 2004)
^{89}Zr	Oxalic acid	$^{\text{nat}}\text{Y}$ metal foil	Cation-exchange chromatography via hydroxamate-functionalized resin	(Siikanen, et al., 2012)

^aDescription of the portion of the cyclotron target that enters the automated system. (Table from Wooten, et al., 2013. Table courtesy of MDPI. Creative Commons.)

5.1.1. Production and Applications of ^{89}Zr

The isotope ^{89}Zr is one of several positron-emitting radiometals that are increasing in popularity as radiolabels for PET (Anderson and Welch, 1999; Ikotun and Lapi, 2011; Nayak and Brechbiel, 2009; Wadas, et al., 2010). In particular, ^{89}Zr holds significant potential as a radiolabel for antibodies, antibody fragments, and peptides for the *in vivo* molecular imaging of antigens using PET (McCabe and Wu, 2010; van Dongen, et al., 2007; van Dongen and Vosjan, 2010; Verel, et al., 2005; Vugts, et al., 2013). Zirconium-89 is well-suited for this technique because it is a positron-emitter with a half-life that is long enough to accommodate the longer targeting time and biological half-life for these relatively large imaging agents. So far, the most prevalent application for ^{89}Zr has been cancer imaging. The information obtained using PET

imaging of ^{89}Zr compounds can be useful for cancer staging, therapy planning, and treatment monitoring, making ^{89}Zr a potentially valuable tool for personalized cancer care.

There are several properties of ^{89}Zr that make it an attractive radiolabel for peptides, antibodies, and nanoparticles. Most importantly, the half-life of ^{89}Zr ($t_{1/2}=3.3$ days) is close enough to the targeting time and biological half-life of antibodies and other macromolecules that could be used as targeting agents. Additionally, ^{89}Zr emits positrons with a sufficient branching ratio ($I_{\beta^+,total}=22.7\%$) and provides good spatial resolution in PET because it emits positrons at a low average energy ($E_{\beta^+,avg.}=396$ keV), and therefore a lower positron range (1.2 mm) (Disselhorst, et al., 2010) compared to several other PET isotopes. Unfortunately, ^{89}Zr also emits a high-energy (909 keV) gamma ray with a high branching ratio (99.0%), meaning that the dose rate for this isotope is significant ($\Gamma=6.6$ R $\cdot\text{cm}^2/\text{mCi}\cdot\text{h}$). The decay product of ^{89}Zr (and ^{89m}Zr) is always the stable nuclide ^{89}Y , so there is no additional dose from daughter nuclei. Figure 5.2 shows a simplified decay scheme for ^{89}Zr .

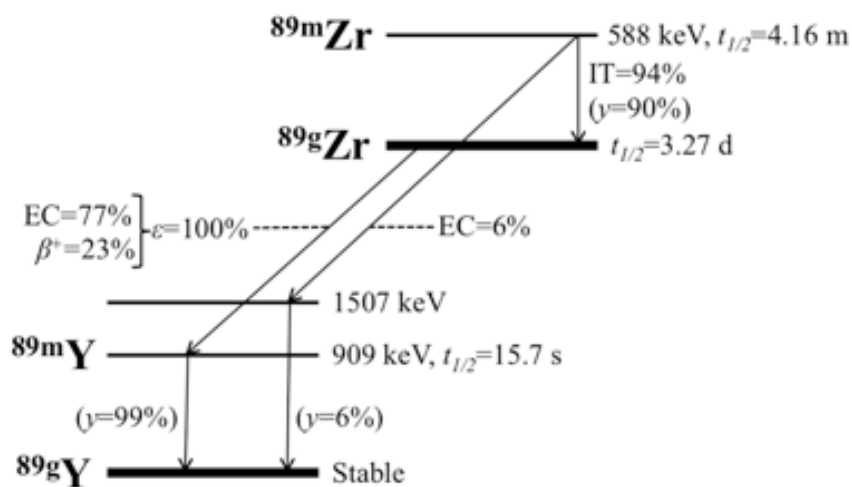


Figure 5.2. Simplified decay scheme for ^{89}Zr .
(Image: Wooten, et al., 2013. Image courtesy of MDPI. Creative Commons.)

The vast majority of medical centers capable of producing medical isotopes do so using a low-energy “biomedical” cyclotron capable of bombarding a target with protons with energy (E_p) <20 MeV (and alternatively deuterons with energy (E_d) <10 MeV). For these particles and energies, the highest cross-section is the (p,n) reaction with a peak cross-section of ~ 0.8 b at $E_p \sim 14$ MeV. The (p,n) reaction uses ^{nat}Y target material, which is monoisotopic as ^{89}Y and thus relatively inexpensive. For the above reasons, the $^{nat}\text{Y}(p,n)^{89}\text{Zr}$ reaction is the most common reaction route for ^{89}Zr production (Kasbollah, et al., 2013). However, contaminants can also be produced in a ^{nat}Y foil via the following common proton reactions: $(p,n)^{89m}\text{Zr}$, $(p,2n)^{88}\text{Zr}$, $(p,pn)^{88}\text{Y}$. Fortunately, high radionuclidic purity can still be achieved using ~ 15 MeV protons because ^{89m}Zr has a short half-life ($t_{1/2} = 4.2$ m) and a high degree of isomeric transition (IT = 93.8%) and because the $(p,2n)$ and (p,pn) reactions require greater proton beam energies, so they have low cross-sections at $E_p \sim 15$ MeV—less than 0.2 and 0.02 b, respectively (BNL/NNDC/CSISRS). Figure 5.3 shows plotted cross-section data for reactions that are relevant to bombardment of ^{nat}Y with low-energy protons: $(p,n)^{89g}\text{Zr}$, $(p,n)^{89m}\text{Zr}$, $(p,2n)^{88}\text{Zr}$, and $(p,pn)^{88}\text{Y}$, and the important characteristics of ^{89}Zr production in general are summarized in Table 5.2.

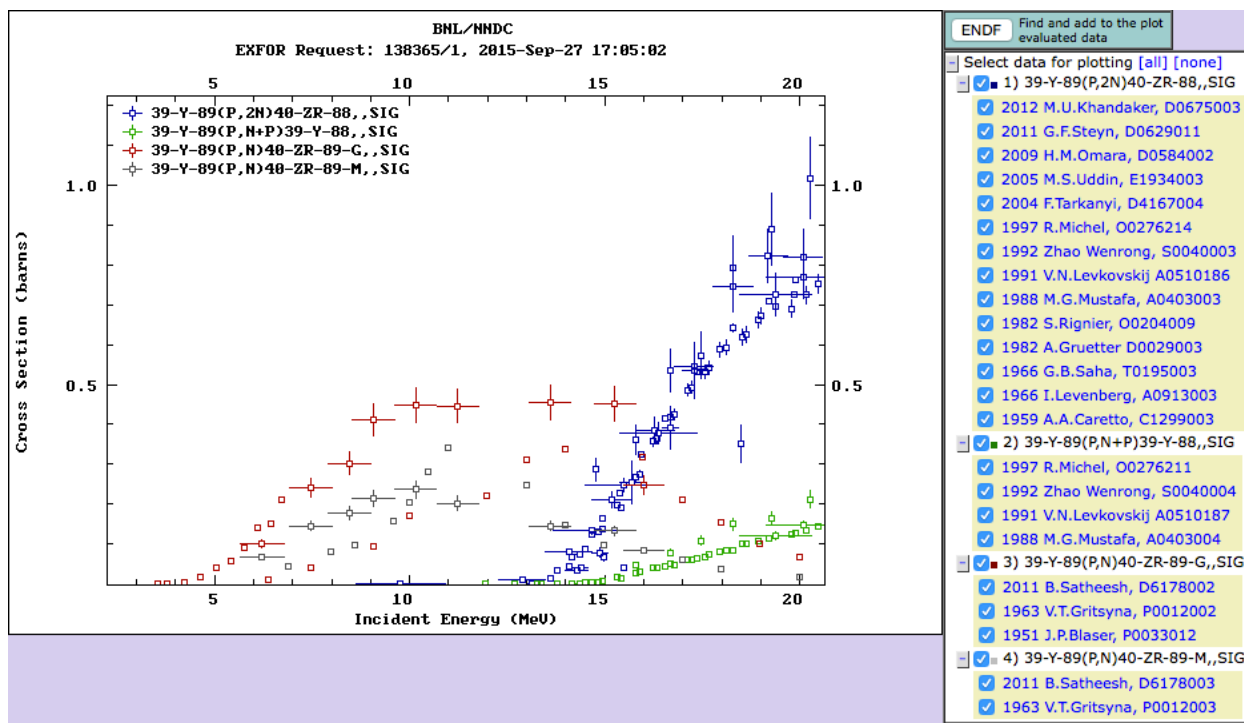


Figure 5.3. Screen shot of published cross-section data for reactions relevant to bombardment of ^{nat}Y with low-energy protons.

Screenshot of nuclear reaction cross-section data that were accessed via NRDC/BNL/NNDC/CSISRS and plotted using the X4-Servlet from BNL/NNDC. (Data accessed via: NRDC/BNL/NNDC/CSISRS; Otuka, et al., 2014; Zerkina, 2015.)

Table 5.2. Summary of characteristics for production of ^{89}Zr using a low-energy cyclotron.

Target (natural abundance)	^{nat}Y	(100% ^{89}Y)
Production reaction	$(p,n)^{89}\text{Zr}$	($t_{1/2} = 3.27$ days)
Reaction threshold		3.7 MeV
Stopping range of 14.7 MeV protons		1.02 mm
Other possible reactions	$(p,n)^{89m}\text{Zr}$	($t_{1/2} = 4.2$ m)
	$(p,2n)^{88}\text{Zr}$	($t_{1/2} = 83.4$ days)
	$(p,pn)^{88}\text{Y}$	($t_{1/2} = 107$ days)
Optimum beam energy, E_p		13 MeV
Target preparation		hot-rolled ^{nat}Y metal foil

Optimum beam energy was selected to avoid production of ^{88}Zr contaminant, while still producing ^{89}Zr . (Table from: Wooten, et al., 2013. Table courtesy of MDPI. Creative Commons.)

Out of several papers that we examined for using the (p,n) reaction for ^{89}Zr production and isolation, five used Y foil targets (Dejesus and Nickles, 1990; Dutta, et al., 2009; Holland, et al., 2009; Link, et al., 1986; Walther, et al., 2011), two used sputtered Y onto Cu (Meijs, et al., 1994; Verel, et al., 2003), and one used Y_2O_3 pellets (Kandil, et al., 2008). Although the sputtered targets provided superior heat transfer and therefore allowed for higher beam currents, we chose to use Y foil for ease of use. For a hypothetical irradiated Y foil that contains 100 mCi of ^{89}Zr , $<0.3 \mu\text{g}$ of ^{89}Zr atoms are present in the foil, and these product atoms must be extracted chemically to give the desired product—a solution containing $^{89}\text{Zr(IV)}$ ions. So far, the most prevalent chelator of the $^{89}\text{Zr(IV)}$ cation is desferrioxamine (DFO) (Deri, et al., 2013; Meijs, et al., 1992). This separation has been performed with mixed results using several different techniques (Holland, et al., 2009), including solvent extraction (Dejesus and Nickles, 1990; Dutta, et al., 2009; Kandil, et al., 2008; Lahiri, et al., 1997; Link, et al., 1986), cation-exchange (Dutta, et al., 2009; Kandil, et al., 2008), anion-exchange (Dejesus and Nickles, 1990; Kandil, et al., 2008; Link, et al., 1986; Zweit, et al., 1991), and solid hydroxamate resin (Fadeeva, et al., 1989; Herscheid, et al., 1983; Holland, et al., 2009; Meijs, et al., 1994; Verel, et al., 2003). Hydroxamate resin separation has emerged as the preferred method following the publication of a standardized method for producing and separating ^{89}Zr by Holland, et al. (Holland, et al., 2009). This separation can produce high recovery, radionuclidic purity, and effective specific activity (ESA). Our objective for this work was to automate the process that was reported by Holland, et al. (2009) based on chemistry that was developed by Verel, et al. (2003), Meijs, et al. (1994), and Herscheid, et al. (1983).

5.1.2. Production and Applications of ^{86}Y

Yttrium-86 is a medically important radioisotope for imaging by positron emission tomography (PET) because of favorable decay characteristics, amenability to radiolabelling, and because it has identical chemistry to ^{90}Y , a therapeutic radioisotope. The nuclear decay properties of ^{86}Y are summarized in Table 5.3. Yttrium-86 emits positrons at a low enough average energy ($E_{\beta^+,avg}=660$ keV) for acceptable spatial resolution in PET and with a total positron branching ratio ($I_{\beta^+,total}=31.9\%$) that is greater than the PET radiometals ^{64}Cu and ^{89}Zr (ENSDF/NNDC/BNL, 2015), providing more signal per radioactivity. The half-life ($t_{1/2}=14.7$ hours) for ^{86}Y is similar to the biological half-lives of peptides and antibodies, and it can be attached to these molecules with numerous bifunctional chelators, including derivatives of DTPA, DOTA, EDTA, NOTA, and TETA (Ikotun and Lapi, 2011; Wadas, et al., 2010; Nayak and Brechbiel, 2009). This capability makes ^{86}Y a suitable radiolabel for nuclear imaging of the biodistribution of these targeting molecules, along with ^{64}Cu , ^{89}Zr , and other radionuclides (Ikotun and Lapi, 2011; Nayak and Brechbiel, 2009). Additionally, ^{86}Y -PET can be applied to new molecules because chelating molecules, including derivatives of DOTA and DTPA, have proven useful for radiolabelling with ^{86}Y and ^{90}Y . This includes the FDA-approved radioimmunotherapy drug, Zevalin[®] (*ibritumomab tiuxetan*; Spectrum Pharmaceuticals, Henderson, Nevada, United States), which consists of a monoclonal antibody labeled with ^{90}Y chelated in a derivative of DTPA.

Table 5.3. Summary of chemical and nuclear decay properties of ^{86}Y with a simplified decay scheme.

Half-life, $t_{1/2}$	14.74 hours
Daughter isotope	100% ^{86}Sr (stable)
Decay modes	32% β^+ 68% EC
β^+ energy, $E_{\beta^+,avg}$	660 keV
γ -ray energy, E_γ (intensity)	1077 keV (82.5%)
Gamma factor ^a , Γ	18.9 $\text{R}\cdot\text{cm}^2\cdot\text{mCi}^{-1}\cdot\text{h}^{-1}$
Theoretical specific activity	212.53 $\text{Ci}\cdot\mu\text{mol}^{-1}$
Metastable isomer(s)	^{86m}Y

(Data: BNL/NNDC/ENSDF; ^aSmith and Stabin, 2012.)

In Zevalin and other applications of ^{90}Y , the radioisotope ^{111}In is often used as an imageable surrogate for ^{90}Y by single photon emission computed tomography (SPECT) for determining distribution and dosimetry. However, this approach suffers the limitations of SPECT with respect to spatial resolution and calculating dosimetry, and indium does not have exactly the same chemistry as yttrium, which would affect labeling efficiency and stability, as well as the *in vivo* distribution of any ions that might become de-complexed. Furthermore, different metal radiolabels, even while still chelated and bound to a peptide or antibody, can affect *in vivo* distribution. Yttrium-86 is attractive as a surrogate for ^{90}Y because it has identical chemistry to ^{90}Y and is imageable by PET, which has better spatial resolution than SPECT and is inherently quantitative for more accurate dosimetry calculations for ^{90}Y . Table 5.3 summarizes the nuclear decay and chemical properties of ^{86}Y .

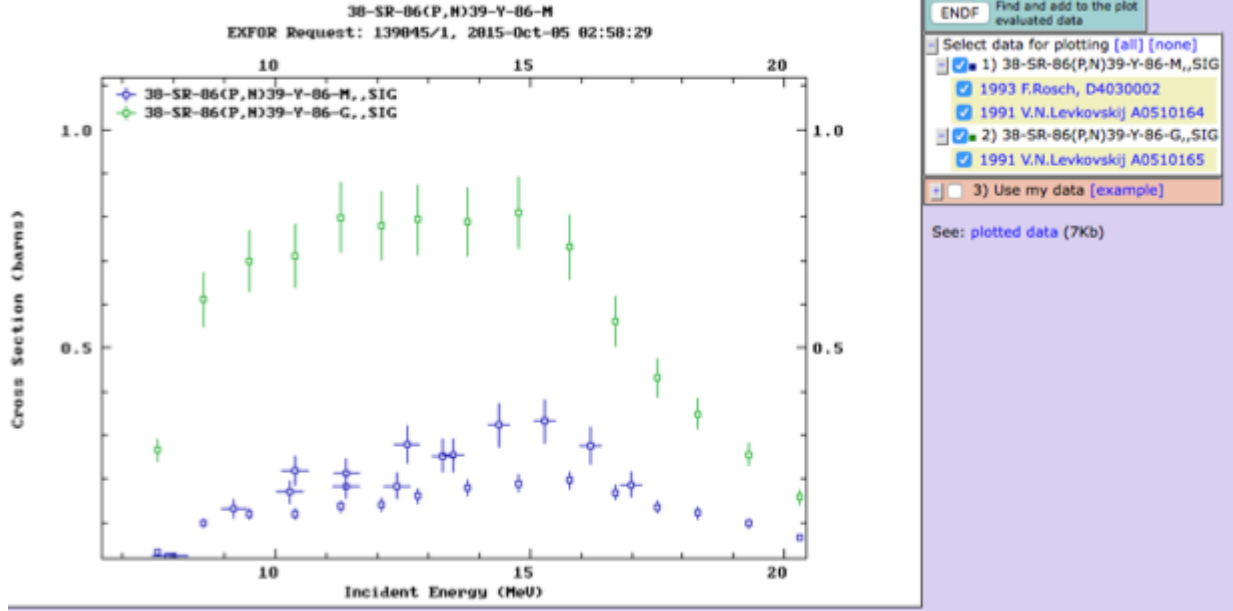


Figure 5.4. Cross-sections for the production of $^{86,86m}\text{Y}$ via bombardment of ^{86}Sr with low-energy protons.

Screenshot of nuclear reaction cross-section data that were accessed via NRDC/BNL/NNDC/CSISRS and plotted using the X4-Servlet from BNL/NNDC. (Data accessed via: NRDC/BNL/NNDC/CSISRS; Otuka, et al., 2014; Zerkin, 2015.)

Many PET centers that produce medical isotopes from cyclotron bombardment do so using low-energy medical cyclotrons with proton energies (E_p) < 20 MeV. At these energies, the most practical way to produce ^{86}Y by proton bombardment would be via the $^{86}\text{Sr}(p,n)$ reaction, which produces ^{86}Y with a maximum cross-section (σ_{max}) of $\sim 0.7\text{-}0.8$ b at $E_p \sim 11\text{-}15$ MeV and ^{86m}Y with $\sigma_{max} \sim 0.3$ b at $E_p \sim 14\text{-}15$ MeV (Figure 5.4). Furthermore, ^{86m}Y has a relatively short half-life ($t_{1/2} = 48$ min.) and undergoes isomeric transition to ^{86}Y with a branching ratio $> 99.3\%$, so it contributes significantly to production of ground-state ^{86}Y and is therefore not considered a contaminant for ^{86}Y production. Since strontium has four stable isotopes and ^{86}Sr is only 9.9% naturally abundant, it is preferable to bombard an enriched ^{86}Sr target, to reduce production of radiocontaminants from other isotopes of Sr in the target, such as $^{85,85m,87,88}\text{Y}$, ^{84}Rb , and ^{85}Sr , all of which have $t_{1/2} > 1$ h, as well as $\sigma < 0.1$ b at $E_p < 20$ MeV. Based on cross-section data, we

expected contamination from some of these products even with a perfectly enriched target, yet we only observed contamination from $^{87,88}\text{Y}$, which we believed resulted from enrichment <100% (see Results and Discussion). Since strontium is not stable in ambient conditions, several published studies used commercially available $^{86}\text{SrCO}_3$ powder as a target material, while Yoo *et al.* converted $^{86}\text{SrCO}_3$ to ^{86}SrO by thermal decomposition. In addition to having a greater percentage of ^{86}Sr by total mass than $^{86}\text{SrCO}_3$, they observed that ^{86}SrO tolerated higher proton beam currents because of better thermal conductivity. In this work, we have designed, built, and commissioned a module that has performed the separation of ^{86}Y safely and routinely.

5.2. Experimental

5.2.1. Materials

Natural yttrium foil was purchased from Alfa Aesar (Ward Hill, Massachusetts, United States), and niobium and platinum metals were purchased in rod form from A.D. Mackay (currently in Denver, North Carolina, United States). A silica-based weak cation-exchange resin was purchased from Waters (Milford, Massachusetts). The chelator DFO-NCS was purchased from Macrocyclics (Dallas, Texas, United States). Ultrapure (~18 M Ω) water was purified in a Millipore system (Billerica, Massachusetts) and was used for all other purposes, including cleaning the automated modules before each use and making solutions for DFO titrations. [^{86}Sr] SrCO_3 was purchased from Isoflex (San Francisco, California, United States). All other chemicals were purchased from Sigma-Aldrich (Saint Louis).

5.2.2. Cyclotron Production

5.2.2.1. Cyclotron Production of ^{89}Zr

Discs with diameter 9.5 mm were punched from 0.64 mm thick $^{\text{nat}}\text{Y}$ foil (disc mass ~ 0.2 g). Niobium metal target holders were machined, consisting of a base and a screw-on lid with a centered, circular hole to expose the target foil to the cyclotron beam. Niobium was selected because of its high melting temperature ($T_m = 2,468$ °C) and high chemical inertness (Greenwood and Earnshaw, 1997). A single $^{\text{nat}}\text{Y}$ disc was placed inside the target holder, as shown in Figure 5.5. Due to activation, many target holders were machined to allow residual activity to decay before reuse. Before each target holder was reused, it was scrubbed by hand using a cotton swab dipped into a slurry made from Al_2O_3 powder and water. The target holder was placed in 6 M HCl for 1–4 h for cleaning and dried in an oven. The target assembly was mounted in the CS-15 cyclotron (The Cyclotron Corporation, Berkeley, California, United States) at the Mallinckrodt Institute of Radiology (MIR) at Washington University in Saint Louis School of Medicine (WUSM) and bombarded with protons ($E_p \approx 14.7$ MeV) to produce ^{89}Zr via the $^{\text{nat}}\text{Y}(p,n)^{89}\text{Zr}$ reaction. The beam exit energy was $E_p \approx 7.9$ MeV, based on calculations performed using *The Stopping Range of Ions in Matter (SRIM)* software (Ziegler, et al., 2010), which implements the Bethe formula for stopping power. After E_p was degraded by the Y foil, the beam stopped in the base of the Niobium target holder, as calculated with *Transport of Ions in Matter (TRIM)* module within the *SRIM* package. During bombardment, the target holder assembly was cooled on the beam side by a He gas jet and on the reverse side by flowing chilled water ($T \approx 2.2$ °C). Following irradiation, the target remained in the solid target station for a few hours to allow for the decay of short-lived contaminants, especially $^{89\text{m}}\text{Zr}$ in the Y foil. Then, the

target assembly was removed by hand, and other short-lived contaminants were allowed to decay overnight while the target was in a shielded location. On the following morning, chemical separation was performed in the hot cell that contained the automated module.

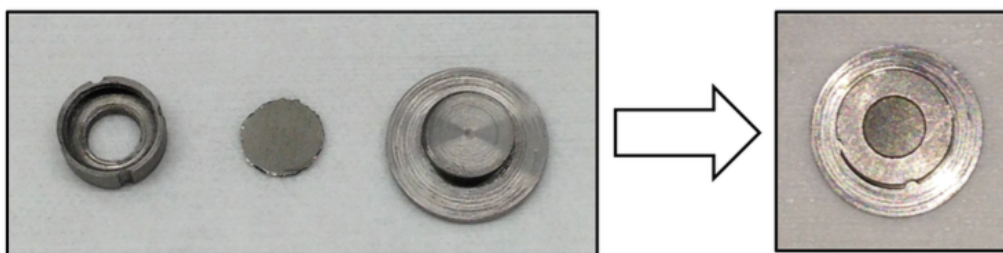


Figure 5.5. Photograph of the disassembled (left) and assembled (right) Y foil target and Niobium target holder.

(The samples on the left and right sides of the arrow above are photographs of representative samples, and they may not necessarily be the exact same samples.) (Image: Wooten, et al., 2013. Image courtesy of MDPI. Creative Commons.)

5.2.2.2. Cyclotron Production of ^{86}Y

The bare metal strontium is very chemically reactive due to rapid oxidation by air and reactivity with water, which produce strontium oxide and strontium hydroxide, respectively. Due to this reactivity, $^{86}\text{SrCO}_3$ was used as the initial material. $^{86}\text{SrCO}_3$ was heated at 1000-1100°C for 4-12 hours under Ar gas to produce ^{86}SrO , which was immediately stored in an evacuated vessel to prevent the spontaneous conversion back to $^{86}\text{SrCO}_3$ in air. The ^{86}SrO was preferred to $^{86}\text{SrCO}_3$ because Yoo, et al. (2005) noted that ^{86}SrO had a higher content of Sr per mass than $^{86}\text{SrCO}_3$ and observed experimentally that, relative to $^{86}\text{SrCO}_3$, ^{86}SrO could withstand greater beam current (6 vs. 2 μA) and could improve production yields of ^{86}Y (4.5 vs. 2.3 $\text{mCi}\cdot\mu\text{A}^{-1}\cdot\text{h}^{-1}$). Shortly before the start of cyclotron bombardment, the ^{86}SrO was compressed under 3,000 psi using a pneumatic press into a powder target holder made of platinum. The target holder consisted of a single piece of platinum, cut into a disk that fit into the solid target end station of

the cyclotron, with a dimple at the center cross hatched to improve the adhesion to the target material. The thickness of the compressed target is difficult to accurately measure, but assuming the powder is perfectly compressed, we estimated the target thickness to be $t = 4m/\pi d^2\rho = 1.16$ mm where m is the mass of the powder, d is the diameter of the cavity, and ρ is the density of the salt. The target was mounted in the CS-15 cyclotron (The Cyclotron Corporation, Berkeley) at the Mallinckrodt Institute of Radiology (MIR) and bombarded with protons to produce ^{86}Y via the $^{86}\text{Sr}(p,n)^{86}\text{Y}$ reaction.

5.2.3. Separation Chemistry

5.2.3.1. Separation Chemistry for ^{89}Zr

Figure 5.6 summarizes the general steps in our production process. A stock of hydroxamate resin was made by functionalizing the weak cation-exchange resin with hydroxamate groups according to a procedure published in Holland, et al. (Holland, et al., 2009), based on chemistry developed by others (Herscheid, et al., 1983; Meijs, et al., 1994; Verel, et al., 2003). Chemical separation of ^{89}Zr from the ^{nat}Y foil was performed in an in-house built automated module installed inside a lead hot cell (Comecer, Castel Bolognese, Italy), typically on the day after bombardment. During setup for each separation of ^{89}Zr , 100 mg of hydroxamate resin from this stock was loaded between two polyethylene (PE) frits (Grace, Deerfield, Illinois, United States), which were between two small pieces of glass wool, and loaded into a custom-blown glass column reservoir that was then incorporated into the system with air-tight connections. The entire irradiated target assembly—target holder and target foil—was quickly dropped into a Teflon dissolution vessel mounted on the automated system. This transfer was

performed manually, the door to the hot cell was then closed, and the remaining steps in the purification process were performed remotely.

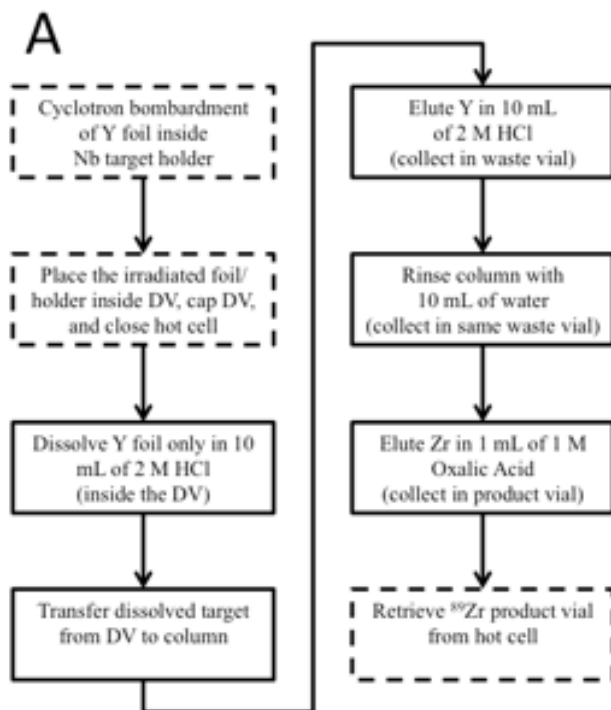


Figure 5.6. A flowchart describing the process for production and isolation of ^{89}Zr from an irradiated Y foil.

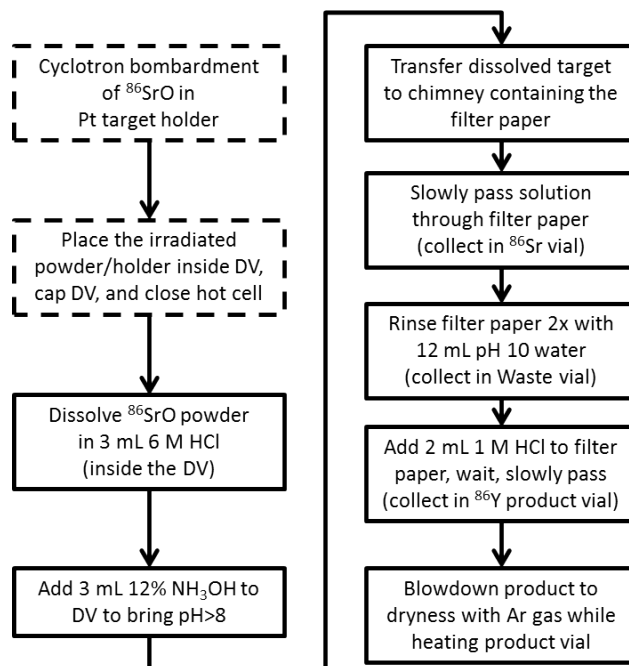
Solid line: automated steps; dashed line: steps that were performed manually. (Image: Wooten, et al., 2013. Image courtesy of MDPI. Creative Commons.)

Using a custom software program that was made in the *LabVIEW* platform (National Instruments, Austin, Texas, United States) running on a laptop outside the hot cell (Figure 5.10), 10 mL 2 M HCl was added to the dissolution vessel to dissolve the $^{\text{nat}}\text{Y}$ target. After waiting ~ 1 h for complete dissolution, the dissolved target was transferred to the column through tubing using compressed air. Then, the Y was eluted from the column in 10 mL 2 M HCl and collected in a waste vial, leaving the ^{89}Zr bound on the column. The column was rinsed with 10 mL water, which was collected in the same waste vial, and then the ^{89}Zr was eluted in 1 mL 1 M oxalic acid

and collected in a product vial as ^{89}Zr chelated by the oxalate ions (^{89}Zr -oxalate). Although other studies have achieved greater recovery and activity per volume by collecting multiple fractions from the column (Holland, et al., 2009; Meijs, et al., 1994; Verel, et al., 2003), we currently have automated the collection for only one elution of the product for simplicity in the automated module. However, to compensate for collecting a single fraction, we increased slightly the volume of eluent to 1 mL. After collection of ^{89}Zr in the product vial, the product was retrieved from the hot cell manually and then dispensed in 2 mL skirted microcentrifuge tubes for distribution within our institution and/or shipping to extramural researchers.

5.2.3.2. Separation Chemistry for ^{86}Y

A procedure for the chemical separation of ^{86}Y from ^{86}Sr was adapted from Avila-Rodriguez, et al. (2008) and is summarized in Figure 5.7. The separation was performed in an in-house built automated module installed inside a lead hot cell (Comecer, Castel Bolognese, Italy), typically a few hours after bombardment, to allow for the short lived $^{86\text{m}}\text{Y}$ to decay. During setup for each separation of ^{86}Y , new solutions were loaded into the source vials and a new filter was placed over the glass frit of the separation column. The irradiated target was quickly dropped into the Teflon dissolution vessel mounted on the automated system. This was done manually, the door to the hot cell was then closed, and the remaining steps of purification performed remotely.



Avila-Rodriguez, et al. *Appl. Radiat. Isot.* 2008.

Figure 5.7. A flowchart that describes the process for the production and chemical separation of ^{86}Y from an irradiated SrO target.

Dashed boxes indicate steps that were performed manually, solid boxes are automated steps.

A custom software program made in the *LabVIEW* platform was run on a laptop outside the hot cell to control the release of chemicals and transfer of material remotely. A volume of 3 mL of 6 M HCl was added to the dissolution vessel to dissolve the SrO target. After waiting ~5 min. for removal of the SrO powder from the target holder, 12 mL of 8 M NH_4OH was added. The colloidal solution was transferred to the 0.45 μm filter through tubing using compressed air. The $[\text{}^{86}\text{Sr}]\text{Sr}(\text{OH})_2$ passed through the filter. The first Sr fraction was collected. 2 x 12 mL of basic MilliQ water was passed to the dissolution vessel then the filter and extracted as a wash. A volume of 2 mL of 1 M HCl was slowly passed over the filter and the ^{86}Y product was collected. The product was brought to dryness at 130 $^\circ\text{C}$ under Ar gas.

5.2.4. Automated Module

5.2.4.1. Automated Module for ^{89}Zr

The path of fluids (liquids and air) through the system was controlled by solenoid-actuated isolation valves, and, as a fail-safe, solenoid-actuated pinch valves prevented liquids from flowing through the flexible tubing at inappropriate times or in the opposite direction. Solenoid valves were manufactured by NResearch (West Caldwell, New Jersey, United States). Solvents only came in contact with polymers and glass in the system. The compressed air was adjusted by a pressure regulator (Swagelok). The flow of compressed air was precisely controlled by a hot wire digital mass flow controller (Pneutronics) that received commands from the computer. Before each separation, all liquid solvents were pre-loaded into the system by hand in glass vials capped with silicone rubber septa that allowed for insertion of two PEEK needles—one connected to compressed air and one for transporting the liquid. The vials were then clipped onto the front of the module, and during the separation each liquid was extracted from its vial using positive pressure from the PEEK needle that was connected to compressed air. The general schematic of the entire system is shown in Figure 5.8.

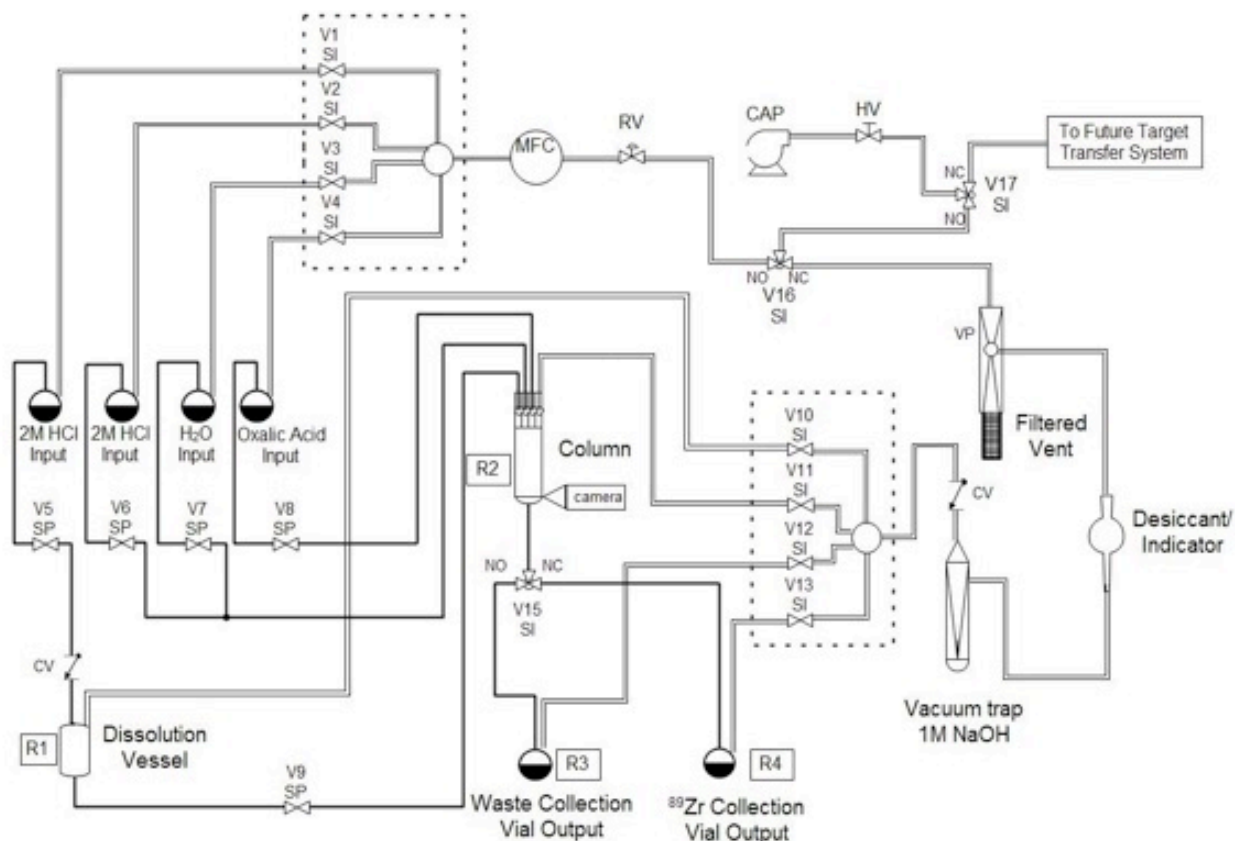


Figure 5.8. Process flow diagram for the automated module used for chemical separation of ^{89}Zr from irradiated ^{nat}Y foils.

CAP: compressed air pump; CV: check valve; HV: hand valve; MFC: mass flow controller; NC: normally closed; NO: normally open; R: radiation detector; RV: regulator valve; SI: solenoid isolation; SP: solenoid pinch; V: valve. Valves enclosed by a dashed box are part of a gradient manifold. Valves V14, V18, and V19 do not exist in the actual system, so they are not displayed here. (Image: Wooten, et al., 2013. Image courtesy of MDPI. Creative Commons. Original image was made using *Edraw Max* software (EdrawSoft, Sheung Wan, Hong Kong).)

An automated module was designed and built to perform a ^{89}Zr - separation protocol remotely inside a lead hot cell. The frame for this module ($h \times w \times d = 21 \times 18 \times 11$ in. = $0.53 \times 0.46 \times 0.28$ m) was constructed of extruded aluminum modular framing, to which walls were attached that were made of ultra high-molecular weight polyethylene. Various system components were mounted on these plastic walls, as pictured in Figure 5.9. The front panel of the module was hinged to allow easy access to the components and wiring inside the module. All liquids were pushed through the system by compressed air through flexible tubing. All liquid and

most gas connections were assembled using non-metallic connectors, which reduced exposure to metal contaminants. Many of the liquid connection pieces were designed for high-pressure liquid chromatography (HPLC) systems and were made of ethylene-tetrafluoroethylene (ETFE, Tefzel[®]); gas connections were made using stainless steel Swagelok[®] tube fittings (Swagelok, Solon, Ohio, United States).

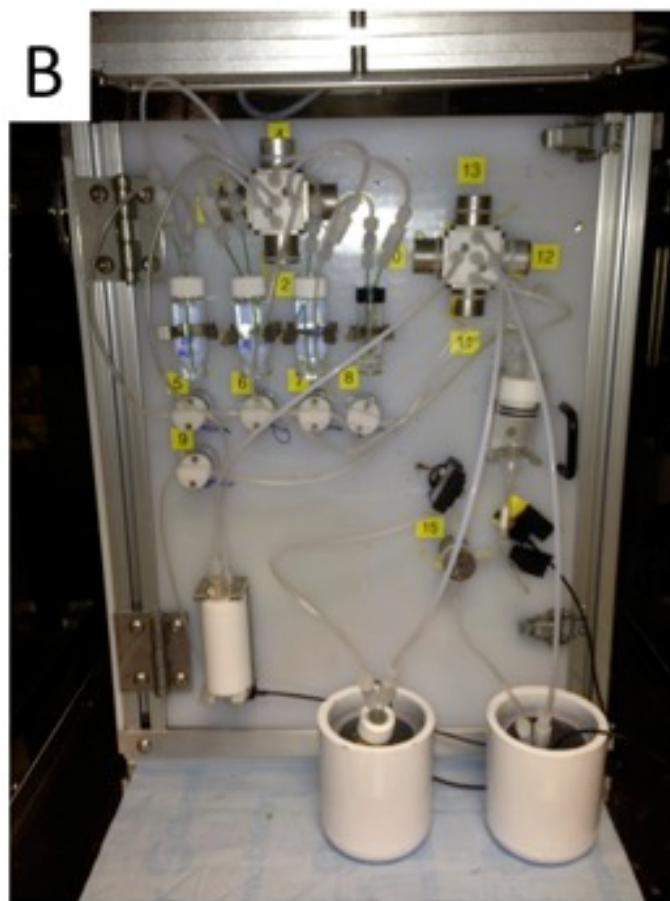


Figure 5.9. Photograph of the module for isolating ⁸⁹Zr from ^{nat}Y metal target material. The entire target holder assembly was placed in the dissolution vessel after bombardment, the ^{nat}Y target material itself was dissolved and transferred to the column for immobilization of the ⁸⁹Zr, leaving behind the Niobium target holder in the dissolution vessel. (Image: Wooten, et al., 2013. Image courtesy of MDPI. Creative Commons.)

A computer located outside of the hot cell was used to control the entire chemical separation process. A program was created on the *LabVIEW* platform that featured a graphical user interface (GUI) that provides instructions and controls for production personnel. Users could follow a step-by-step procedure with a pre-programmed control scheme and, if necessary, intervene by controlling individual valves in the event of a problem in the system. Using the GUI, the user can easily and precisely change the flow through the mass flow controller and thereby the speed at which liquids were pushed through the system, most importantly the speed of solvents through the column. We found that to improve recovery, the final eluent was allowed to sit on the column for ~ 20 min. and then slowly pushed through the column at $\sim 0.2\text{--}1$ mL/min. The GUI also included a live video feed from a mini color camera (ApexCCTV, Allen, Texas, United States) providing an up-close view of the liquid on the column, as well as real-time graphs that reported the radiation dose measured by four Si PIN-type photodiode detectors (Carroll & Ramsey, Berkeley, California, United States). These detectors were strategically placed close to the dissolution vessel, resin column, waste vial, and product vial (see Figure 5.8), allowing the user to monitor the movement of radioactivity through the system in real time. A screenshot of the GUI near the end of a separation process is shown in Figure 5.10.

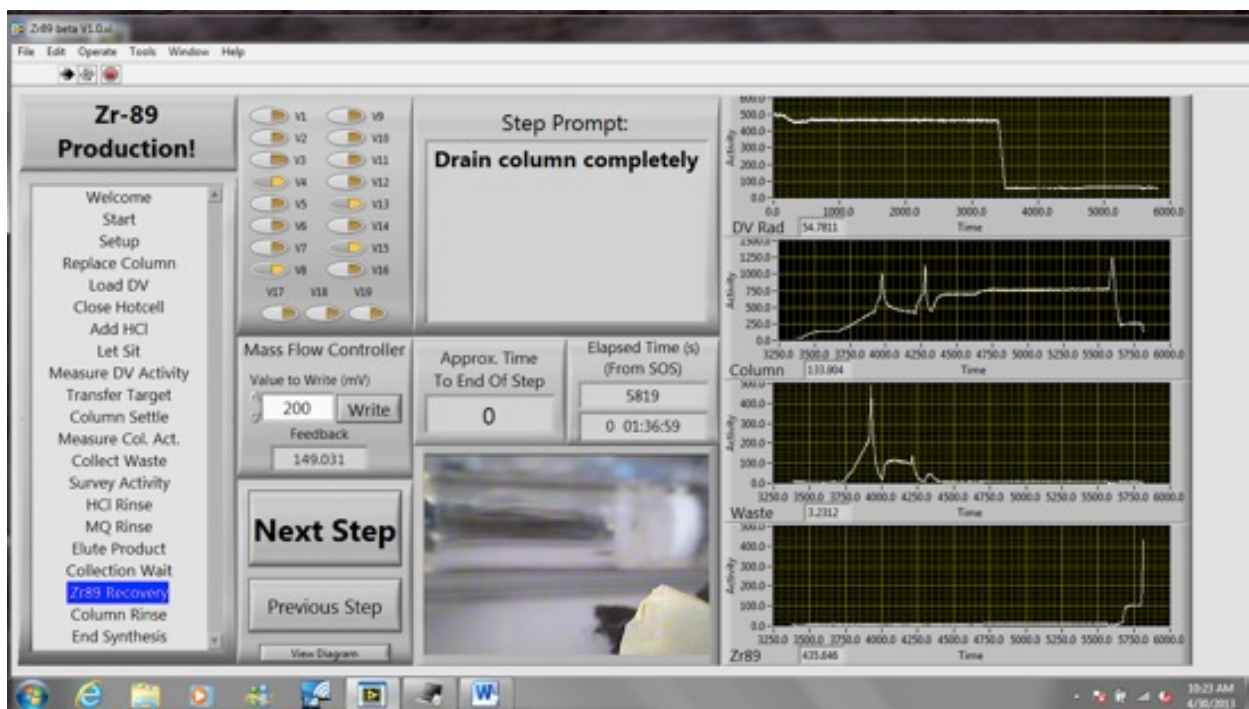


Figure 5.10. Screenshot of the window containing the graphical user interface (GUI) that was used to control the automated module.

(Image: Wooten, et al., 2013. Image courtesy of MDPI. Creative Commons. Program was created in the *LabVIEW* platform (National Instruments, Austin, Texas, United States). Programming performed by L.A. Lawrence.)

5.2.4.2. Automated Module for ^{86}Y

An automated module was designed and built to perform the separation of ^{86}Y and Sr inside of a lead hot cell. Madrid, et al. (2011) had previously developed a semi-automated module for the remote isolation of ^{86}Y at WUSM/MIR, and we benefited from the experience gained in producing that module and utilizing it for isolation of ^{86}Y ; however, a newer replacement module was needed. The walls of the module were of ultra-high-molecular weight polyethylene, and most components were mounted onto these plastic walls. The front wall of the module was hinged to allow easy access to wiring and internal components. Figure 5.11 shows a process flow diagram for the system. Vacuum from a Venturi pump was used to pull all liquids through the system through flexible tubing and through narrow needles made in-house from

polyetheretherketone (PEEK™) tubing. The Venturi pump was powered by compressed air from the building and the speed of liquids through the system was controlled by pulsing valves open and closed during a step in the process—instead of leaving them open continuously during the step for maximum speed of liquids. Solenoid-actuated isolation valves were used to control the path of liquids and gases through the system, and, as a fail-safe, solenoid-actuated pinch valves were used, to prevent liquids from flowing through tubing in the wrong direction or at incorrect times. Solenoid valves were manufactured by NResearch. A hand valve adjusted the compressed air that entered the system from the building supply. To reduce risk of metal contaminants, solvents only came in contact with polymers and glass in the system, and no metal components. All liquid solvents were pre-loaded into the system before each separation by hand in glass V-bottom vials, each capped with a lid that included a silicone rubber septa, which allowed for the insertion of PEEK needles for transporting air, vacuum, or liquids. The vials were clipped onto the front of the module, as seen in Figure 5.12. Each liquid was extracted from its vial by vacuum, necessitating vents on each input vial (Figure 5.11).

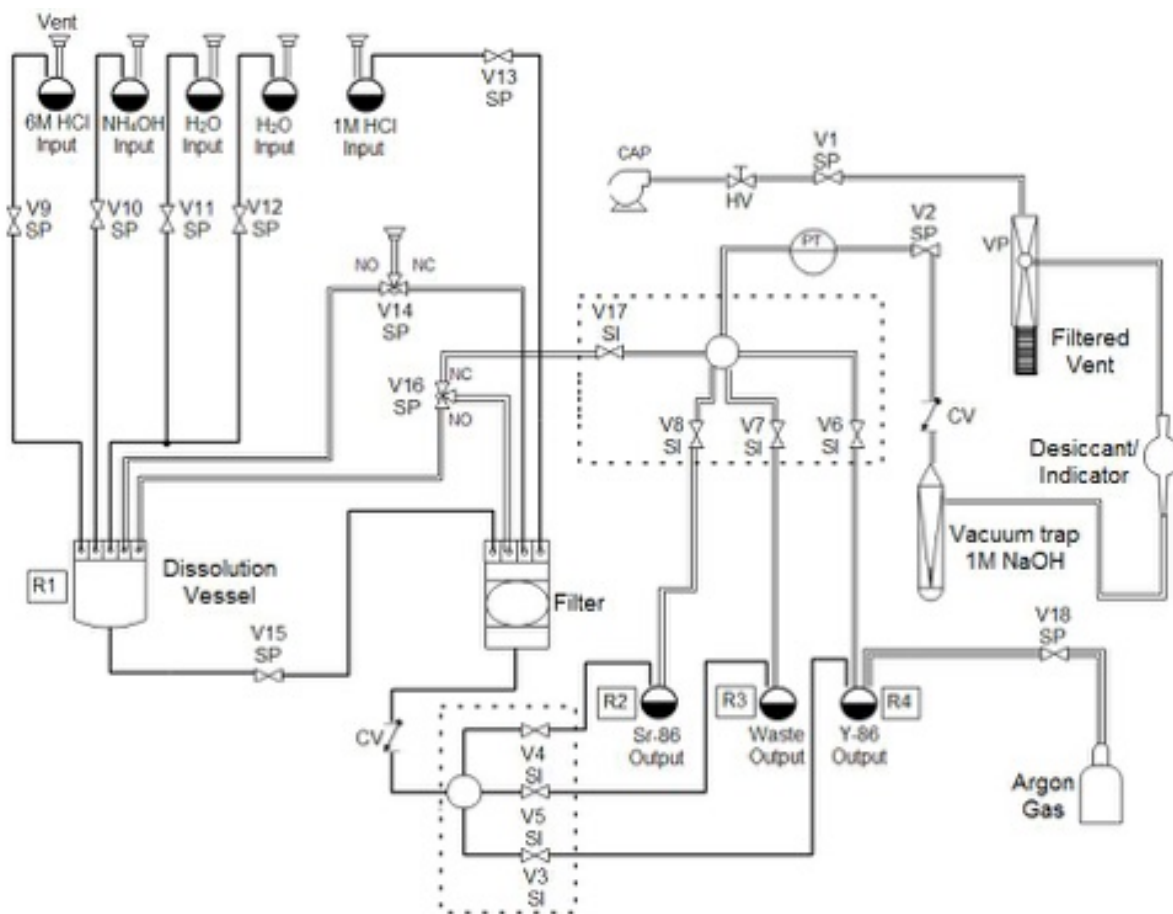


Figure 5.11. Process flow diagram for the automated module used for chemical separation of ^{86}Y from irradiated SrO powder targets.

CAP: compressed air pump; CV: check valve; HV: hand valve; NC: normally closed; NO: normally open; PT: pressure transducer; R: radiation detector; SI: solenoid isolation; SP: solenoid pinch; V: valve; VP: venture pump; double line: PTFE tubing for compressed air or vent only; triple line: PTFE tubing for Ar gas only. Valves enclosed by a dashed box are part of a gradient manifold. Not pictured: manometer. (Image was made using *Edraw Max* software (EdrawSoft, Sheung Wan, Hong Kong).)

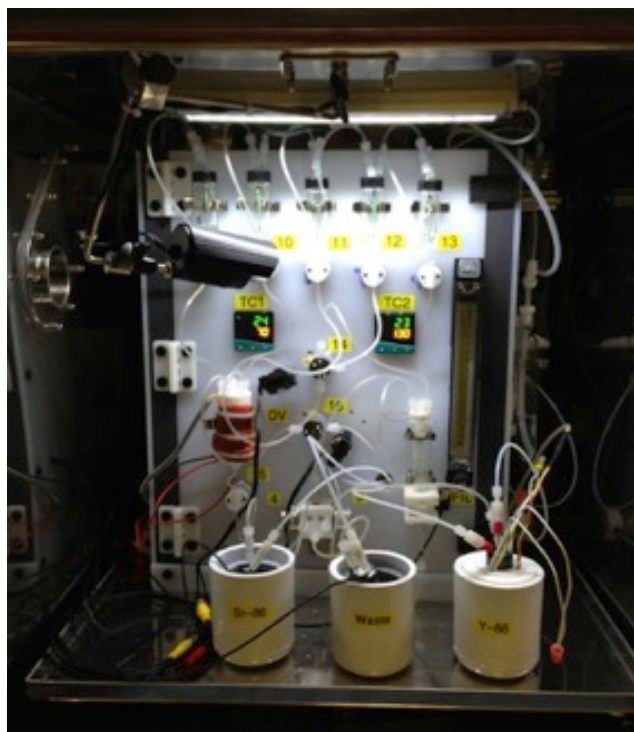


Figure 5.12. A photograph of the automated module for ^{86}Y .

To control the components of the module, a custom program was created in *LabVIEW*. This program included a GUI that provided instructions and controls for production personnel, as shown in screenshots in Figure 5.13. The computer followed a pre-programmed control scheme, that, if necessary, could be overridden to control individual valves in the event of a problem in the isolation process. The GUI also included a live video feed from mini color cameras (ApexCCTV), which provided up-close view of liquid at selected points in the system, such as, in Figure 5.13, the liquid passing onto the filter and the liquids flowing into output vials. Silicone PIN-type photodiode detectors (Carroll & Ramsey) can feed data to graphs in the GUI (Figure 5.13) to monitor the movement of radiation through the system, which is important information that is complementary to the visual movement of liquids provided by the video cameras.

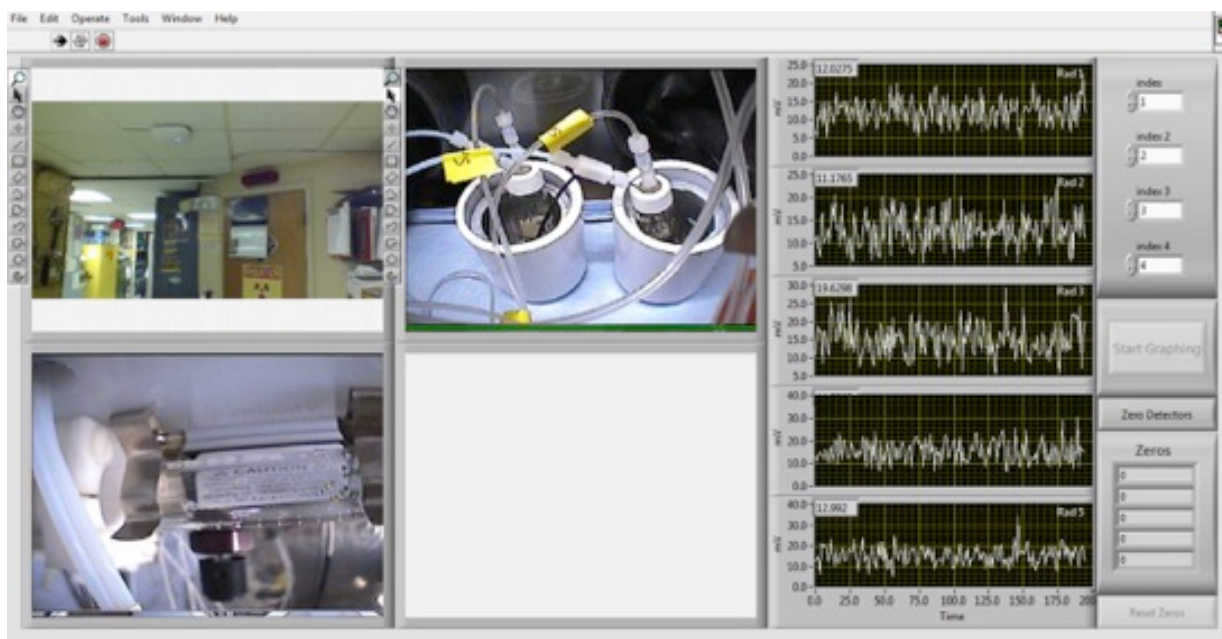
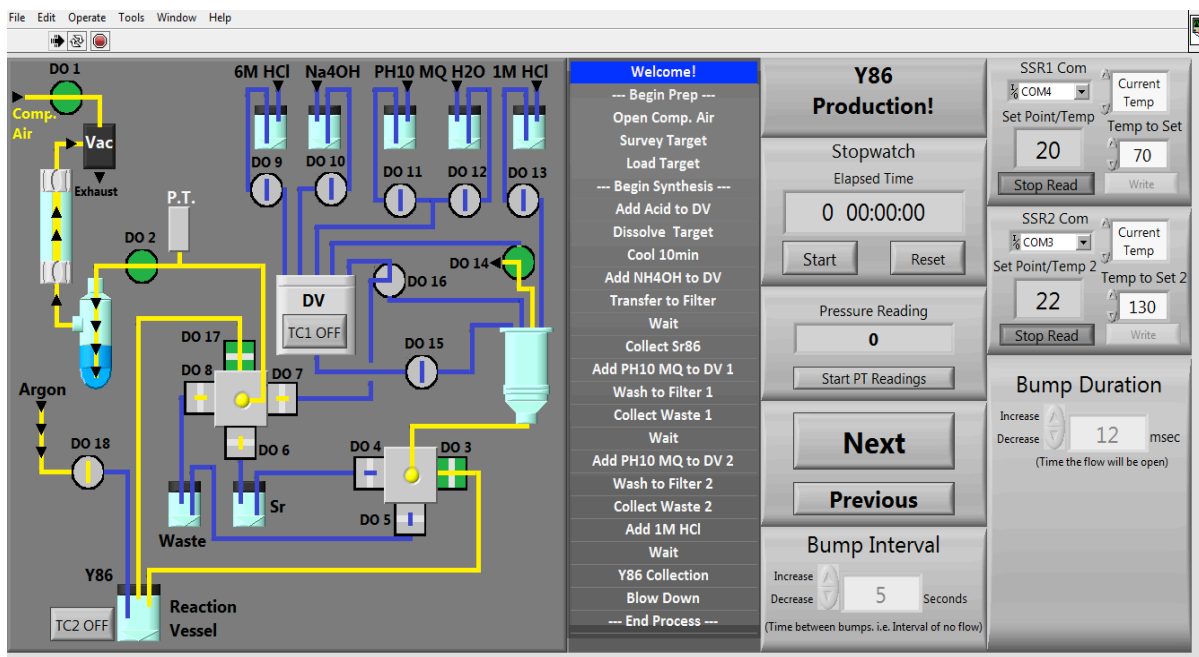


Figure 5.13. Screenshot of the window containing the graphical user interface (GUI) that controlled the automated module.

(Program was created in the *LabVIEW* platform (National Instruments, Austin, Texas, United States). Programming performed by L.A. Lawrence.)

5.2.4.3. Design of Automated Module for ^{52}Mn

As described in Chapter 2, we chose to bombard non-enriched, electroplated chromium ($^{\text{nat}}\text{Cr}$) because of reduced cost of material and the ability to produce batches of foil discs in an industrial hard chrome electroplating bath. These foils were held in a Niobium metal target holder with a screw-on lid that had an open window for the beam to pass through. $^{\text{nat}}\text{Cr}$ foils were bombarded with ~ 13.5 MeV protons from the CS-15 cyclotron at WUSM/MIR. In test separations performed by hand, and following the selected method from Graves, *et al.*, the bombarded foil was digested in HCl, then ethanol was added before the solution was passed through a 100-300 mg column of AG 1-X8 resin, an anion-exchange resin. Under these conditions of that procedure, Cr(III) was eluted, while $^{52}\text{Mn(II)}$ was immobilized on the column. Manganese-52(II) was eluted in 1 M HCl, dried down, re-dissolved in concentrated HCl, and then ethanol was added to return the activity to the previous conditions. The column was rinsed thoroughly with 2 M HCl, 6 M HCl, water, and then the ethanol/HCl mixture to restore it to its original condition. This separation procedure was repeated two more times, reusing the same resin each time. This procedure is summarized in Section 2.2.5.2, and a module was designed to automate this separation process.

The result for this section was a process flow diagram for an automated module that will be constructed in the future. This diagram is shown in Figure 5.14, and, once it is constructed, this will be controlled by a *LabVIEW* program running on a laptop, similar to the programs for controlling the modules for ^{89}Zr and ^{86}Y (Sections 5.2.4.1 and 5.2.4.2). This program will control all of the electric solenoid-actuated valves and valve manifolds in the system, which will determine the movement of liquids to various destinations in the system. This entire process will be monitored in real time by observing the transport of liquids with small digital cameras and the

transport of radioactivity with small semiconductor radiation detectors. The necessary combinations of valve openings and closings will be pre-programmed into a step-by-step sequence in the *LabVIEW* program, while retaining the capability to actuate any individual component at any time simply by clicking its corresponding button. This capability is important for reacting to unexpected situations that can occur with routine productions. To reduce risks of liquid leaks associated with pushing liquids using air at positive pressure, this module is designed to transport liquids that are pulled through the system by vacuum, similar to the ^{86}Y module (Section 5.2.4.2). The vacuum is generated by a Venturi pump that using a stream of compressed air originating from a source external to the module and hot cell. A digital MFC controlled by the *LabVIEW* program can control the flow rate of compressed air before the Venturi pump, thereby controlling the strength of the vacuum.

5.2.5. Product Characterization

The ^{89}Zr product was characterized for activity amount, radionuclidic purity, and ESA. The amount of activity that was recovered was measured using a dose calibrator (Capintec, Ramsey, New Jersey, United States). The radionuclidic purity was characterized using a high-purity germanium (HPGe) detector (Canberra, Meriden, Connecticut, United States). The product was diluted into a 2 mL skirted microcentrifuge tube, and a 10 min scan of the product was performed within one half-life of the original bombardment. To search for longer-lived contaminants, an aliquot of one production was allowed to decay for ~ 3 half-lives and then scanned for 12 hours. Gamma ray peaks were identified based on characteristic gamma-rays. Per Holland, et al. (2009), DFO titration was used to determine ESA, which is the radioactivity of the product isotope per total amount of metals in the product. To minimize non-specific binding of

other metals by the DFO, the DFO was challenged by 50 mM DTPA. The titration was carried out by thin layer chromatography (TLC) on pure cellulose blotting paper that was developed in 50 mM DTPA and scanned using a radio-TLC scanner (Bioscan, Washington, D.C., United States). At this point, the productions of ^{86}Y were mainly characterized by radioactivity as measured by an ionization dose calibrator.

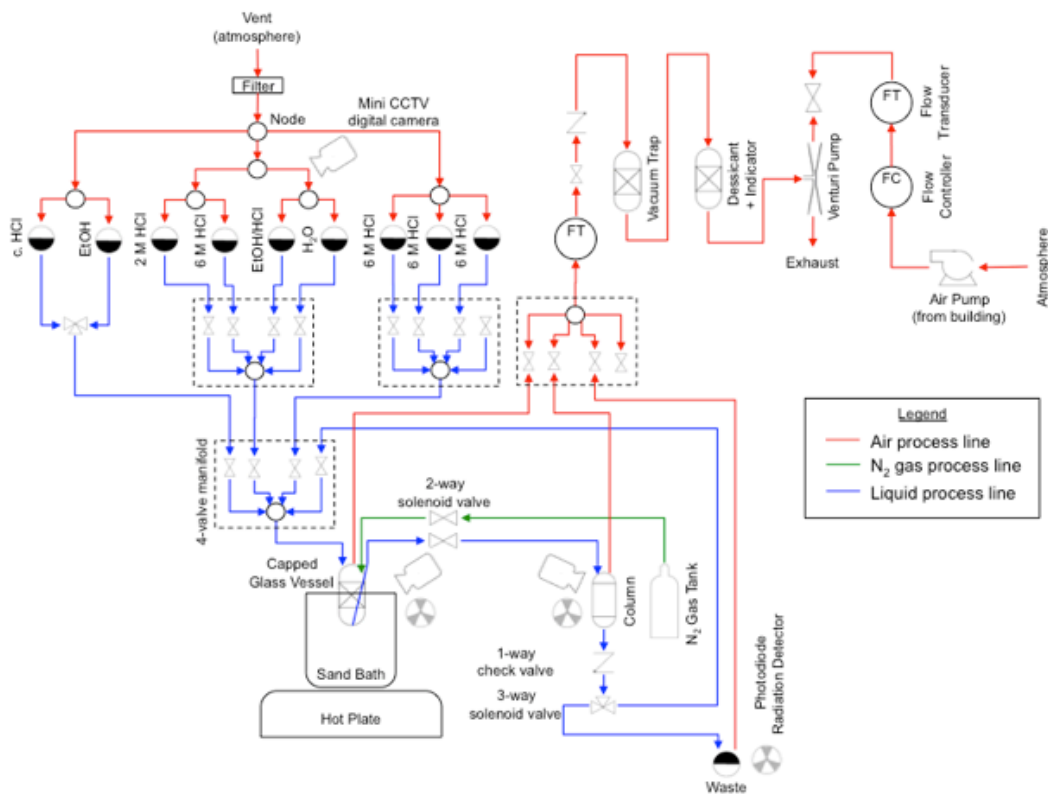


Figure 5.14. Process flow diagram for a module for the isolation of ^{52}Mn from Cr metal.

The final product was characterized for activity amount and radionuclidic purity. A dose calibrator (Capintec) was used to measure the amount of activity recovered. To characterize radionuclidic purity, the product was diluted in 2 mL skirted microcentrifuge tubes and scanned for 10 m, within one half-life of EOB, with a high-purity Ge detector (Canberra) connected to a

digital spectrum analyzer (Canberra). The samples were allowed to decay for ~3 half-lives and then scanned for 12 hours, to detect longer-lived contaminants.

5.3. Results

5.3.1. Results from Production of ^{89}Zr

The methods described in this work have been used successfully for several years for the cyclotron production and chemical separation of ^{89}Zr . Typically, after the chemical separation was completed using the automated module, a dose calibrator was used to measure the activity of ^{89}Zr collected in the product and waste vials. To reduce radiation dose, the system was allowed to decay for one week before measuring the dissolution vessel, which still contained the irradiated Niobium target holder, and the intact column assembly, which still included the resin, frits, and glass wool. The radioactivity measured for all four major module components was decay-corrected to the end-of-bombardment (EOB) time for each production. The decay-corrected activities were summed to give an estimated total radioactivity of ^{89}Zr produced in each cyclotron bombardment. This estimate neglects any activity that was lost in tubing, valves, *etc.*, but it allows us to compare the performance of the automated chemical separation for productions with different starting activities. The majority ($74\% \pm 16\%$) of ^{89}Zr was collected in the product vial and the largest loss of activity was to the column ($18\% \pm 15\%$), which was greater than either the waste vial ($4\% \pm 10\%$) or the dissolution vessel ($3\% \pm 3\%$), as shown in Figure 5.15.

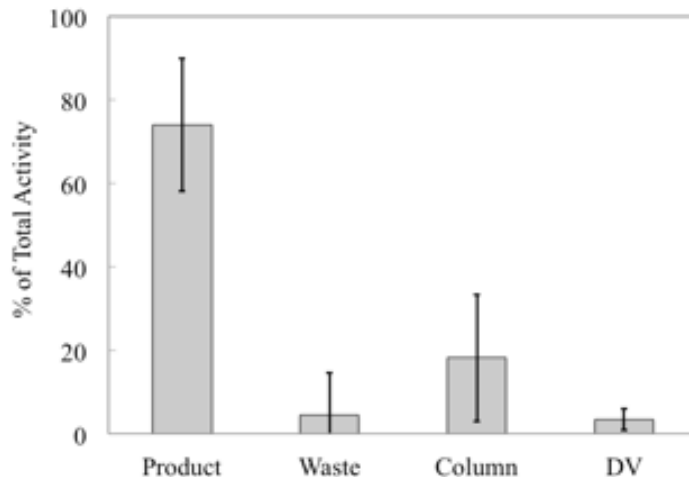


Figure 5.15. Distribution of ^{89}Zr in various components after each production.

For each production, the activity in each of the four primary system components was decay-corrected to a common time point (end-of-bombardment in the cyclotron) and calculated as a percentage of the total activity. Displayed here are the average percentages for each component \pm 1 SD. $N = 14$. DV: radioactivity remaining in the dissolution vessel after isolation process. (Image: Wooten, et al., 2013. Image courtesy of MDPI. Creative Commons.)

The percentage of ^{89}Zr activity collected in the product vial is the recovery rate of the chemical separation that was carried out using the automated module and is an important performance indicator for the separation process. In some cases this may be a result of us only collecting one elution instead of multiple fractions; otherwise, it may be because the stock of hydroxamate resin became less effective at binding Zr if it was stored for too long. We chose to make a stock of the resin for simplicity to avoid functionalizing a new batch of resin for each production.

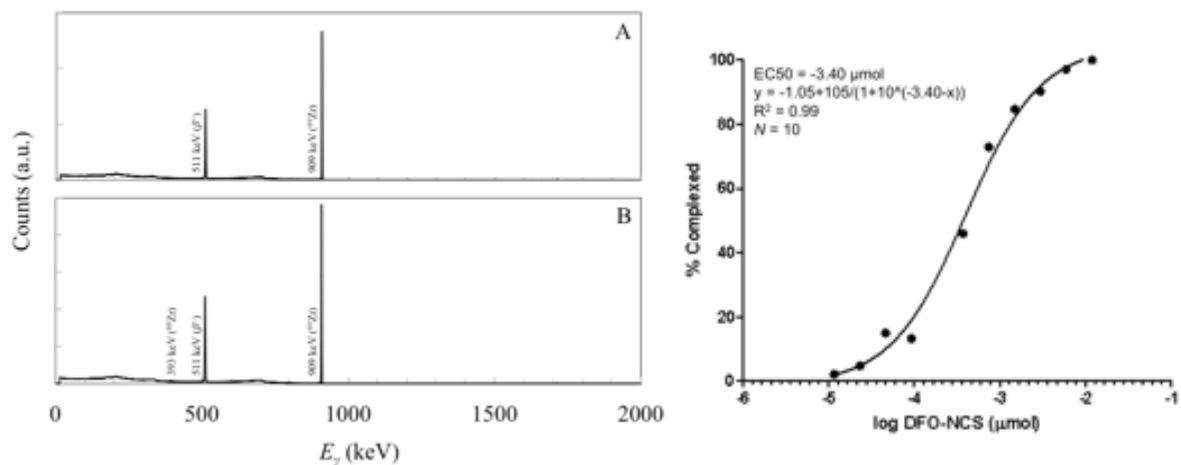


Figure 5.16. Gamma spectra of diluted aliquots from the product vial from two different productions. DFO-⁸⁹Zr titration curve that resulted in an effective specific activity of 63 mCi·μmol⁻¹ for a selected ⁸⁹Zr production.

(A) A 10 m scan taken on the same day as chemical separation, and (B) a 12 h scan taken 22 days after the chemical separation. E_γ : gamma-ray energy; a.u.: arbitrary units. Spectra were zoomed in on $0 \leq E_\gamma \leq 2,000$ keV. Right panel: sigmoidal dose-response curve. DFO titration experiment was performed by E. Mebrahtu. (Images: Wooten, et al., 2013 (supplementary information). Images courtesy of MDPI. Creative Commons.)

5.3.2. Results from Production of ⁸⁶Y

After chemical separation, the ⁸⁶Y product vial was removed from the hot cell and a dose calibrator was used to measure the activity of ⁸⁶Y collected. Before the next ⁸⁶Y production, the dissolution vessel, target, filter paper, and Sr fraction were all surveyed in the dose calibrator to estimate percent recovery. The radioactivity measured for all five components were decay-corrected to the EOB time for each production. The decay-corrected activities were then summed to give an estimated total radioactivity of ⁸⁶Y produced. Before placing the target into the automated module, the activity of the entire target was measured using a dose calibrator, which allowed for the percent activity in each component to be calculated. The majority (59%±14% (not relative uncertainty)) of the ⁸⁶Y was collected in the product vial, and the greatest loss of radioactivity was mainly lost in the elution of Sr (3%±4% (not relative uncertainty)). We found

that recovery of ^{86}Y was extremely dependent on the type of filter paper used, with the 0.45 μm mesh providing the best recovery.

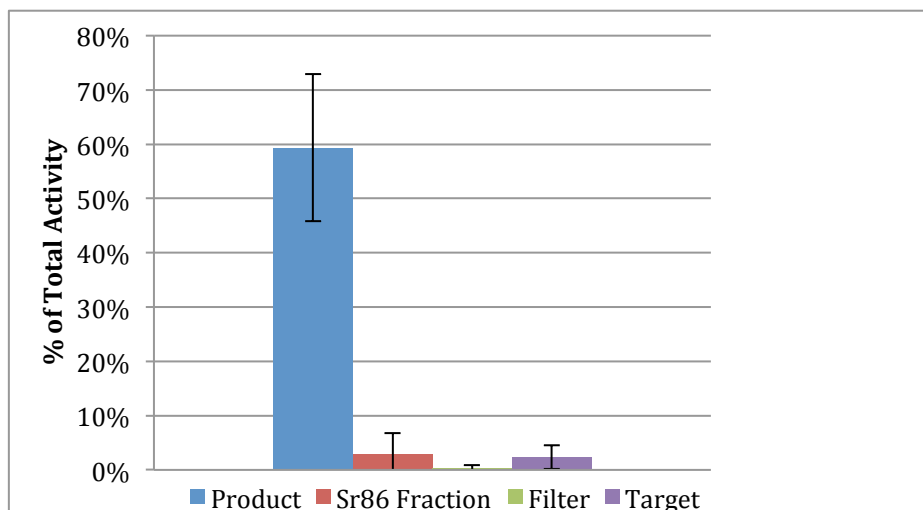


Figure 5.17. Distribution of ^{86}Y in various components after each production.

For each production, the radioactivity in the product, waste, and Sr vials, as well as on the filter, were decay-corrected to a common timepoint and calculated as a percentage of the total activity. Displayed in Figure 5.17 are the average percentages for each component, with error bars representing the 2σ (95%) confidence interval. The number of productions (n) represented by this data was $n=11$. It should be noted that this production data from using the module for ^{86}Y should be considered preliminary because it was collected during a phase of troubleshooting and optimization. Not included in this data were productions in which there was an obvious failure that resulted in a very large quantity of ^{86}Y not being isolated.

5.4. Discussion

5.4.1. Automated Module for ^{89}Zr

Automation is an important part of isotope production in particular and nuclear medicine in general because automated modules enable production centers to separate large activities of isotopes while still meeting institutional and federal regulations for radiation dose. Several groups have published on custom-made automated modules for various radiometals, including ^{64}Cu (Burke, et al., 2010; Kume, et al., 2012; Matarrese, et al., 2010; Welch, et al., 2006), ^{124}I (Nagatsu, et al., 2011), $^{99\text{m}}\text{Tc}$ (Chattopadhyay, et al., 2012), ^{86}Y (Park, et al., 2004), and ^{89}Zr (Siikanen, et al., 2012; Wooten, et al., 2012).

The Niobium target holders have been irradiated up to 15 μA without significant alterations of target or target holder. Since the same beam current, beam energy, and foil thickness were used for all productions in this work, the bombardment time (t_b) was the only bombardment parameter that was adjusted to control the amount of activity produced in the cyclotron. The parameters for comparable publications varied widely. Excluding the Y_2O_3 pellet targets, only one publication (Dejesus and Nickles, 1990) used a foil that was close to ours in thickness. Also, the beam current, bombardment time, and $\mu\text{A}\cdot\text{h}$ all varied widely across publications. Not surprisingly, the Y_2O_3 targets used lower currents, presumably because of reduced heat transfer, while the sputtered targets received high beam current for long bombardment times.

The predicted activity produced from a cyclotron was calculated by estimating beam energies at various points in the target using *SRIM* and calculating the reaction rate between these points using published empirical cross-section data for the $^{\text{nat}}\text{Y}(p,n)^{89}\text{Zr}$ reaction (Birattari,

et al., 1973; Blosser and Handley, 1955; Church and Caretto, 1969; Khandaker, et al., 2012; Michel, et al., 1997; Saha, et al., 1966; Uddin, et al., 2005). These data were accessed and plotted through the NNDC online database (NNDC/BNL), as shown in Figure 5.3. We estimated that 37% of the beam was lost in the rim of the lid of the target holder, instead of passing through the central window to irradiate the exposed ^{nat}Y foil. The reaction rate (R) was calculated, followed by the activity (A), using the standard equation for production of a radionuclide: $A = R(1 - e^{-\lambda t})$ (Ehmann and Vance, 1991), where λ is the decay constant for ^{89}Zr .

To confirm the radionuclidic purity of the solution in the product vial, gamma spectroscopy was performed. Typically, a short (10 min.) scan of a diluted aliquot from the product vial was performed on the same day as each chemical separation (Figure 5.16). For one production, a long (12 h) scan was performed after waiting for several half-lives (~22 days) of ^{89}Zr to allow it to decay relative to longer-lived potential radiocontaminants, making them easier to detect by gamma spectroscopy. This spectrum indicated a radionuclidic purity of ^{89}Zr equal to 99.998% of total activity (99.95% of total atoms) and identified ^{88}Zr as the only radiocontaminant. Even though our recovery percentage was less than other studies, our radionuclidic purity was on par with other publications, only one of which had a radionuclidic purity <99%. This high radionuclidic purity is likely because of the minimal overlap of the excitation function for the $^{nat}\text{Y}(p,n)^{89}\text{Zr}$ reaction with the $^{nat}\text{Y}(p,2n)^{88}\text{Zr}$ reaction, or any other potential reactions. For most productions of ^{89}Zr in this work, ESA was determined by DFO titration, similar to Holland, et al. (2009). ESA accounts for the presence of any metal isotope (stable or radioactive) that can be chelated by the selected chelator, in this case, DFO. For each production, the results of the DFO titration were plotted and fit with a sigmoidal dose-response curve to produce an EC50 value, which was used to calculate ESA in $\text{mCi} \cdot \mu\text{mol}^{-1}$.

In this work, we present the cyclotron production of ^{89}Zr using a biomedical cyclotron and the chemical separation of ^{89}Zr from a Y foil target using an automated module. This module dissolved the Y foil in acid and then separated the ^{89}Zr from Y using a hydroxamate resin column. Our methods reduced radiation dose to production personnel as the separation was carried out inside a lead hot cell, while the module was controlled by a laptop outside. The progress of the separation was monitored using radiation detectors in the module, and the final result for each production was a $^{89}\text{Zr(IV)}$ -oxalate solution, and this solution was characterized for recovery of activity, radionuclidic purity, and ESA. Our ^{89}Zr products had very high purity, similar to other published production methods. The procedures described in this work have been used for several years to routinely produce ^{89}Zr for users at our institution and for shipping to other institutions. Lessons learned from production of ^{89}Zr will be adapted for routine cyclotron production and chemical separation of other radiometals from solid targets.

5.4.2. Automated Module for ^{86}Y

In this work, we present the cyclotron production of ^{86}Y using a biomedical cyclotron and the chemical separation of ^{86}Y from a SrO powder target using an automated module. This module dissolved the SrO powder in acid and then separated the ^{86}Y from the Sr by passing through a filter in a basic solution. The ^{86}Y was then passed through the filter paper using acid and collected in a separate output vial. Utilizing this automated module for routine production of ^{86}Y would reduce radiation dose to personnel, as the separation was performed inside a lead hot cell and controlled remotely by a computer that was located outside of the hot cell. The separation process was monitored with radiation detectors and cameras positioned on the module at strategic locations, and the final product for each production was a no-carrier-added solution

of ^{86}Y in 1 M HCl. Drying down this product would reduce risk of spills and leaks during transport, and it could facilitate solvent exchange from 1 M HCl to a different desired solvent. We do not anticipate that drying down ^{86}Y in 1 M HCl would compromise the solubility of the ^{86}Y product in water, so we expect that it can be re-dissolved easily.

As mentioned earlier, the production results from the ^{86}Y module that are presented in this chapter should be considered preliminary data. Not included in this data were productions in which there was an obvious failure that resulted in a very large quantity of ^{86}Y not being isolated. Also, there were many productions in which the pressed powder target did not survive the cyclotron bombardment, resulting in a target with very little powder remaining in the dish of the target holder. (Currently, the powder targets for production of ^{86}Y are covered.) The results that are presented in this dissertation for the semi-automated isolation of ^{86}Y are from relatively early productions for this new module, which has been used more since those productions were performed.

5.4.3. Automated Module for ^{52}Mn

^{52}Mn is an important radioisotope of manganese for studying the chemical behavior of manganese in many applications. Manganese-52 also has attractive nuclear decay properties that make it attractive for radiolabelling of agents with long biological half-lives, such as macromolecules and nanoparticles, because of its long half-life, low positron energy, and sufficient branching ratio for positron emission. Many methods for isolating ^{52}Mn from bombarded chromium target material have been proposed, but a very recent method utilizing a solution of ethanol and concentrated HCl to elute Cr(III) seems very efficient, robust, and suitable for automation. Thus, an automated module is a logical and important next step in the

routine production of ^{52}Mn . Because of the half-life of ^{52}Mn , it is practical to ship it domestically or even internationally without losing too much of it to decay. Therefore, it is likely that only a few automated modules will be constructed in the foreseeable future and that these units will be used to produce large enough batches that can be aliquotted and shipped to meet demand.

As discussed in Chapter 2, scaled-up production of ^{52}Mn can be achieved by bombarding Cr metal targets that are isotopically enriched ^{52}Cr and/or greater in thickness, increasing proton energy not beyond ~ 24 MeV, or bombarding with deuterons in the $40 \rightarrow 8$ MeV range. Radiocontaminants co-produced from the latter two solutions would be easily removed by decay ($^{51,52\text{m}}\text{Mn}$ and ^{52}V) or by chemical isolation of ^{52}Mn from the chromium target material (^{51}Cr).

Manganese-52 emits significant amounts of gamma radiation in addition to its 511 keV annihilation photons, so radiation safety is a significant issue with this PET radionuclide. Much study and care is applied to radiation dosimetry for patients receiving injected radiopharmaceuticals and to limiting exposure for the clinical personnel that administer these doses as a full-time job. However, it is also important to monitor and limit radiation dose to personnel responsible for the production of radionuclides and radiopharmaceuticals, especially since they are likely handling more radioactivity before some of it is lost to nuclear decay and yield losses from chemical processes. Automated modules are very useful in this respect, both for isolating radionuclides and synthesis of radiolabelled compounds, because they can be located inside a hot cell of any size and thickness necessary to protect personnel. The module that has been designed for the chemical isolation of ^{52}Mn will play an important role in making this valuable PET radionuclide widely available by enabling routine, scaled-up productions of much larger activities than would otherwise be reasonable to handle by hand in an open laboratory benchtop setting, even inside of a lead castle. Based on general experience with

automated modules for chemical separations of PET radiometals, it is also possible that using such a module for isolating ^{52}Mn in a hot cell could result in greater purity and consistency by reducing the influence of human factors and protecting the isolation procedure from environmental contaminants.

5.5. Conclusions and Recommendations

- Semi-automated modules for the scaled-up production of ^{89}Zr and ^{86}Y were constructed in collaboration with a team of people. These automated modules were able to carry out separations inside of a lead hot cell by moving solvents through tubing by vacuum or compressed air. The separation process was controlled from outside the hot cell by a laptop that was connected to the module and running a software program that was produced in-house. The ability to control separation processes remotely protects production personnel from significant radiation dose, and these modules have been used routinely to produce isotopes for use at institutions nationwide, including ^{89}Zr for a clinical trial at our institution.
- We have designed a similar module that will implement the anion-exchange separation method for ^{52}Mn from a chromium metal target.
- *Recommended future directions:* For the ^{52}Mn automated module: assemble the module; automate with a custom software program; validate the module with increasing starting activities until it is ready for routine use; if collecting the final ^{52}Mn product in the same glass vessel as the previous rounds

introduces contaminants in the final product, then a separate line and collection vessel for the final round of elution of ^{52}Mn can be added to the design.

5.6. References

- Anderson, C.J.; Welch, M.J., 1999. Radiometal labeled agents (non-technetium) for diagnostic imaging. *Chem. Rev.* 99, 2219-2234.
- Avila-Rodriguez, M.A.; Nye, J.A.; Nickles, R.J., 2008. Production and separation of non-carrier-added ^{86}Y from enriched ^{86}Sr targets. *Appl. Radiat. Isot.* 66, 9-13.
- Birattari, C.; Gadloli, E.; Erba, E.G.; Strini, A.M.G.; Strini, G., et al., 1973. Pre-equilibrium processes in (p,n) reactions. *Nuclear Physics A* 201, 579-592.
- Blosser, H.; Handley, T., 1955. Survey of (p,n) Reactions at 12 Mev. *Physical Review* 100, 1340-1344.
- Burke, P.; Golovko, O.; Clark, J.C.; Aigbirhio, F.I., 2010. An automated method for regular productions of copper-64 for PET radiopharmaceuticals. *Inorganica Chimica Acta* 363, 1316-1319.
- Chattopadhyay, S.; Barua, L.; De, A.; Das, S.S.; Kuniyil, R., et al., 2012. A computerized compact module for separation of Tc-99m-radionuclide from molybdenum. *Appl. Radiat. Isot.* 70, 2631-2637.
- Church, L.B.; Caretto, A.A., 1969. Study of (P,Xn) Reactions at 400-Mev. *Physical Review* 178, 1732-1742.
- Dejesus, O.T.; Nickles, R.J., 1990. Production and Purification of Zr-89, a Potential Pet Antibody Label. *Appl. Radiat. Isot.* 41, 789-790.
- Deri, M.A.; Zeglis, B.M.; Francesconi, L.C.; Lewis, J.S., 2013. PET imaging with (8)(9)Zr: from radiochemistry to the clinic. *Nuclear medicine and biology* 40, 3-14.
- Disselhorst, J.A.; Brom, M.; Laverman, P.; Slump, C.H.; Boerman, O.C., et al., 2010. Image-quality assessment for several positron emitters using the NEMA NU 4-2008 standards in the Siemens Inveon small-animal PET scanner. *Journal of nuclear medicine* 51, 610-617.
- Dutta, B.; Maiti, M.; Lahiri, S., 2009. Production of $^{88,89}\text{Zr}$ by proton induced activation of natY and separation by SLX and LLX. *Journal of Radioanalytical and Nuclear Chemistry* 281, 663-667.
- Edraw Max software. EdrawSoft, Sheung Wan, Hong Kong. Online: <<https://www.edrawsoft.com/EDrawMax.php>>.
- Ehmann, W.D.; Vance, D.E., 1991. *Radiochemistry and Nuclear Methods of Analysis*. Wiley, New York.
- Evaluated Nuclear Structure Data File (ENSDF), National Nuclear Data Center (NNDC), Brookhaven National Laboratory (BNL). Online database accessed via: <<http://www.nndc.bnl.gov/chart/>>.

- Fadeeva, V.I.; Tikhomirova, T.I.; Yuferova, I.B.; Kudryavtsev, G.V., 1989. Preparation, Properties and Analytical Application of Silica with Chemically Grafted Hydroxamic Acid Groups. *Anal. Chim. Acta* 219, 201-212.
- Greenwood, N.N.; Earnshaw, A., 1997. *Chemistry of the Elements*, 2nd ed. Butterworth-Heinemann, Oxford, United Kingdom.
- Herscheid, J.D.M.; Vos, C.M.; Hoekstra, A., 1983. Manganese-52m for Direct Application - a New Fe-52/Mn-52m Generator Based on a Hydroxamate Resin. *International Journal of Applied Radiation and Isotopes* 34, 883-886.
- Holland, J.P.; Sheh, Y.; Lewis, J.S., 2009. Standardized methods for the production of high specific-activity zirconium-89. *Nucl. Med. Biol.* 36, 729-739.
- Ikotun, O.F.; Lapi, S.E., 2011. The rise of metal radionuclides in medical imaging: copper-64, zirconium-89 and yttrium-86. *Future Med. Chem.* 3, 599-621.
- Kandil, S.A.; Scholten, B.; Saleh, Z.A.; Youssef, A.M.; Qaim, S.M., et al., 2008. A comparative study on the separation of radiozirconium via ion-exchange and solvent extraction techniques, with particular reference to the production of ⁸⁸Zr and ⁸⁹Zr in proton induced reactions on yttrium. *Journal of Radioanalytical and Nuclear Chemistry* 274, 45-52.
- Kasbollah, A.; Eu, P.; Cowell, S.; Deb, P., 2013. Review on production of ⁸⁹Zr in a medical cyclotron for PET radiopharmaceuticals. *Journal of nuclear medicine technology* 41, 35-41.
- Khandaker, M.U.; Kim, K.; Lee, M.W.; Kim, K.S.; Kim, G., et al., 2012. Investigations of Y-89(p,x)Zr-86, Zr-88, Zr-89g, Y-86m+g, Y-87g, Y-87m, Y-88g, Sr-85g, and Rb-84g nuclear processes up to 42 MeV. *Nucl. Instrum. Methods Phys. Res. B* 271, 72-81.
- Kume, M.; Carey, P.C.; Gaehle, G.; Madrid, E.; Voller, T., et al., 2012. A semi-automated system for the routine production of copper-64. *Applied radiation and isotopes* 70, 1803-1806.
- Lahiri, S.; Mukhopadhyay, B.; Das, N.R., 1997. Simultaneous production of Zr-89 and Nb-90, Nb-91m, Nb-92m in alpha-particle activated yttrium and their subsequent separation by HDEHP. *Appl. Radiat. Isot.* 48, 883-886.
- Link, J.; Krohn, K.; Eary, J.; Kishore, R.; Lewellen, T., et al., 1986. ⁸⁹Zr for antibody labeling and positron emission tomography. *J. Labelled Comp. Radiopharm.* Sixth International symposium on radiopharmaceutical chemistry. Wiley, Boston, pp. 1297-1298.
- Madrid, E.; Carey, P.; Kume, M.; Welch, M.; Lapi, S., 2011. Optimization of Y-86 production via an automated system, *J. Nucl. Med. Meeting Abstracts*, p. 1437. Society of Nuclear Medicine Annual Meeting, San Antonio, Texas, United States, 4-8 Jun. 2011.
- Matarrese, M.; Bedeschi, P.; Scardaoni, R.; Sudati, F.; Savi, A., et al., 2010. Automated production of copper radioisotopes and preparation of high specific activity [(64)Cu]Cu-ATSM for PET studies. *Applied radiation and isotopes* 68, 5-13.
- McCabe, K.E.; Wu, A.M., 2010. Positive progress in immunoPET--not just a coincidence. *Cancer biotherapy & radiopharmaceuticals* 25, 253-261.
- Meijs, W.E.; Herscheid, J.D.M.; Haisma, H.J.; Pinedo, H.M., 1992. Evaluation of Desferal as a Bifunctional Chelating Agent for Labeling Antibodies with Zr-89. *Appl. Radiat. Isot.* 43, 1443-1447.

- Meijs, W.E.; Herscheid, J.D.M.; Haisma, H.J.; Wijbrandts, R.; van Langevelde, F., et al., 1994. Production of Highly Pure No-Carrier Added ^{89}Zr for the Labeling of Antibodies with a Positron Emitter. *Appl. Radiat. Isot.* 45, 1143-1147.
- Michel, R.; Bodemann, R.; Busemann, H.; Daunke, R.; Gloris, M., et al., 1997. Cross sections for the production of residual nuclides by low- and medium-energy protons from the target elements C, N, O, Mg, Al, Si, Ca, Ti, V, Mn, Fe, Co, Ni, Cu, Sr, Y, Zr, Nb, Ba and Au. *Nucl. Instrum. Methods Phys. Res. B* 129, 153-193.
- Nagatsu, K.; Fukada, M.; Minegishi, K.; Suzuki, H.; Fukumura, T., et al., 2011. Fully automated production of iodine-124 using a vertical beam. *Appl. Radiat. Isot.* 69, 146-157.
- National Nuclear Data Center (NNDC), Brookhaven National Laboratory (BNL). Cross-Section Information Storage and Retrieval System (CSISRS). Data from: International Network of Nuclear Reaction Data Centres (NRDC). Online database: <<http://www.nndc.bnl.gov/exfor/exfor.htm>>. Plots generated by the X4-Servlet.
- Nayak, T.K.; Brechbiel, M.W., 2009. Radioimmunoimaging with longer-lived positron-emitting radionuclides: potentials and challenges. *Bioconjugate chemistry* 20, 825-841.
- Otuka, N.; Dupont, E.; Semkova, V.; Pritychenko, B.; Blokhin, A.I., et al., 2014. Towards a More Complete and Accurate Experimental Nuclear Reaction Data Library (EXFOR): International Collaboration Between Nuclear Reaction Data Centres (NRDC). *Nuclear Data Sheets* 120, 272-276.
- Park, L.S.; Szajek, L.P.; Wong, K.J.; Plascjak, P.S.; Garmestani, K., et al., 2004. Semi-automated ^{86}Y purification using a three-column system. *Nuclear medicine and biology* 31, 297-301.
- Saha, G.B.; Porile, N.T.; Yaffe, L., 1966. (P,Xn) and (P,Pxn) Reactions of Yttrium-89 with 5-85-Mev Protons. *Physical Review* 144, 962-971.
- Siikanen, J.; Peterson, M.; Tran, T.A.; Roos, P.; Ohlsson, T., et al., 2012. A peristaltic pump driven ^{89}Zr separation module. *AIP Conf. Proc.* 1509, 206-210. 14th International Workshop on Targetry and Target Chemistry, Playa del Carmen, Mexico, 26-29 Aug. 2012.
- Smith, D.S.; Stabin, M.G., 2012. Exposure rate constants and lead shielding values for over 1,100 radionuclides. *Health phys.* 102, 271-291.
- Uddin, M.S.; Hagiwara, M.; Baba, M.; Tarkanyi, F.; Ditroi, F., 2005. Experimental studies on excitation functions of the proton-induced activation reactions on yttrium. *Appl. Radiat. Isot.* 63, 367-374.
- van Dongen, G.A.; Visser, G.W.; Lub-de Hooge, M.N.; de Vries, E.G.; Perk, L.R., 2007. Immuno-PET: a navigator in monoclonal antibody development and applications. *Oncologist* 12, 1379-1389.
- van Dongen, G.A.; Vosjan, M.J., 2010. Immuno-positron emission tomography: shedding light on clinical antibody therapy. *Cancer Biother. Radiopharm.* 25, 375-385.
- Verel, I.; Visser, G.W.; Boellaard, R.; Stigter-van Walsum, M.; Snow, G.B., et al., 2003. ^{89}Zr immuno-PET: comprehensive procedures for the production of ^{89}Zr -labeled monoclonal antibodies. *Journal of nuclear medicine* 44, 1271-1281.
- Verel, I.; Visser, G.W.M.; van Dongen, G.A., 2005. The promise of immuno-PET in radioimmunotherapy. *Journal of Nuclear Medicine* 46 (Suppl. 1), 164S-171S.
- Vugts, D.J.; Visser, G.W.; van Dongen, G.A., 2013. ^{89}Zr -PET radiochemistry in the development and application of therapeutic monoclonal antibodies and other biologicals. *Current topics in medicinal chemistry* 13, 446-457.

- Wadas, T.J.; Wong, E.H.; Weisman, G.R.; Anderson, C.J., 2010. Coordinating radiometals of copper, gallium, indium, yttrium, and zirconium for PET and SPECT imaging of disease. *Chemical reviews* 110, 2858-2902.
- Walther, M.; Gebhardt, P.; Grosse-Gehling, P.; Wurbach, L.; Irmeler, I., et al., 2011. Implementation of ^{89}Zr production and in vivo imaging of B-cells in mice with ^{89}Zr -labeled anti-B-cell antibodies by small animal PET/CT. *Applied radiation and isotopes* 69, 852-857.
- Welch, M.J.; Tang, L.L.W.; Gaehle, G.G.; Lewis, J.S., 2006. AUTOMATED SEPARATION, PURIFICATION AND LABELING SYSTEM FOR ^{60}Cu , ^{61}Cu AND ^{64}Cu RADIONUCLIDES AND RECOVERY THEREOF. United States patent no.: US 2006/0004491 A1. Other patents: EP1654206A2, EP1654206A4, WO2005014510A2, WO2005014510A3.
- Wooten, A.L.; Madrid, E.; Schweitzer, G.D.; Lawrence, L.A.; Mebrahtu, E., et al., 2013. Routine Production of ^{89}Zr Using an Automated Module. *Appl. Sci.* 3, 593-613.
- Wooten, A.L.; Schweitzer, G.D.; Lawrence, L.A.; Madrid, E.; Lapi, S.E., 2012. An automated system for production of ^{89}Zr . *AIP Conf. Proc.* 1509, 201-205. 14th International Workshop on Targetry and Target Chemistry, Playa del Carmen, Mexico, 26-29 Aug. 2012.
- Zerkin, V., IAEA-NDS. Multi-platform EXFOR-CINDA-ENDF. Project dates: 1999-2015.
- Ziegler, J.F.; Ziegler, M.D.; Biersack, J.P., 2010. SRIM - The stopping and range of ions in matter (2010). *Nucl. Instrum. Methods Phys. Res. B* 268, 1818-1823.
- Zweit, J.; Downey, S.; Sharma, H.L., 1991. Production of No-Carrier-Added Zirconium-89 for Positron Emission Tomography. *Appl. Radiat. Isot.* 42, 199-201.

Chapter 6. Compiled Conclusions and Recommendations

This dissertation has included concepts and results from applications for positron-emitting radiometals, with an emphasis on ^{52}Mn . These experiments have centered around the larger ideas that have defined the chapters of this dissertation: radionuclide production and isolation, biodistribution and PET imaging, applications in PET/MR, and automation for scaled-up radionuclide production. The conclusions and recommended future directions for each of these ideas can be found at the end of each respective chapter, and they are summarized here:

Chapter 1. Introduction

- Manganese is important because of its natural role as an essential micronutrient in humans that is involved in several important processes for life.
- Manganese has historically caused neurotoxicity when inhaled chronically from environmental contaminants, and occupational exposure to inhaled manganese continues to cause neurotoxicity, even in developed countries with occupational safety measures.
- Manganese(II) is one of the most highly paramagnetic cations on the periodic table, which makes it a candidate for the metallic core in T_1 contrast agents. Manganese(II) has very different chemistry, toxicity, and excretion route than the current standard cation Gd(III), so Mn(II) provides a meaningful alternative.

- A radiotracer for the study of manganese is important because of the sensitivity of many radioactive assays, the ease of quantification, and the availability of necessary equipment. *In vivo* imaging of manganese is also important for studying the above roles of manganese, and PET imaging has advantages over other nuclear emission imaging modalities (and the lack of a SPECT radioisotope of manganese).
- Manganese-52 was selected because it is a positron-emitter with a sufficient total intensity of positrons, a relatively long half-life for nuclear decay that would enable studies spanning several days, and the ability to produce ^{52}Mn from a non-enriched target bombarded with low-energy protons, which were available from a cyclotron at our institution. Manganese-52 is a good choice for studying manganese specifically, but and also has characteristics that make it competitive with other PET radiometals, such as a very low average positron energy, which can correspond to good spatial resolution in PET.

Chapter 2. Nuclear Cross-Sections and Chemical Separation of ^{52}Mn

- Nuclear cross-sections have been measured for the $^{\text{nat}}\text{Cr}(p,x)^{52,52\text{m},54}\text{Mn}$ reactions for incident protons with energy ≤ 13 MeV, which is easily achieved by most cyclotrons at medical centers. The cross-section results agreed closely with theoretical simulations, and they can be used to predict yields of $^{52,52\text{m},54}\text{Mn}$ when bombarding natural chromium with low-energy protons.

- Chemical isolation was performed using a published method that involved digesting the chromium target in HCl, replacing the HCl with dilute H₂SO₄ and then immobilizing ⁵²Mn(II) on a cation-exchange column. This method resulted with visible amounts of Cr(III) in the product.
- Chemical isolation using a recently published method was more effective. This method involved digesting the chromium target in HCl, diluting this solution in ethanol, immobilizing ⁵²Mn(II) on an anion-exchange column, and performing this process repeatedly.
- *Recommended future directions:* Trace metal analysis after each round of the anion-exchange separation method to determine how many rounds are necessary; characterization of routine production including cyclotron yields, chemical recovery percentage, radionuclidic purity, and trace metals analysis.

Chapter 3. Biodistribution and PET Imaging of ⁵²Mn

- Biodistribution studies of intravenously injected ⁵²Mn(II) in mice showed uptake in many organs, most interestingly: salivary glands, brain, thyroid, thymus, pancreas, liver, kidney, and bone.
- Similar studies in rats that extended to longer timepoints showed that activity in all of those organs decreases significantly over the course of seven days, except for brain, adrenals, and pancreas and confirmed that manganese is excreted almost exclusively through the feces and not the urine.
- Biodistribution studies of inhaled manganese in mice showed uptake in lung, brain, thyroid, pancreas, liver, and kidney.

- PET imaging of [^{52}Mn]MnCl₂ in mice and rats confirmed the observations from biodistribution, including high signal from ^{52}Mn in the pancreas at seven days post-injection, after the activity had significantly decreased in nearby tissues, such as the liver and kidneys.
- *Recommended future directions:* PET/CT imaging using a CT contrast agent that will reveal the pancreas on CT, which will enable quantitative imaging of free manganese in the pancreas with possible applications in diagnostic imaging of diabetes.

Chapter 4. Applications for ^{52}Mn in PET/MR Imaging

- A phantom containing various concentrations of non-radioactive Mn(II)Cl₂·(H₂O)₄ dissolved in water, was imaged by MRI using an inversion recovery pulse sequence. The signal from the images were analyzed, and these results were used to calculate the relaxivity of this compound in aqueous solution.
- Another phantom was constructed that contained a matrix of different concentrations of non-radioactive Mn(II)Cl₂·(H₂O)₄ dissolved in water to which different amounts of ^{52}Mn had been added. This phantom was imaged by PET/MR and revealed changes in both MR and PET signals.
- *Recommended future directions:* Investigate the utility of ^{52}Mn by radiolabeling a compound that has been used to chelate Mn(II) for MRI imaging; perform PET/MR imaging of phantoms containing the compound

complexed with non-radioactive Mn(II) and radioactive $^{52}\text{Mn(II)}$ in various concentrations and radioactivities.

Chapter 5. Remotely-Controlled Modules for the Isolation of PET Radiometals

- Semi-automated modules for the scaled-up production of ^{89}Zr and ^{86}Y were constructed in collaboration with a team of people. These automated modules were able to carry out separations inside of a lead hot cell by moving solvents through tubing by vacuum or compressed air. The separation process was controlled from outside the hot cell by a laptop that was connected to the module and running a software program that was produced in-house. The ability to control separation processes remotely protects production personnel from significant radiation dose, and these modules have been used routinely to produce isotopes for use at institutions nationwide, including ^{89}Zr for a clinical trial at our institution.
- We have designed a similar module that will implement the anion-exchange separation method for ^{52}Mn from a chromium metal target.
- *Recommended future directions:* For the ^{52}Mn automated module: assemble the module; automate with a custom software program; validate the module with increasing starting activities until it is ready for routine use; if collecting the final ^{52}Mn product in the same glass vessel as the previous rounds introduces contaminants in the final product, then a separate line and collection vessel for the final round of elution of ^{52}Mn can be added to the design.

This dissertation has presented preliminary work in the production and biomedical applications of ^{52}Mn , a radionuclide that holds potential for many more studies related to PET imaging and non-imaging of the behavior of manganese.

Appendix A. Calibration Setting Numbers
for Selected PET Radioisotopes in Ionization
Dose Calibrators

Table of Contents

A.1. Introduction	2
A.2. Experimental.....	5
A.3. Results	11
A.4. Discussion.....	14
A.5. Conclusions and Recommendations	16
A.6. References	16

List of Figures

Figure A.1. Plots of normalized readout radioactivity (ARO,norm) versus calibration setting numbers (NA) over large ranges of settings.	14
--	----

List of Tables

Table A.1. Summary of isotope production methods that were followed or adapted for the isotopes used in this work.....	6
Table A.2. Shared characteristics of the CRC-15R and CRC-25R models of Capintec brand ionization dose calibrators.....	9
Table A.3. Results for calibration setting numbers on Capintec CRC-15R and CRC-25R dose calibrators.....	12
Table A.4. Selected results from other studies that determined setting numbers for various medical radionuclides and models of Capintec dose calibrators.	13

Appendix A. Calibration Setting Numbers **for Selected PET Radioisotopes in** **Ionization Dose Calibrators**^{1,2,3,4}

For PET radionuclides, the radioactivity of a sample can be conveniently measured by a dose calibrator. These devices depend on a “calibration setting number”, but many recommended settings from manuals were interpolated based on standard sources of other radionuclide(s). We

¹ Much of the work in this appendix is being revised for publication elsewhere:

Wooten, A.L.; Lewis, B.C.; Szatkowski, D.J.; Sultan, D.H.; Abdin, K.I.; Voller, T.F.; Liu, Y.; Lapi, S.E. Calibration Setting Numbers for Dose Calibrators for the PET Isotopes ⁵²Mn, ⁶⁴Cu, ⁷⁶Br, ⁸⁶Y, ⁸⁹Zr, ¹²⁴I. In revision.

² A.L. Wooten contributed to: experimental design, experimental measurements, data analysis, preparation of figures and tables, and writing.

³ Acknowledgments: The authors mentioned in the manuscript above contributed to the work presented in this chapter, especially B.C.L. and D.J.S. who contributed to experimental design, experimental measurements, and data analysis. B.C.L. also performed much of the literature research. The authors additionally acknowledge T.E. Mastren (WUSTL/WUSM/MIR) and D.R. Mayo (Los Alamos National Laboratory, New Mexico, United States) for helpful advice; A. Hall (Capintec) for helpful advice and providing useful materials; W.H. Margenau and P.M. Margenau (WUSM/MIR) for operation of the cyclotron; E. Madrid, E. Mebrahtu, and P.E. Eisenbeis (WUSM/MIR) for their roles in radioisotope production.

⁴ A.L.W. was supported in part by a training grant from the National Institute of Biomedical Imaging and Bioengineering, U.S. National Institutes of Health (1T32EB14855-01). The authors have no competing financial interests to disclose. B.C.L., A.L.W., and other costs were supported in part or in whole by the Nuclear Science and Security Consortium (NSSC) multi-institutional training grant from the Office of Nonproliferation and Verification Research and Development, National Nuclear Security Administration (NNSA), United States Department of Energy (US DOE) (DE-NA0000979). There was no project-specific funding for this project.

Disclaimer: “This report was prepared as an account of work sponsored by an agency of the United States Government. Neither the United States Government nor any agency thereof, nor any of their employees, makes any warranty, express or limited, or assumes any legal liability or responsibility for the accuracy, completeness, or usefulness of any information, apparatus, product, or process disclosed, or represents that its use would not infringe privately owned rights. Reference herein to any specific commercial product, process, or service by trade name, trademark, manufacturer, or otherwise does not necessarily constitute or imply its endorsement, recommendation, or favoring by the United States Government or any agency thereof. The views and opinions of authors expressed herein do not necessarily state or reflect those of the United States Government or any agency thereof.”

conducted HPGe gamma-ray spectroscopy, resulting in a reference for determining settings in two types of vessels containing one of several PET radionuclides. Our results reiterate the notion that in-house, experimental calibrations are recommended for different radionuclides and vessels.

A.1. Introduction

Many PET imaging agents that are currently in development, including peptides, antibodies, and nanoparticles, have biological half-lives of hours to days, so they require positron-emitting radiolabels with longer half-lives than traditional PET isotopes, such as ^{11}C or ^{18}F . Other isotopes such as ^{64}Cu , ^{86}Y , ^{89}Zr , and ^{124}I , satisfy these criteria and are currently used as radiolabels for compounds in preclinical and clinical research (Ikotun and Lapi, 2011; Nayak and Brechbiel, 2009; Wadas et al., 2010). For studies using any of these isotopes, it is critical to obtain accurate measurements of radioactivity at numerous stages of the PET study, including: immediately following target irradiation, chemical separation, dispensing, radiolabelling, and pre-injection. These radioactivity measurements are commonly measured in laboratory and clinical settings using a dose calibrator, which provides fast results for the measurement of the radioactivity of a sample. This type of benchtop instrument has a small enough footprint and a small enough cost to be commonly installed in many different rooms that might be used during the workflow from cyclotron to injection.

The user manuals provided by Capintec (2007, 2015) for the dose calibrators that were used in this investigation provided a good explanation of the physics of radiation measurement that are employed by these models of gas ionization dose calibrators. We only briefly summarize these explanations here. Dose calibrators measure the radioactivity of a sample based on the rate

at which it emits ionizing photon radiation—X-rays, gamma-rays, or other photons (e.g., from positron annihilation). With a few exceptions, particle radiation—alphas, betas, and positrons—are not penetrating enough to cause ionization in the gas chamber. In many models of dose calibrators, the radioactive sample is lowered into the center of a cylindrical sealed chamber containing a gas. Photons in the 100-2,000 keV energy range do not directly produce the ionization signal for the dose calibrator, but rather they interact with the wall and/or gas of the chamber to release electrons, and these secondary electrons ionize the gas in the chamber enough to produce the electric signal that is measured by the device. Electric current is created in a circuit within the dose calibrator, and the magnitude of this current is directly proportional to the radioactivity of the isotope that emitted the radiation (for similar sample geometries). In the dose calibrators used in this investigation, the gas in the chamber was argon, which is also used in many other gas ionization dose calibrators.

Since the radiation dose rates vary widely by isotope, the accuracy of these instruments relies on using the correct calibration setting for the isotope being measured. For ionization chambers connected to older, analog control units, a dial setting adjusts a potentiometer to change the gain in the detector for the isotope being measured (IAEA). In newer, digital dose calibrators, a “calibration setting number” (represented by the variable N_A in certain user manuals) simply adjusts the digital output of the unit (Capintec, 2007, 2015; Chandra, 2011). In both generations of dose calibrators, numerous commonly used isotopes have pre-programmed settings that can be selected, but a custom calibration setting number must be entered (or dialed) for other isotopes. Many calibration setting numbers are recommended by Capintec in user manuals, but the vast majority of these values were calculated using an empirical linear fit equation that was based upon the detector response to only two isotopes in a single geometry

(Capintec, 2007, 2015). Specifically, these measurements were conducted for reference sources consisting of 5 mL of solution containing ^{57}Co or ^{60}Co in a glass ampoule with 0.6 mm wall thickness, obtained from the United States National Institute of Standards and Technology (NIST) (NIST, 2011; Capintec, 2007, 2015).

Consequently, several publications have endeavored to experimentally determine new calibration setting numbers for various models of Capintec dose calibrators, sample geometries, and radionuclides. To measure reference activities, these investigations have used various radioanalytical techniques: HPGe detector (Beattie et al., 2014; Coursey et al., 1993; Zimmerman et al., 2001), NaI(Tl) detector (Zimmerman et al., 2002), $4\pi\beta$ liquid scintillation ($4\pi\beta$ -LS) (Cessna et al., 2008; Mo et al., 2006; Zimmerman and Cessna, 2000; Zimmerman et al., 1999), or a different gas ionization chamber (Tyler and Woods, 2002, 2003). Some of the calibration setting numbers that were determined in these studies yielded radioactivity readouts that were dramatically different from the radioactivity readout from recommended settings. In at least one case, Capintec officially changed its recommended calibration for an isotope: Based on the results of Zimmerman, *et al.* (2001) and later Cessna, *et al.* (2008), the recommended setting number for ^{18}F was changed from 439 to 472 for NIST ampoules and 484 for 3 mL plastic syringes (Capintec, 2009). Furthermore, the calibration setting numbers for the same isotopes in the same dose calibrator models were often greater for samples with larger volumes. Geometry effects are even more pronounced for isotopes that emit low-energy gamma-rays (Tyler and Woods, 2003); or positrons or beta particles (Capintec, 2007, 2015) because these radiations are more susceptible to systematic errors resulting from attenuation or scattering, respectively.

We acknowledge that some facilities in radiochemistry and nuclear medicine may rely solely on Capintec dose calibrators to measure radioactivity—without access to a high-precision

reference measurement instrument, such as a HPGe detector. In Section A.2.3, we performed gamma-ray spectroscopy using a HPGe detector to quantify the amount of radioactivity in samples that served as references for the experimental determination of calibration setting numbers for two different sample geometries containing the PET isotopes ^{52}Mn , ^{64}Cu , ^{86}Y , ^{89}Zr , ^{76}Br and ^{124}I . The two geometries that we tested were 2 mL microcentrifuge tubes, which are widely measured in dose calibrators for radiochemistry work, and 10 cc (10 mL) syringes, which are commonly measured in dose calibrators before injection of a radiopharmaceutical.

A.2. Experimental

A.2.1. Materials

Ultrapure water ($\sim 18\text{ M}\Omega$) was obtained from a Millipore system (Billerica, Massachusetts, United States) and was used for diluting aliquots of radioactivity. 2 mL microcentrifuge tubes and 10 cc syringes were purchased from Fisher Scientific (Pittsburgh, Pennsylvania, United States). All ^{124}I was purchased from 3D Imaging (Maumelle, Arkansas, United States).

A.2.2. Radionuclide Production

All other isotopes used in this work were produced on-site by (p,n) reactions in solid targets that were bombarded with protons from the CS-15 cyclotron (The Cyclotron Corporation, Berkeley, California, United States) at Washington University School of Medicine in St. Louis (WUSM). Various methods (Table A.1) were carried out by remotely-controlled automated

modules inside of lead hot cells to separate the following isotope products from the corresponding bulk solid target material: ^{64}Cu (Kume et al., 2012; McCarthy et al., 1997), ^{76}Br (McCarthy et al., 1999; Tolmachev et al., 1998), ^{86}Y (Avila-Rodriguez et al., 2008; Yoo et al., 2005), and ^{89}Zr (Holland et al., 2009; Meijs et al., 1994; Wooten et al., 2012). Manganese-52 was produced by bombarding a natural Cr foil target with protons (Wooten et al., 2015), followed by digesting the Cr foil in hydrochloric acid with no further purification. Iodine-124 was produced by 3D Imaging (Berridge, 2013) in a manner similar to methods that were published by Knust, *et al.* (2000), Sheh, *et al.* (2000), and other published methods. For each isotope, aliquots were taken and diluted with ultrapure water as needed for gamma-ray spectroscopy (Section A.2.3) or dose calibrator measurements (Section A.2.4).

Table A.1. Summary of isotope production methods that were followed or adapted for the isotopes used in this work.

Product Isotope	Target		Isolation Method	Reference(s)
	Isotope	Material		
^{52}Mn	^{52}Cr (83.7%)	$^{\text{nat}}\text{Cr}$ metal foil	(No isolation performed—only digestion of Cr target by HCl.)	-
^{64}Cu	^{64}Ni (0.9%)	Electroplated ^{64}Cu metal	Anion-exchange chromatography	<u>AM</u> : (Kume, et al., 2012) <u>SC</u> : (McCarthy et al., 1997)
^{76}Br	^{76}Se (9.4%)	Pressed $^{76}\text{Cu}_2\text{Se}$ pellet	Dry distillation followed by thermal chromatography	<u>AM</u> : Not yet published. <u>SC</u> : (McCarthy, et al., 1999) (Tolmachev, et al., 1998)
^{86}Y	^{86}Sr (9.9%)	Pressed ^{86}SrO pellet	pH-based precipitation followed by filtration	<u>AM</u> : Not yet published. <u>SC</u> : (Avila-Rodriguez, et al., 2008) (Yoo, et al., 2005)
^{89}Zr	^{89}Y (100%)	$^{\text{nat}}\text{Y}$ metal foil	Hydroxamate resin chromatography	<u>AM</u> : (Wooten, et al., 2012) <u>SC</u> : (Holland, et al., 2009) (Meijs, et al., 1994)
$^{124}\text{I}^\dagger$	^{124}Te (4.7%)	$\text{TeO}_2/\text{Al}_2\text{O}_3$	Dry distillation	<u>SC</u> : (Knust, et al., 2000) (Sheh, et al., 2000)

All isotopes were produced via (p,n) reactions. † Purchased from 3D Imaging (Maumelle, Arkansas, United States). All other isotopes were produced in-house at WUSM/MIR. AM: automated module; SC: separation chemistry.

A.2.3. Gamma-Ray Spectroscopy

The radioactivity per volume of the product solution was calculated based on gamma-ray spectroscopy results from one of two Canberra (Meriden, Connecticut, United States) brand HPGe detector systems: Detector 1 (model GC1818 with 18.9% efficiency) and Detector 2 (model GC2018 with 24.5% efficiency) . Each detector was connected to a digital spectrum analyzer (DSA; model: DSA-1000) and operated by the *Gamma Acquisition & Analysis* module of the *Genie 2000* spectroscopy software package (v. 3.3). The HPGe detector was calibrated for energy and efficiency based on the full-absorption photopeaks from a mixed-gamma reference source (Eckert & Ziegler Analytics, Atlanta, Georgia, United States). This calibration source consisted of a 2 mL skirted microcentrifuge tube that contained eight radioisotopes in a hardened epoxy, which was an identical geometry to the 2 mL microcentrifuge tubes used for counting emissions from our diluted isotope products.

For each isotope considered in this study, an aqueous solution containing the isotope was serially diluted in 2 mL microcentrifuge tubes until the Ge detector yielded a dead time <5%. The dilution was produced in triplicate, and each of these three tubes was scanned long enough to acquire $\geq 10^3$ counts for the gamma-ray with the highest branching ratio, which was typically 10-30 min of detector live time. In the spectroscopy results, we identified at least one full-absorption photopeak that corresponded to an identifying gamma-ray energy (E_γ) that was emitted by the isotope being measured. Gamma-ray energy(ies) with the highest branching ratio(s) without also being emitted by a metastable isomer (e.g., $E_\gamma=1,434$ keV from ^{52m}Mn) were used for analysis. The number of counts and detector efficiency for the selected peak were used to calculate the radioactivity per volume, assuming no decay during counting because the counting period was short (<5%) relative to the isotope's half-life using the following equation:

$$A = \frac{N_c}{\varepsilon_c I_\gamma t_l}, \quad (\text{A.1})$$

where A is the radioactivity (Bq); N_c is the number of counts (net peak area) for the full-absorption photopeak; ε_c is the counting efficiency for the detector at the corresponding gamma-ray energy (dimensionless); I_γ is the branching ratio for the corresponding gamma-ray (dimensionless); t_l is the detector live time during gamma-ray counting. The results calculated using Equation A.1 were decay-corrected to an arbitrary time in the past for all three tubes, averaged together, and then multiplied by the dilution factor to determine the radioactivity per volume of the original product solution at that common time. This value was then used to calculate the radioactivity per volume in the product solution at the time when the samples would be prepared for the dose calibrator measurement (Section A.2.4).

A.2.4. Dose Calibrator Measurements

Calibration setting numbers were determined from measurements using two models of dose calibrators from Capintec (Ramsey, New Jersey, United States): a model CRC-15R or a model CRC-25R. Characteristics of both of these models are given in Table A.2, and they use identical calibration setting numbers (Capintec, 2007, 2009, 2015). For each isotope, one radioactivity between 10-1,000 μCi was selected for measurement in a dose calibrator. Based on the radioactivity per volume calculated from the gamma-ray spectroscopy results, the radioactivity was decay-corrected to the approximate time of measurement in the dose calibrator. Then, the appropriate volume containing the radioactivity was transferred into either a 2 mL microcentrifuge tube or into a 10 cc syringe. The final volume in these vessels was

approximately 1 or 8 mL, respectively. The time from pipetting to the end of the final measurement in the dose calibrator was less than 15 min., so decay during that period was negligible for the isotopes studies.

Table A.2. Shared characteristics of the CRC-15R and CRC-25R models of Capintec brand ionization dose calibrators.

Well Diameter	6.1 cm
Well Depth	25.4 cm
Electrometer Accuracy	Better than $\pm 2\%$
System Precision	Better than $\pm 0.1\%$ FSD
System Linearity	Within $\pm 2\%$
Equation for recommended calibration numbers	$N_A = 1076*(R_A - 0.080)$

N_A =Calibration number; R_A =the response of the detector to Isotope A. (Sources: Capintec, 2007, 2015).

Each sample was placed in the dose calibrator, and the calibration setting number was adjusted until the screen displayed the expected radioactivity based on the gamma spectroscopy results (corrected for dilution and radioactive decay). During these measurements, the precision of the dose calibrator was set to read to the nearest 1 μCi . For some isotopes that emitted high or low dose rates of gamma radiation, it was necessary to find a calibration setting number that caused the control unit to display a multiple of the expected value so divisions or multiplication of the readout by an integer correction factor obtained a meaningful result. When using these dial settings to measure an unknown amount of radioactivity, the readout value would be divided or multiplied by the correction factor for that isotope, such as $\div 2$, $\times 2$, $\times 10$, and $\times 100$, to yield the final radioactivity readout (A_{RO}). For some of our experiments, the sample was removed from the dose calibrator and replaced in a different orientation to account for variations in the positioning of the vessel within the well of the dose calibrator. For these experiments where only one valid setting was recorded, we conservatively assumed an uncertainty of ± 5 setting numbers to

manufacture a range of values. Additionally, for ^{52}Mn , ^{64}Cu , and ^{124}I , the calibration setting number was varied over a large range to observe the effect on radioactivity readout on a wider scale.

A.2.5. Data and Uncertainty Analysis

The entire dose calibrator had an instrumental uncertainty of $\pm 2\%$ (Capintec, 2007, 2015). Since the radioactivity is directly proportional to the radioactivity readout in the local range of calibration setting numbers, we calculated 2% of the maximum in each range, and added or subtracted it to the maximum or minimum of each range to get new values, $N_{A_{min}}$ and $N_{A_{max}}$. If the displayed value needed to be multiplied or divided by a scaling factor, the number was adjusted by 2% and by the same scaling factor. The midpoint of this new range, $N_{A_{mid}}$, was calculated as the mean of $N_{A_{min}}$ and $N_{A_{max}}$ for that trial, and the uncertainty of this midpoint was $(N_{A_{max}} - N_{A_{min}})/2$. If the vessel was placed in the dose calibrator multiple times, the midpoints from each placement were averaged. The uncertainty in this mean resulted from propagating the individual uncertainty from each placement using the following equation:

$$\delta N_A^2 = \left(\frac{1}{n}\right)^2 \sum_{i=1}^n \delta N_{A_i}^2, \quad (\text{A.2})$$

where δN_A is the uncertainty in the average; n is the number of trials; and δN_{A_i} is the uncertainty in each value that was averaged together. Equation A.2 applies the total differential equation for the propagation of small uncertainties to the equation for the arithmetic mean, if all uncertainties are uncorrelated (Arras, 1998; Croarkin; Ku, 1966).

Dose calibrator measurements were performed on vessels in triplicate, each resulting in an average result with uncertainty. These results across the three vessels were averaged, and the uncertainty in each final result was obtained by propagating the uncertainties from the individual vessels through Equation A.2 (This time, with $n=3$). The final average result was rounded to the nearest integer (because all dial settings are integers), and the uncertainty was accordingly rounded up to the nearest integer to be conservative. These results are the final values and uncertainties that are shown in Table A.3.

A.3. Results

Our results for calibration setting numbers for the Capintec dose calibrators are shown in Table A.3 for our six isotopes, both in 2 mL microcentrifuge tubes and in 10 cc syringes. Table A.3 also shows the gamma factor (I) for each of these isotopes, calculated by Smith and Stabin (2012) to express the dose rates for various isotopes based on a weighted average of gamma-ray energies and branching ratios—including annihilation photons. All results were greater than the recommended values found in the user manuals to varying degrees. This was interesting because the recommended values were interpolated from results based on 5 mL calibration sources, which would be near the midpoint of the two volumes.

Table A.3. Results for calibration setting numbers on Capintec CRC-15R and CRC-25R dose calibrators.

Isotope	Gamma Factor ^a Γ (R·cm ² /mCi·h)	From Manual ^b	New Calibration Setting		Percent Difference in Radioactivity Readout (%)
			2 mL Tube	10 cc Syringe	
⁵² Mn	18.4	676÷2	759±12 (÷2)	777±13 (÷2)	+10.2%
⁶⁴ Cu	1.05	15 or 115 (×2)	16±2	108±2 (x2)	-3.6% ^c
⁷⁶ Br	14	495÷2	604±9 (÷2)	800±9 (÷2)	+52.6%
⁸⁶ Y	18.9	711÷2	762±12 (÷2)	815±9	-44.1%
⁸⁹ Zr	6.59	465	514±6	527±6	+11.2%
¹²⁴ I	6.59	570	29±1	733±7	+24.6%

For (x2) or (÷2), the radioactivity readout from the dose calibrator should be multiplied or divided by 2 to obtain the correct radioactivity measurement. ^aGamma factor describes the dose rate from gamma radiation emitted by an isotope. (Data from: (Smith and Stabin, 2012).) ^bAll recommended dial settings were the same in the manuals for both the CRC-15R and CRC-25R models, except for ⁷⁶Br and ⁸⁹Zr (not listed in the manual for the CRC-25R). (Recommended setting(s) from: Capintec, 2007, 2015). ^cCalculated relative to the radioactivity readout using setting: 15.

For comparison, we measured each of the isotopes in a 10 cc syringe using our result for the calibration setting number and also the recommended value, and the percent difference relative to the measurement using the new value was calculated. These percentages of difference varied significantly (Table A.3), and other published works reported (Table A.4) that activities measured using recommended calibration setting numbers can differ slightly (~1-10%) or greatly: +50% for ⁹⁰Y (Coursey et al., 1993); +45% and -42% for ¹²⁵I in different geometries (Zimmerman et al., 2002); and +35% for ¹¹¹In (Ceccatelli et al., 2007). In the majority of published studies listed in Table A.4, the radioactivity measured using recommended settings would overestimate the amount of radioactivity that was present in the sample.

Table A.4. Selected results from other studies that determined setting numbers for various medical radionuclides and models of Capintec dose calibrators.

Isotope	Reference	Method	Capintec Model ¹	Source			Result	
				Vessel Geometry	Vessel Volume V_{vessel} (mL)	Liquid Volume V_{source} (mL)	Setting Number ² N_A (-)	Readout Difference ³ (%)
¹⁸ F	(Cessna, et al., 2008)	4 $\pi\beta$ -LS	CRC-15R	NIST ampoule	5	5	472	+6.4
			CRC-15R	Syringe	3	1	484	+8.9
			CRC-15PET	"	"	"	501	+12.7
			CRC-12	"	"	"	500	+13.3
	(Mo, et al., 2006)	4 $\pi\beta$ -LS	CRC-712M	Wheaton vial	-	-	459	-
	(Zimmerman, et al., 2001)	HPGe	CRC-12	Monojet syringe	12	9	482	+8.3
			CRC-35R	NIST ampoule	-	-	477	+6.2
	(Zimmerman and Cessna, 2000)	4 $\pi\beta$ -LS	CRC-12	Mallinckrodt dose vial	10	5	463	+4.5
"	CRC-12		plastic syringe	12	9	482	+7.3	
⁸⁹ Zr	(Beattie, et al., 2014)	HPGe	CRC-15R	borosilicate glass vial	20	10	517	+8.00-12.0
⁹⁰ Y	(Coursey, et al., 1993)	HPGe	CRC-12	NIST ampoule	-	-	48 ($\times 10$)	+50
							494 (with Cu filter)	+14.9-28.0
¹²⁴ I	(Beattie, et al., 2014)	HPGe	CRC-15R	borosilicate glass vial	20	10	494 (with Cu filter)	+14.9-28.0
¹²⁵ I	(Zimmerman, et al., 2002)	NaI(Tl)	CRC-12	plastic syringe	5	-	497	+45
			CRC-12	conical glass dose vial	2	-	143	-42
¹³³ Xe	(Zimmerman and Cessna, 2000)	4 $\pi\beta$ -LS	CRC-12	Dupont dose vial	3	-	181	-2.7
			CRC-12	NIST ampoule	-	-	184	-1.7
¹⁸⁸ Re	(Zimmerman and Cessna, 2000)	4 $\pi\beta$ -LS	CRC-12	SoloPak dose vial	5	-	620 ($\times 10$)	+22.2
	(Zimmerman, et al., 1999)	4 $\pi\beta$ -LS	CRC-12	NIST ampoule	-	-	630 ($\times 10$)	+30

¹All dose calibrator models were by Capintec. These results for calibration setting numbers may translate across certain models of Capintec dose calibrators, but not necessarily all models. ²Some calibration setting numbers require that the radioactivity readout be multiply or divided by a factor for an accurate measurement. ³This column is the percentage difference of the radioactivity readout using the calibration number from the user manual versus the radioactivity readout using the experimentally determined calibration number.

A.4. Discussion

For selected isotopes and geometries, the radioactivity readout over a wide range of calibration setting numbers was also recorded. These data were plotted in Figure A.1 and demonstrate something similar to an inverse relationship of A_{RO} to N_A across small and large ranges for N_A . These isotopes represented a variety of gamma-ray dose rates, such as ^{52}Mn , ^{64}Cu , and ^{124}I , all in 2 mL microcentrifuge tubes. Readout radioactivity was normalized to the largest value that was measured using the calibration setting numbers in that experiment for that radionuclide. It is important to be aware of these relationships because the fitted equations can be used to calculate the correct radioactivity of a sample in case the incorrect setting is accidentally used in a measurement. Therefore, when using the dose calibrator, the calibration setting number used should be recorded in case rescaling is necessary in the future.

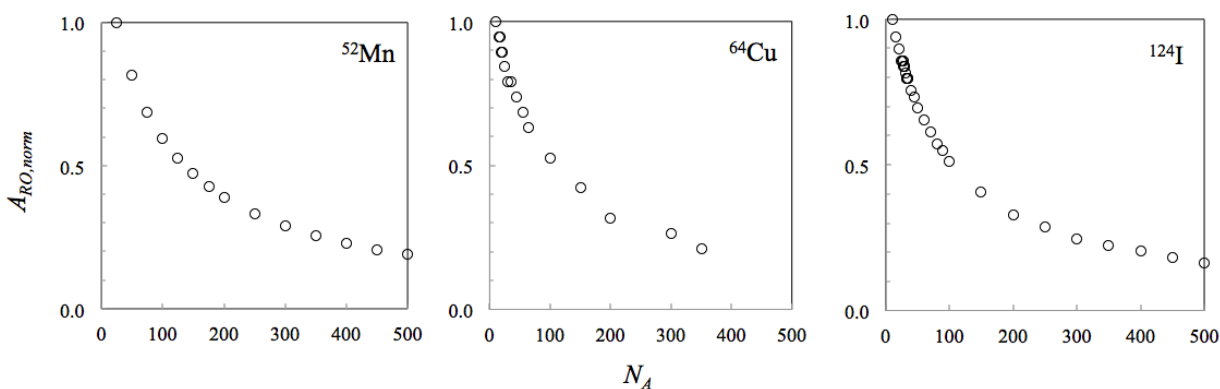


Figure A.1. Plots of normalized readout radioactivity ($A_{RO, norm}$) versus calibration setting numbers (N_A) over large ranges of settings.

Readout radioactivity was normalized to the largest value that was measured using the calibration setting numbers in that experiment for that radionuclide. Over large ranges for three isotopes with very different total gamma-ray dose rates: ^{52}Mn , ^{64}Cu , and ^{124}I . All results in this figure were from samples in 2 mL microcentrifuge tubes.

Using gamma-ray spectroscopy results as a reference, calibration setting numbers for using Capintec dose calibrators to measure the radioactivity of six PET isotopes: ^{52}Mn , ^{64}Cu , ^{76}Br , ^{86}Y , ^{89}Zr , and ^{124}I were determined experimentally for 2 mL microcentrifuge tubes and 10 cc syringes. In many cases, results were significantly different from the calibration setting numbers recommended by the manufacturer. Since the CRC-15R and CRC-25R models of dose calibrators from Capintec were used, results can be used directly for that family of models, including: 15R, 15W, 25R, 25W, 127R, and Ultra-R (Capintec, 2009). However, since the manufacturer's recommended settings are interpolated from other measurements that used a standard glass NIST source geometry, and because results show significant effects of sample geometry for several isotopes, we recommend utilizing a reference sample or high-precision reference measurement—such as HPGe gamma spectroscopy—to experimentally determine calibration setting numbers for various geometries and materials involving dose calibrator use.

In most cases, calibration setting numbers differed from those recommended in the user manual, which meant that using the recommended calibration settings could result in radioactivity measurements higher or lower than expected. Additionally, settings determined for the 10 cc syringes were consistently greater than for the 2 mL geometry. Our results reiterate the widely known fact that experimentally determined dose calibrator settings for various radionuclides and sample geometries are necessary for accurate measurements of radioactivity. These settings have potentially significant implications for radiochemistry experiments, as well as dosimetry for pre-clinical and clinical applications of radionuclides, including the PET radionuclides that were examined in this work.

A.5. Conclusions and Recommendations

Using gamma-ray spectroscopy results as a reference, we have experimentally determined calibration setting numbers for using certain Capintec dose calibrators to measure the radioactivity of six PET isotopes: ^{52}Mn , ^{64}Cu , ^{76}Br , ^{86}Y , ^{89}Zr , and ^{124}I . Measurements were conducted for 2 mL microcentrifuge tubes and 10 cc syringes to provide results for two vessels that are commonly placed in dose calibrators to measure radioactivity for either radiochemistry lab work or for *in vivo* injections, respectively. In many cases, our results were significantly different from the calibration setting numbers recommended by the manufacturer. As the CRC-15R and CRC-25R models of dose calibrators from Capintec were used, our results can be used directly for that family of models, including: 15R, 15W, 25R, 25W, 127R, and Ultra-R (Capintec, 2009). However, since the calibrations settings recommended by the manufacturer are interpolated results based on measurements using a different source geometry than what is commonly used in practice for clinical and pre-clinical radiochemistry. Since our results show significant effects of sample geometry, we join with a body of literature to recommend performing in-house calibration for any radionuclide or vessel geometry by utilizing a high-precision measurement, such as HPGe gamma spectroscopy, as a reference for cross-calibration.

A.6. References

- Arras, K.O., 1998. An Introduction To Error Propagation: Derivation, Meaning and Examples of Equation $C_y = F_x C_x F_x T$. Technical Report EPFL-ASL-TR-98-01 R3. Swiss Federal Institute of Technology Lausanne, Lausanne, Switzerland, p. 6.
- Avila-Rodriguez, M.A., Nye, J.A., Nickles, R.J., 2008. Production and separation of non-carrier-added ^{86}Y from enriched ^{86}Sr targets. *Appl. Radiat. Isot.* 66, 9-13.

- Beattie, B.J., Pentlow, K.S., O'Donoghue, J., Humm, J.L., 2014. A Recommendation for Revised Dose Calibrator Measurement Procedures for ^{89}Zr and ^{124}I . PLOS ONE. 9, e106868.
- Berridge, M., 2013. Personal communication. Message to: Wooten, A.L. 30 Jan. 2013. E-mail.
- Canberra. Detector specification and performance data. Detector model: GC2018, Detector serial No.: 10475. Doc. No.: DPF-009, Rev. H, Date: 2012.
- Canberra. Detector specifications and performance data. Model: GC1818, Serial No.: 2953512. No additional identifying information available.
- Capintec, 2007. CRC-15R: Owner's Manual. Manual No. 9250-0038, Rev. Y.
- Capintec, 2009. Letter sent to customers regarding a new recommendation for calibration setting number for F-18 in select models of dose calibrators.
- Capintec, 2015. CRC-25R: Owner's Manual. Manual No. 9250-0122, Rev. H.
- Ceccatelli, A., Benassi, M., D'Andrea, M., De Felice, P., Fazio, A., Nocentini, S., Strigari, L., 2007. Experimental determination of calibration settings of a commercially available radionuclide calibrator for various clinical measurement geometries and radionuclides. Appl. Radiat. Isot. 65, 120-125.
- Cessna, J.T., Schultz, M.K., Leslie, T., Bores, N., 2008. Radionuclide calibrator measurements of ^{18}F in a 3 ml plastic syringe. Appl. Radiat. Isot. 66, 988-993.
- Chandra, R., 2011. Nuclear Medicine Physics: The Basics, 7th ed. ed. Lippincott Williams & Wilkins, Wolters Kluwer, Philadelphia.
- Coursey, B.M., Calhoun, J.M., Cessna, J.T., 1993. Radioassays of yttrium-90 used in nuclear medicine. Nucl. Med. Biol. 20, 693-699.
- Croarkin, C., Measurement Process Characterization, in: Croarkin, C., Tobias, P. (Eds.), NIST/SEMATECH e-Handbook of Statistical Methods. NIST/SEMATECH, Online only. <http://www.itl.nist.gov/div898/handbook/mpc/section5/mpc55.htm>.
- Holland, J.P., Sheh, Y., Lewis, J.S., 2009. Standardized methods for the production of high specific-activity zirconium-89. Nucl. Med. Biol. 36, 729-739.
- Ikotun, O.F., Lapi, S.E., 2011. The rise of metal radionuclides in medical imaging: copper-64, zirconium-89 and yttrium-86. Future Med. Chem. 3, 599-621.
- International Atomic energy Agency (IAEA)/Division of Life Sciences/Medical Applications Section, 1984. Quality Control of Nuclear Medicine Instruments. IAEA-TECDOC-317, Vienna.
- Knust, E.J., Dutschka, K., Weinreich, R., 2000. Preparation of ^{124}I solutions after thermodistillation of irradiated $^{124}\text{TeO}_2$ targets. Appl. Radiat. Isot. 52, 181-184.
- Ku, H.H., 1966. Notes on the Use of Propagation of Error Formulas. J. Res. Natl. Bur. Stand. C: Engr. Instr. 70C, 263-273.
- Kume, M., Carey, P.C., Gaehle, G., Madrid, E., Voller, T., Margenau, W., Welch, M.J., Lapi, S.E., 2012. A semi-automated system for the routine production of copper-64. Appl. Radiat. Isot. 70, 1803-1806.

- McCarthy, D.W., Shefer, R.E., Klinkowstein, R.E., Bass, L.A., Margeneau, W.H., Cutler, C.S., Anderson, C.J., Welch, M.J., 1997. Efficient production of high specific activity ^{64}Cu using a biomedical cyclotron. *Nucl. Med. Biol.* 24, 35-43.
- McCarthy, T.J., Laforest, R., Downer, J.B., Lo, A.-R., Margenau, W.H., Hughey, B., Shefer, R.E., Klinkowskein, R.E., Welch, M.J., 1999. Investigation of I-124, Br-76, and Br-77 production using a small biomedical cyclotron-can induction furnaces help in the preparation and separation of targets?, in: McCarthy, T.J. (Ed.), 8th Workshop on Targetry & Target Chemistry, Saint Louis, Missouri, United States, pp. 127-130.
- Meijs, W.E., Herscheid, J.D.M., Haisma, H.J., Wijbrandts, R., van Langevelde, F., Vanleuffen, P.J., Mooy, R., Pinedo, H.M., 1994. Production of Highly Pure No-Carrier Added ^{89}Zr for the Labeling of Antibodies with a Positron Emitter. *Appl. Radiat. Isot.* 45, 1143-1147.
- Mo, L., Reinhard, M.I., Davies, J.B., Alexiev, D., Baldock, C., 2006. Calibration of the Capintec CRC-712M dose calibrator for ^{18}F . *Appl. Radiat. Isot.* 64, 485-489.
- National Institute of Standards and Technology (NIST), 2011. Ampoule Specifications and Opening Procedure. Online. <http://www.nist.gov/pml/div682/grp04/srm.cfm>.
- Nayak, T.K., Brechbiel, M.W., 2009. Radioimmunoimaging with longer-lived positron-emitting radionuclides: potentials and challenges. *Bioconjug. Chem.* 20, 825-841.
- Sheh, Y., Kozirowski, J., Balatoni, J., Lom, C., Dahl, J., Finn, R., 2000. Low energy cyclotron production and chemical separation of "no carrier added" iodine-124 from a reusable, enriched tellurium-124 dioxide/aluminum oxide solid solution target. *Radiochim. Acta* 88, 169-173.
- Smith, D.S., Stabin, M.G., 2012. Exposure rate constants and lead shielding values for over 1,100 radionuclides. *Health Phys.* 102, 271-291.
- Tolmachev, V., Lovqvist, A., Einarsson, L., Schultz, J., Lundqvist, H., 1998. Production of Br-76 by a low-energy cyclotron. *Appl. Radiat. Isot.* 49, 1537-1540.
- Tyler, D.K., Woods, M.J., 2002. Syringe Calibration Factors and Volume Correction Factors for the NPL Secondary Standard Radionuclide Calibrator. NPL Report CIRM 56, National Physical Laboratory, Teddington, Middlesex, UK.
- Tyler, D.K., Woods, M.J., 2003. Syringe calibration factors for the NPL Secondary Standard Radionuclide Calibrator for selected medical radionuclides. *Appl. Radiat. Isot.* 59, 367-372.
- Wadas, T.J., Wong, E.H., Weisman, G.R., Anderson, C.J., 2010. Coordinating radiometals of copper, gallium, indium, yttrium, and zirconium for PET and SPECT imaging of disease. *Chem. Rev.* 110, 2858-2902.
- Wooten, A.L., Lewis, B.C., Lapi, S.E., 2015. Cross-sections for (p,x) reactions on natural chromium for the production of ^{52}Mn , ^{54}Mn radioisotopes. *Appl. Radiat. Isot.* 96, 154-161.
- Wooten, A.L., Schweitzer, G.D., Lawrence, L.A., Madrid, E., Lapi, S.E., 2012. An Automated System for Production of ^{89}Zr . *AIP Conf. Proc.* 1509, 201-205.
- Yoo, J., Tang, L., Perkins, T.A., Rowland, D.J., Laforest, R., Lewis, J.S., Welch, M.J., 2005. Preparation of high specific activity ^{86}Y using a small biomedical cyclotron. *Nucl. Med. Biol.* 32, 891-897.
- Zimmerman, B.E., Cessna, J.T., 2000. Experimental determinations of commercial 'dose calibrator' settings for nuclides used in nuclear medicine. *Appl. Radiat. Isot.* 52, 615-619.

- Zimmerman, B.E., Cessna, J.T., Dorton, J.A., 2002. Experimental investigation of dose calibrator response for ^{125}I brachytherapy solutions contained in 5 mL plastic syringes and 2 mL conical glass v-vials as a function of filling mass. *Med. Phys.* 29, 1547-1555.
- Zimmerman, B.E., Cessna, J.T., Unterweger, M.P., Li, A.N., Whiting, J.S., Knapp, F.F., Jr., 1999. A new experimental determination of the dose calibrator setting for ^{188}Re . *J. Nucl. Med.* 40, 1508-1516.
- Zimmerman, B.E., Kubicek, G.J., Cessna, J.T., Plascjak, P.S., Eckelman, W.C., 2001. Radioassays and experimental evaluation of dose calibrator settings for ^{18}F . *Appl. Radiat. Isot.* 54, 113-122.